2 cy

UCRL-19890

MASTER

BUBBLE CHAMBER STUDY OF POLARIZED $\gamma p \rightarrow \pi^+ \pi^- p$ AT 2.8 AND 4.7 GeV

Kenneth Charles Moffeit
(Ph. D. Thesis)

November 1970

AEC Contract No. W-7405-eng-48

LAWRENCE RADIATION LABORATORY
UNIVERSITY of CALIFORNIA BERKELEY

UCRL-19890

DISCLAIMER

THIS PAGE

WAS INTENTIONALLY

LEFT BLANK

TABLE OF CONTENTS

Abstract iv

I. INTRODUCTION 1

II. EXPERIMENTAL PROCEDURE 5

A. Photon Beam 5

B. Bubble Chamber 9

C. Energy Spectrum 11

D. Polarization Properties 14

E. Scanning Procedures 17

F. Measuring and Kinematical Reconstruction 21

III. TOTAL AND PARTIAL CROSS SECTIONS 27

IV. ρ^{o} PHOTOPRODUCTION IN THE REACTION $\gamma p \rightarrow \pi^{+}\pi^{-}p$ 34

A. Dalitz and Chew-Low Plot Distributions 34

B. Cross Sections and the ρ^{o} Mass Shift 37

1. Parameterization and Model Independent Results 37

2. Söding Model 60

3. Comparison with the Vector Dominance Model 67

C. Conservation of s-Channel Helicity in ρ^{o} Photoproduction 69

D. Other Models 97

V. THE ρ^{o}-ω INTERFERENCE PARAMETERS IN DIFFRACTIVE PHOTOPRODUCTION OF VECTOR MESONS ON HYDROGEN 99

VI. Δ PRODUCTION IN THE REACTION $\gamma p \rightarrow \pi^{+}\pi^{-}p$ 113

VII. CONCLUSIONS 127

APPENDIX A: Comparison of Measurements at LRL and SLAC 129

APPENDIX B: Maximum likelihood fitting of $\gamma p \to \pi^+\pi^- p$ .. 136

APPENDIX C: Description of Söding Model 137

ACKNOWLEDGMENTS 140

REFERENCES 142

Bubble Chamber Study of Polarized $\gamma p \rightarrow \pi^+\pi^- p$ at 2.8 and 4.7 GeV*

By

Kenneth Charles Moffeit
Department of Physics
University of California
Berkeley, California 94720

November 10, 1970

ABSTRACT

A nearly monochromatic and linearly polarized photon beam produced by Compton backscattering of ruby laser light was used to study the reaction $\gamma p \rightarrow \pi^+\pi^- p$ at 2.8 and 4.7 GeV in a hydrogen bubble chamber. The cross sections for this reaction at 2.8 and 4.7 GeV are found to be 30.6 ± 1.2 and 19.9 ± 0.8 μb, respectively.

Rho production and decay via $\gamma p \rightarrow \rho^o p$ is studied and found to proceed almost completely through natural parity exchange. The contributions from unnatural parity exchange at 2.8 and 4.7 GeV are 3.1 ± 3.1% and -1.1 ± 2.8%, respectively, for momentum transfer $|t| < 1$ GeV^2. The behavior of the density

* Work supported in part by the U.S. Atomic Energy Commission and the National Science Foundation.

matrix elements shows that the rho production mechanism conserves s-channel c.m.s. helicity for $|t| < 0.4$ GeV^2. The dependence of the ρ^o mass shape on the momentum transfer is inconsistent with the Ross-Stodolsky factor. Evidence is presented for an interference of ρ^o production with background. The data are compared with models including that of Söding, and the total and differential cross sections for ρ^o production are presented.

We measured the ρ^o-ω interference parameters. Assuming the ratio of the ρ^o and ω photoproduction amplitudes $|A_\omega/A_\rho|^2 = 7.1$ we find $R_e(\delta e^{i\beta}) = 2.3 \pm 0.9$ MeV and $Im(\delta e^{i\beta}) = -0.4 \pm 0.9$ MeV, where $\delta(\approx 2.3$ MeV) is the mass mixing parameter and $\beta(\approx -9^o)$ is the relative phase of the ρ^o-ω amplitudes.

The production of $\Delta(1236)$ via $\gamma p \to \Delta^{++}\pi^-$ $(\Delta^o\pi^+)$ was studied in the reaction $\gamma p \to \pi^+\pi^- p$. We present cross sections and measurement of the parity asymmetry P_σ; for Δ^{++} production with momentum transfer $|t_\Delta| < 0.5$ GeV^2 we found the values $P_\sigma = -0.27 \pm 0.12$ and -0.53 ± 0.15 at 2.8 and 4.7 GeV, respectively, whereas pure one-pion exchange would lead to $P_\sigma = -1$.

I. INTRODUCTION

In this thesis we report the results from a study of photoproduction with a linearly polarized photon beam at average energies of 2.8 and 4.7 GeV.[1] The backscattering of an intense ruby laser beam on high-energy electrons results in a nearly monochromatic photon beam with a degree of polarization greater than 90%. By exposing the 82-inch hydrogen bubble chamber at the Stanford Linear Accelerator Center to this photon beam we make a clean selection of the reaction

$$\gamma p \rightarrow \pi^+\pi^- p \ . \qquad (1)$$

The production of rho mesons in reaction (1) with linearly polarized photons provides an elegant technique to study the production mechanism in detail. For example, a separation into the orthogonal contributions from natural and unnatural parity ($P = \pm(-1)^J$) exchanges in the t-channel can be made by measuring the ρ^o decay angular distribution with respect to the photon polarization plane.[2]

Diffractive ρ^o photoproduction (Sect. IV): Previous ρ^o photoproduction studies[3-6] have shown that the ρ^o cross section is approximately constant above 2 GeV indicating a diffractive character of the production mechanism. Recent experiments at DESY[7] and Cornell[8] using polarized photon beams from coherent bremsstrahlung on diamond crystals together with counter tech-

niques to measure the ρ^o cross section parallel and perpendicular to the polarization plane have shown that the transverse part of ρ^o production in reaction (1) is dominated by natural parity exchange. The DESY bubble chamber experiment, using an unpolarized bremsstrahlung photon beam, has indicated that s-channel c.m. system helicity is conserved.[4] By observing the full ρ^o decay angular distributions correlated with the polarization vector of the incident photon we establish that ρ^o production is dominated by natural-parity exchange and that it conserves s-channel c.m. system helicity for $|t| < 0.4$ GeV^2 (t is the square of the four-momentum transfer between target and recoil protons).

Rho Mass Shift (Sect. IV): The first observation of ρ^o photoproduction on hydrogen[9] reported a mass for the ρ of $\approx$ 720 MeV. Bubble chamber experiments performed at the Cambridge Electron Accelerator[3] and DESY[4] confirmed the apparent mass shift (lower by $\approx$ 40 MeV from ρ production by charged pion beams), and it was shown that the rho shape is skewed with respect to the p-wave Breit-Wigner resonance shape. These observations have necessitated the use of models to fit the data, and because no model has been preferred experimentally, the ρ^o production cross section has been uncertain to about 20%. We present model-independent cross sections for production of $\pi^+\pi^-$ pairs from reaction (1) in the s-channel c.m. helicity-conserving p-wave state which dominates in the ρ^o region. The high statistics of this experiment allows us to test the Ross-Stodolsky factor[10] by investigating the t dependent of the ρ^o

mass shape. We also determined the ρ^o-production cross sections using the Söding model,[11] which we found to agree with the data.

Rho-omega Interference (Sect. V): We have examined reaction (1) for evidence of ρ^o-ω interference.[12] The possibility of the $\omega \to \pi^+\pi^-$ (G-violating) amplitude interfering with the $\rho^o \to \pi^+\pi^-$ amplitude was proposed some time ago,[13] but interference effects amounting to two or more standard deviations in the $\pi^+\pi^-$ channel have been reported only recently.[14-20,25] These experimental results have stimulated new theoretical studies of ρ^o-ω mixing.[21-24] The magnitude of the observed $\omega \to \pi^+\pi^-$ amplitude agrees with these theoretical expectations, and its relative phase, as seen in the detailed shapes of the interference effects, can be interpreted in terms of simple models for ρ^o and ω production in quasi-two-body reactions.

Delta Production (Sect. VI): Previous photoproduction experiments using bubble chambers[26,27] and the SLAC-spectrometer[28] have studied $\Delta^{++}(1236)$ production in reaction 1, and have shown that for photon energies $E_\gamma \gtrsim 2$ GeV the differential cross section $d\sigma/dt_\Delta$ (t_Δ is the square of the four-momentum transfer between target proton and outgoing Δ) is proportional to $1/E_\gamma^2$ in common with a number of two-body photoproduction processes.[29] Such an energy dependence would be expected for processes dominated by one-pion exchange (OPE), but OPE leads to a zero cross section in the forward direction in contrast to

experiment;[28] it is also not gauge invariant. These difficulties are overcome by a gauge-invariant extension of the OPE model proposed by Stichel and Scholz.[30] The angular correlations in Δ production by polarized photons provide a further check of the gauge invariant OPE model[31] and a test of relations based on vector dominance (VDM).[32]

The evaluation of the data in this experiment was carried out by the SLAC-Berkeley-Tufts Collaboration.[1] Preliminary results have already been reported in a series of publications.[1] For completeness this thesis includes the results on Δ production and ρ^{o}-ω interference. The treatment of the cross sections found in Section III and the ρ^{o} production results of Section IV is significantly different from that presented in publications a and b of reference 1. A detailed study of the reactions involving missing neutrals (e.g., $\gamma p \rightarrow \omega p$) can be found in the thesis of William Podolsky.[33]

II. EXPERIMENTAL PROCEDURES

A. Photon Beam

In 1962, R. Milburn,[34] concurrently with F. Arutyunian, et al.,[35] pointed out that backward Compton scattering of an intense polarized laser light beam by high energy electrons would produce useful yields of monoenergetic, polarized photons. Such a beam[36,37] was used for this experiment which was performed at the Stanford Linear Accelerator Center (SLAC). Because the reaction

$$\gamma(k_i) + e^-(E_e) \rightarrow e^- + \gamma(k_f)$$

is a two-body process, the energy k_f of the scattered photon depends only on the laboratory angle, θ, as measured with respect to the incident electron beam. It can be shown that when the energies of the incoming photon k_i and electron E_e are fixed:

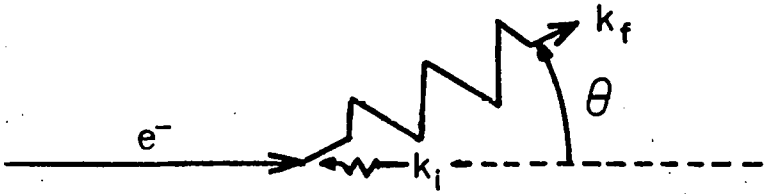

$$k_f = \frac{k_{f_{max}}}{1 + \frac{E_e{}^2\theta^2}{s}}$$

where s is the center of mass energy squared,

$$s \approx m_e^2 + 4\, k_i\, E_e,\quad k_{f_{max}} = \frac{4\, E_e^2\, k_i}{s},\ \text{and}$$

$k_i = 1.78$ eV. By collimating the backscattered photon beam and incident electron beam we find

$$\frac{k_{f_{max}} - k_{f_{min}}}{k_{f_{min}}} = \frac{k_{f_{max}}}{4k_i}\,\theta_c^2$$

where θ_c is the collimating angle ($\approx 10^{-5}$ radians). Thus, the energy resolution (FWHM) is expected to vary from about two percent for $k_{f_{max}} = 1$ GeV to ten percent for $k_{f_{max}} = 7.5$ GeV. Another feature of the Compton process is that if the incident light is polarized, after backscattering ($\theta = 0^\circ$), it is still almost completely polarized in the same way.

Figure 1 shows the beam schematic layout. About 10^{11} electrons in a 100-nanosecond pulse passed through the five-meter-long interaction region. The electron beam in the interaction region was ~ 7mm in diameter with a divergence of about 10^{-5} radians. The incident linearly polarized light beam was obtained by Q-switching a ruby laser of frequency 6943 Å ($k_i = 1.786$ eV) with a maximum output of two joules, and pulse length equal to fifty nanoseconds. The plane of

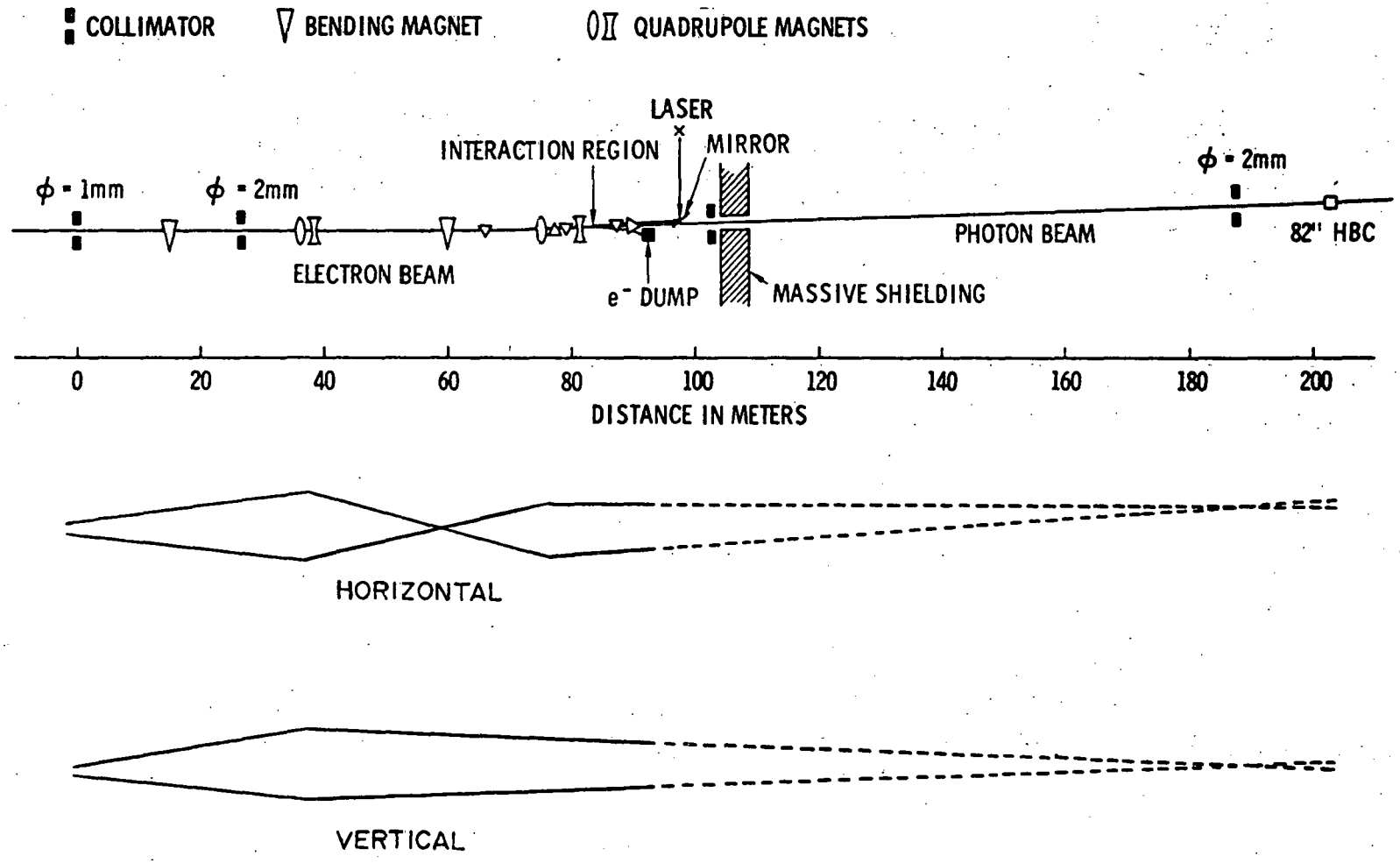

Fig. 1. Experimental layout of the beam. The beam profile is shown in the horizontal and vertical planes (not to scale).

linearly polarized light could be rotated 90° by inserting a half-wave plate into the beam line. After the two beams clashed at a relative angle of 3 milliradians, the electron beam was deflected into a dump. To minimize synchrotron radiation the electron beam first traversed a weak magnetic field until it was clear of the beam line. The synchrotron radiation spectrum resulting from electrons deflected in this weak field was low enough to be removed by a high-Z photoelectric absorber (10 Uranium foils of 0.015 radiation length) thin enough to have a negligble attenuation of the high-energy photon beam. The Compton backscattered photon beam was collimated to $\approx 10^{-5}$ radians by a two-millimeter diameter hole in the final collimator $\approx$ 100 meters downstream of the interaction region. The signals from scintillators embedded in this collimator[38] were used to control the electron beam (and hence the center of the photon beam) steering to $\approx 10^{-6}$ radians. These signals were also used to monitor the photon-beam intensity; control of the intensity was accomplished by adjusting the laser output (voltage adjustment to the flash-lamps) or the electron beam intensity.

B. Bubble Chamber

Approximately 740,000 pictures were taken at average photon energies of 2.8 and 4.7 GeV in the Lawrence Radiation Laboratory (LRL) - SLAC 82-inch hydrogen bubble chamber resulting in 92 ± 4 and 150 ± 6 events per μb, respectively. The magnetic field at the center of the chamber was 17.6 kG.

In Fig. 2, a typical bubble chamber picture containing an hadronic interaction is shown. It is noted from this example:

1) Bubble chamber pictures permit a clear distinction at the scan table between electromagnetic and hadronic interactions.

2) Because of the collimator approximately twenty meters upstream of the bubble chamber, an event or e^+e^- pair falls within ± 1.5mm of a line from the central point of the interaction region through the center of the final collimator. Hadronic events and e^+e^- pairs that are outside this area do not result from primary photons.

3) In the picture there are eight e^+e^- pairs; with more pairs, it would be very difficult to find hadronic events and even more difficult to measure them. Therefore, most of the pictures were taken with $\approx$ 50 photons per pulse; this corresponds to about seven pairs per picture.

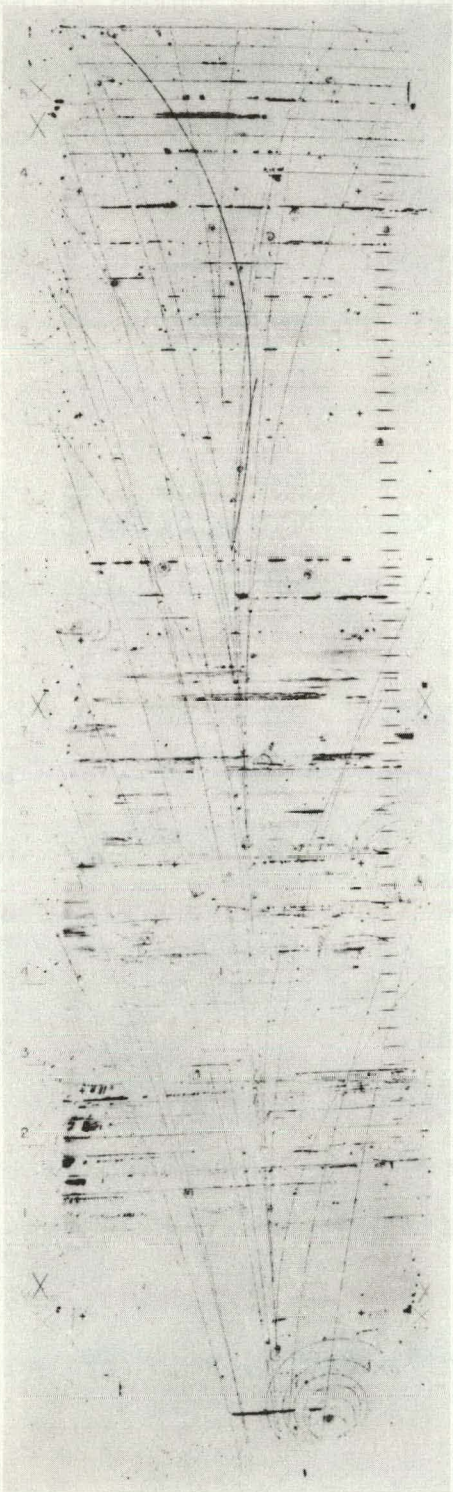

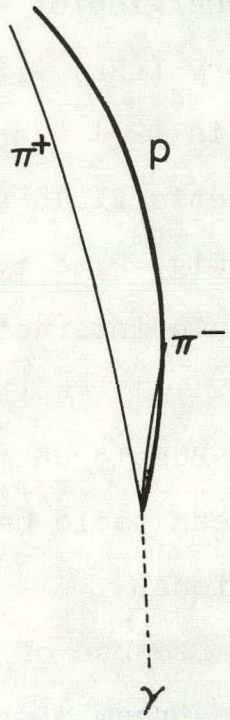

XBB 708-3776A

Fig. 2. Typical bubble chamber picture with an event of the reaction $\gamma p \rightarrow \pi^+ \pi^- p$. The background tracks are electron-positron pairs.

C. Energy Spectrum

In Fig. 3, the photon energy spectra are shown for the two energies. The spectra were obtained from the events which satisfy a three-constraint fit to the reaction $\gamma p \rightarrow \pi^+\pi^- p$. Because the cross section for this reaction is dependent on the photon energy, we weighted the events by their relative production probability,

$$P(E_\gamma) = \frac{\sigma\ \gamma p \rightarrow \pi^+\pi^- p\ (E_o)}{\sigma\ \gamma p \rightarrow \pi^+\pi^- p\ (E)}$$

where E_o is the average energy of the spectrum. The low-energy dependence of the cross section was taken from a previous experiment.[4] Because of the kinematical cutoff for $\gamma p \rightarrow \pi^+\pi^- p$, e^+e^- pairs were used to determine the photon flux below 0.5 GeV. The triangular shaped peaks with lower boundaries at about 2.4, and 4.1 GeV (for average peak energies 2.8 and 4.7 GeV, respectively) contain more than 90 percent of the photons. In addition, there is a small tail of a few percent extending to low energies.

The energy determination was checked by measuring K^o decays; and as shown in Fig. 4, the K^o mass is correct to 0.2%. The $\pi^+\pi^-$ mass resolution at the K^o mass is ± 5 MeV. The combined data for the two energies are given in Fig. 4; we find no significant differences between the two samples.

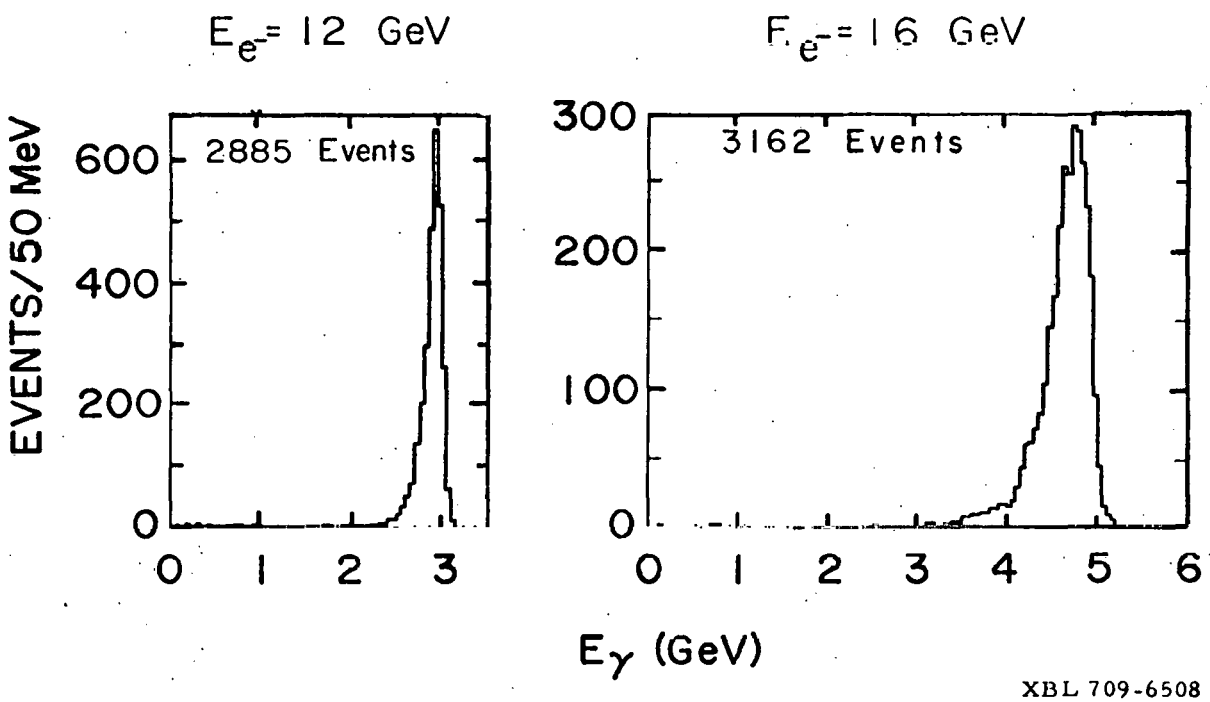

Fig. 3. Photon-energy spectra obtained from events fitting the reaction $\gamma p \rightarrow \pi^+ \pi^- p$; weighted by their relative production cross sections. Below 500 MeV the e^+-e^- pair spectra were used to obtain the photon spectra.

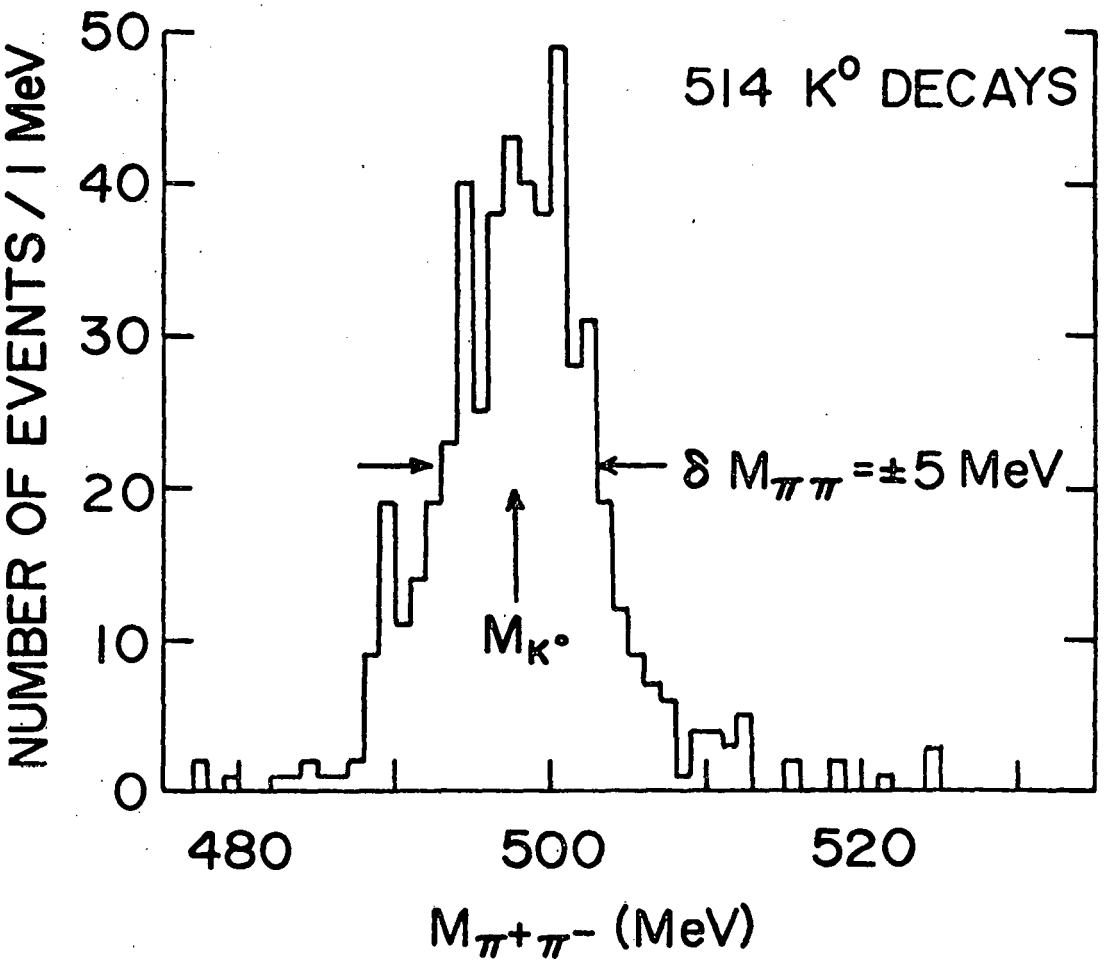

XBL 708-6434

Fig. 4. Fitted dipion mass from 514 K^o decays (combined data of the two energies). Provides test of momentum determination and mass resolution.

D. Polarization Properties

A result of Compton scattering polarized light from electrons is that the backscattered photons retain their polarization (left circularly polarized light becomes right circularly polarized). This is a simple result of conservation of angular momentum in the case of circularly polarized light. However, for linearly polarized light there is a depolarization effect that is important at higher energies; the effect comes from a sign difference between the $J = 1/2$ and 3/2 amplitudes for left and right circularly polarized light. Aside from this effect for linearly polarized light, there is a decrease in polarization for photons out of the exact backward direction. A complete treatment of polarization in Compton scattering can be found in Ref. 34-36.

The first third of the pictures were taken by alternately switching the plane of polarization from horizontal to vertical. This was done pulse-to-pulse by flipping a half-wave-plate in and out of the laser beam path. These planes were chosen to maximize any chamber related environmental biases that could occur. After it was found that the half-wave-plate attenuated the laser light intensity by approximately 30 percent, the plane of polarization was alternated only at every magazine change (about 2400 frames); the intensity of photons at the bubble chamber was then maintained at a constant value by adjusting the amount of laser light when the half-wave-plate was in the laser beam path. No detectable differences were found in the

scanning efficiency for vertical vs. horizontal polarization.

The half-wave plate used during the first run at the accelerator was found to be defective. Approximately 18 percent of the pictures were taken with this "half-wave" plate, and from its characteristics we found the backscattered photons involved had their plane of polarization 45 degrees from the vertical and the degree of linear polarization $\approx$ 81 percent. For the remainder of the photons (82 percent) the degree of linear polarization as calculated for the Compton scattering process was 95 and 93 percent for 2.8 and 4.7 GeV, respectively; averaged over the photon energy spectra.

The alignment and transport of the laser beam introduces an uncertainty in the polarization direction of the high energy photons at the bubble chamber. Although the polarization of the laser light was measured to an accuracy of one degree at the laser, we estimate total uncertainity from all effects to be $\pm 3^{\circ}$ for the polarization state without the half-wave plate. For the half-wave plate data we estimate a further uncertainty of $\pm 5^{\circ}$ in polarization direction. These uncertainties introduce a systematic uncertainty in quantities such as the parity asymmetry P_{σ} (see Section IVC, Eq. 7) and the total helicity conserving p-wave $\pi\pi$ intensity Π (see Section IVB, Eq. 5). For the combined polarization states these uncertainty are less than 2%.

The average polarization and a summary of the beam and exposure are given in Table I.

TABLE I

Beam Parameters and Exposure Statistics

Avg. beam energy, E_γ (GeV)	FWHM (MeV)	Avg. Linear Polarization P_γ	No. of Pictures	E_γ limits accepted (GeV)	Evts/μb
2.8	150	93%	292,000	2.4-3.3	92 ± 4
4.7	450	91%	454,000	4.1-5.3	150 ± 6

E. Scanning Procedures

The purpose of the scan was to find the hadronic interactions and to determine the photon flux. An interaction was defined as a number of outgoing particles resulting from a gamma-proton collision. The outgoing particles had to be hadrons such as the proton, pion, kaon, etc. Because the initial state is of positive charge, the number of outgoing tracks "prongs" from the primary vertex normally is odd with net unit of positive charge. Rare exceptions occur when a negative prong annihilates (e.g. $\pi^- p \rightarrow \pi^o n$) before it travels a visible distance, or when the outgoing proton has less than 80 MeV/c momentum, corresponding to about 1mm of range in hydrogen. Strange particles are often recognized by their decay signature. The electromagnetic background is easily identified by one of the following characteristics: 1) electron-positron pairs have even charge-balance and are normally of zero opening angle (rare wide-angle pairs can be confused with 2 prong events at the scan table), 2) triplets, where the e± pair was produced off an electron, have negative charge balance, and 3) Compton electrons, resulting from elastic photon-electron scattering, are identified by a single negative track.

The determination of photon flux was made by counting the electron-positron pairs within the fiducial area of the events. This area on the film is well-defined because the diameter of the photon beam is less than 3mm in the bubble chamber. The

area was determined during the scan by placing a straight edge on the scan table so that it intersected the average of the pair vertices; an event's primary vertex or a pair vertex was required to fall within ±2.5mm of the straight edge. The length of the scanning area was chosen so as to allow measurement of the tracks of all events to a sufficient length (a minimum of 35 cm for forward tracks and 8 cm for backward tracks). Frames which met any one of the following requirements were not scanned but recorded: A missing view, abnormally light tracks, overlapping views, and blank areas due to illumination failure.

The film was double-scanned with discrepancies resolved in a third pass. The combined double scan efficiency was found to be greater than 99% for all events except those fitting reaction (1) ($\gamma p \rightarrow \pi^+\pi^- p$) with short recoil protons. Both wide-angle pair production (WAP), simulating hadronic events, and a low scanning efficiency present difficulties here. The number of WAP events which could have been confused with events of reaction (1) has been calculated using the Bethe-Heitler cross section formula.[39] Wide angle pair candidates contaminating the events of reaction (1) were found to be 1.6% at 2.8 GeV and 2% at 4.7 GeV, the majority of which have recoil proton momentum less than 140 MeV/c ($|t| < 0.02$ GeV^2, t is the square of the momentum transfer between the target and recoil protons). For $|t| > 0.02$ GeV^2 only 4 WAP candidates at 2.8 GeV and 15 at 4.7 GeV were found. After

removing the WAP candidates the t distribution was examined for scanning losses as a function of $M_{\pi\pi}$. Assuming that the distribution is of the form exp(At) and allowing A to vary with $M_{\pi\pi}$ the scanning losses were found to be 1.2 ± 0.3% at 2.8 GeV and 5.4 ± 0.4% at 4.7 GeV. The double-scan efficiency was calculated as a function of t and found to be greater than 99% for those events of reaction (1) with $t > 0.02$ GeV^2. In summary, corrections to the cross section for $\gamma p \rightarrow \pi^+\pi^- p$ due to WAP contamination and scanning losses amount to -0.4 ± 0.5% at 2.8 GeV and +3.4 ± 0.5% at 4.7 GeV. For other topologies scanning losses due to short recoil protons were found to be negligible.

Discrepancies between the two scans in counting the electron-positron pairs occurred on about 19% of the pair counts. These were resolved in a third pass; and it was found that the normal mistake was for one scanner to record one too many or one too few pairs (see Table II). The resulting corrected combined double scan efficiency for counting pairs was ≈ 100%. Because the evaluation of the cross sections for hadronic events is normalized to the e^+e^- pairs, consideration must be given to possible differences in the scanning procedure for events and pairs. We estimate uncertainties in the pairs counted (as compared to the events) to be ±2%.

TABLE II

Under-and over-counting of e^+e^- pairs.[a]

$\delta_1 = +N$ means scanner 1 recorded N pairs too many, and similarly for δ_2. Thus in 2265 frames, there were 99 in which scanner 1 recorded correctly and scanner 2 recorded one too few.

δ_2 \ δ_1	≤ -4	-3	-2	-1	0	+1	+2	+3	≥ 4
≤ -4				1					
-3					6				
-2					6				
-1			1		99	3	1	0	1
0	2	1	5	107	1824	86	11		2
+1			1	5	76		1	1	
+2			1	1	15	2			
+3					3	1			
≥ 4					1				

[a]Numbers based on UCLRL scans only (50% of total film). At SLAC, where individual pair vertices were recorded, descrepancies were resolved on a one to one basis.

Both laboratories scanned a common subset of the film (10%). Comparison of the scan results indicated that the scanning procedures for the different laboratories gave consistent results except for events of the reaction $\gamma p \rightarrow \pi^+\pi^- p$ with short recoil protons ($|t| < 0.02$ GeV^2). For the different laboratories these events were found with varying degrees of efficiency (the average double scan efficiency was found to be $\approx$ 87%).

F. Measuring and Kinematical Reconstruction

Half the events were measured on conventional measuring machines at SLAC and half at LRL. The last two-thirds of the first measurements at LRL were processed by the Spiral Reader II; the passing rate was comparable to conventional measuring machines. Further information of the performance of the Spiral Reader can be found in the thesis of W. Podolsky.[33] At both laboratories the events were analyzed using the programs TVGP and SQUAW.[40]

After two measurements the failing events were looked at on the scan table, where the event type and other identification was checked before sending the event back for a third measurement. After the third measurement $\approx$ 2% of the 3-prong events remained to be measured. The fraction of 3-prong events which could not be measured due to secondary scatters or track obscuration was $\approx$ 5% (see Table III).

The fit hypotheses made in SQUAW are given in Table III.

TABLE III

Numbers of Events

Mark	Topology	Number Constraint	Number of Events E_γ = 2.8 GeV	Number of Events E_γ = 4.7 GeV
1	$\gamma p \rightarrow \pi^+\pi^- p$	3	2936	3281
2	$\rightarrow p\pi^+\pi^-\pi^0(m\pi^0)$ [a]	0	3238	4688
3	$\rightarrow n\pi^+\pi^+\pi^-(m\pi^0)$ [a]	0	1707	2286
4	$\rightarrow pK^+K^-$ [b]	3	79	104
	Marks 2, 3 ambiguous		681	2900
	Marks 1, 4 ambiguous		5	19
	No fit		35	73
	Remeasurable		183	308
	Unmeasurable		387	737
	Total 3-prong		9251	14396
1	$\gamma p \rightarrow p\pi^+\pi^+\pi^-\pi^-$	3	354	795
2	$\rightarrow p\pi^+\pi^+\pi^-\pi^-\pi^0(m\pi^0)$ [a]	0	260	1194
3	$\rightarrow n\,3\pi^+\,2\pi^-\,(m\pi^0)$ [a]	0	64	429
4	$\rightarrow pK^+K^-\pi^+\pi^-$ [b]	3	1	45
	Marks 2, 3 ambiguous		40	528
	Marks 1, 4 ambiguous		0	1
	No fit		5	8
	Remeasurable		41	101
	Unmeasurable		65	234
	Total 5-prong		830	3335
1	$\gamma p \rightarrow p\,3\pi^+\,3\pi^-$	3	5	44
2	$\rightarrow p\,3\pi^+\,3\pi^-\,\pi^0(m\pi^0)$ [a]	0	0	43
3	$\rightarrow n\,4\pi^+\,3\pi^-\,(m\pi^0)$ [a]	0	0	11
	Marks 2, 3 ambiguous		0	19
	No fit		0	2
	Remeasurable		0	13
	Unmeasurable		0	9
	Total 7-prong		5	141
	Total 9-prong		—	1
	Pairs counted		12,294	22,010
	Frames (Pairs counted on)		1,808	8,784
	Good Frames		292,927	452,239

[a] m = 0, 1, 2.

[b] The number of events for Mark 4 do not include those events with a visible K-decay (11 at 2.8 GeV and 18 at 4.7 GeV for $\gamma p \rightarrow K^+K^- p$).

No constraint was placed on the incident gamma energy. Hence, marks 1 and 4 have 3-constraints in the kinematical fit and marks 2 and 3 have no constraints. Selection of fits was accomplished by accepting fits compatible with bubble density and 3-constraint fits with kinematic $\chi^2 < 30$ (see also Thesis of W. Podolsky).[33]

We have investigated those events with χ^2 greater than 30 for possible losses of genuine $\gamma p \rightarrow \pi^+\pi^- p$ events. The momentum and energy distributions of the charged particles in the 3-pronged events shows this loss < 1% (see also Appendix A). We have also looked for possible biases in the kinematic reconstruction and event identification by generating Monte Carlo events with the program PHONY[41] and applying the same selection criteria as for real events. This study indicates the loss of $\gamma p \rightarrow \pi^+\pi^- p$ events to be < 1% and the contamination from other 3-prong events to be < 1%. We also estimate mistakes made in processing events to be < 1%; hence the total systematic uncertainty of reaction (1) is ± 2%.

The χ^2-distribution for the events giving a 3-constraint fit to $\gamma p \rightarrow \pi^+\pi^- p$ (reaction 1) allows one to check the treatment of errors in TVGP. If the error treatment is correct and the measurements have a Gaussian distribution, the χ^2 distribution for the events should follow the theoretical χ^2 distribution for three degrees of freedom. However, it is more common for bubble chamber experiments[42] to find their χ^2 distributions too wide by a factor of α^2, and to have too many events at high χ^2. In Fig.

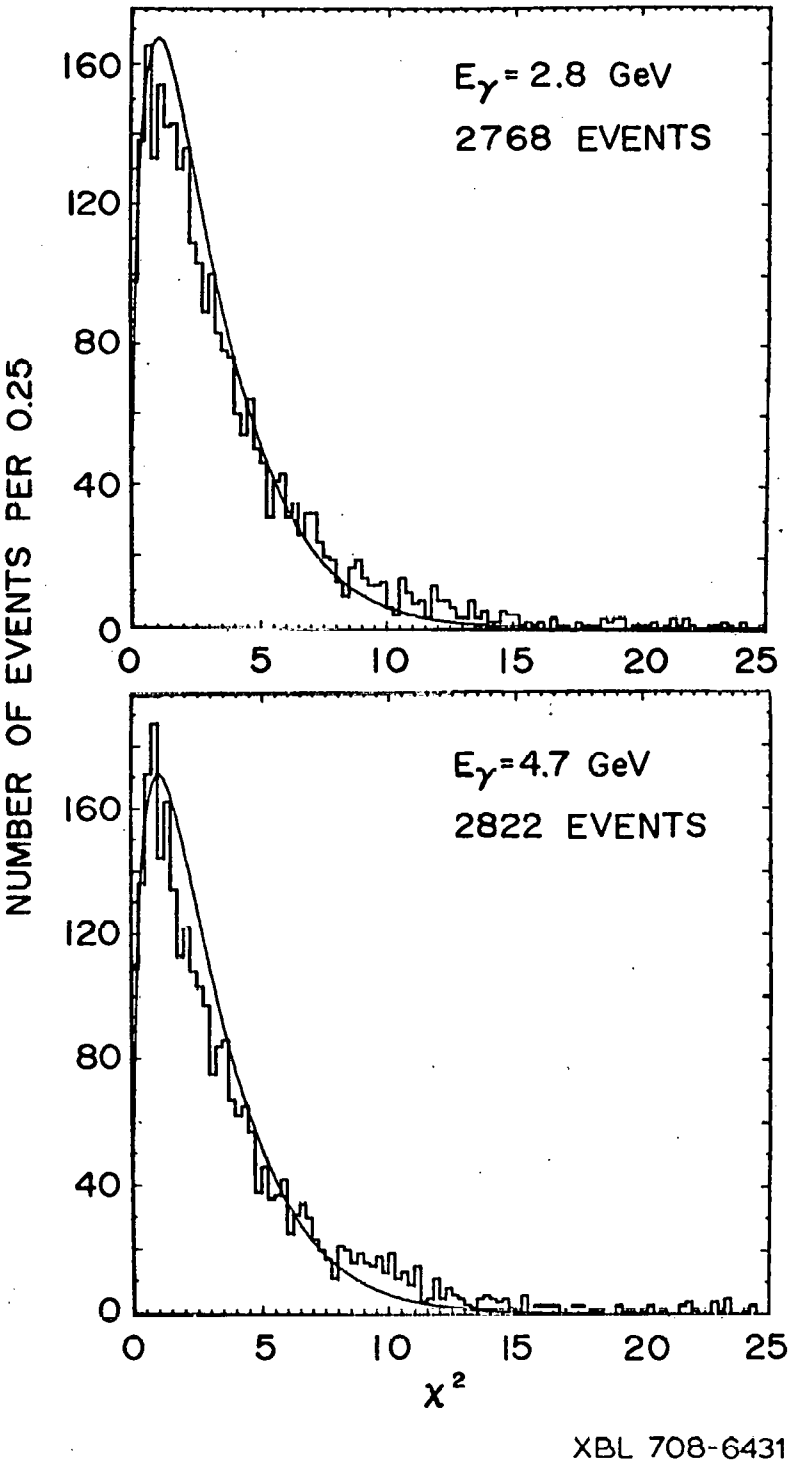

Fig. 5. Chi-squared distribution for events fitting $\gamma p \rightarrow \pi^+ \pi^- p$. The curves give the theoretical χ^2-distribution for 3-degrees of freedom.

5, we give the χ^2 distribution for the events of reaction (1). For comparison we give (full curve) the theoretical χ^2 distribution for three degrees of freedom. The $\approx$ 7 percent too many events for $\chi^2 > 10$ is primarily due to non-gaussian tails which are not taken into account. This percentage is not unreasonable. If we assume that all input errors are equally too small by α, the χ^2 distribution would scale by α^2. Output errors are then assumed to scale also by α. We selected those fits with $\chi^2 \leq 10$ to determine α^2; thus we avoided the excess of events with large χ^2 that are associated with errors having, for example, non-gaussian tails and not an underestimation of the gaussian width itself. We then made a fit of the remaining events to the χ^2 function shape

$$P(\chi^2) \propto (\chi^2/\alpha^2)^{1/2} \exp(-\chi^2/2\alpha^2).$$

This corresponds to the theoretical 3-constraint distribution at $\alpha = 1$. We obtained for α^2 the values 1.09 ± 0.02 at 2.8 GeV and 1.08 ± 0.02 at 4.7 GeV. It follows with the assumptions discussed above that the output errors from TVGP are too small by a factor $\alpha = 1.04 \pm 0.01$.

As discussed earlier (see Fig. 4), effective masses and their errors have been checked by observing the $\pi^+\pi^-$ mass distribution for K^o decays. Agreement was found for the mass of the K^o and the calculated error from SIOUX (K^o mass correct to 0.2% and $\delta M_{\pi\pi} = \pm 5$ MeV). From the calculated error in

SQUAW for the events of reaction (1) we find $\delta M_{\pi\pi} = \pm 5$ MeV in the ρ mass region. A further check was made by comparing events measured at SLAC and also at LRL on the Spiral Reader II. Details of this comparison can be found in Appendix A. The results of the measurement and reconstruction for the events processed at SLAC and LRL were found to be in good agreement.

III. TOTAL AND PARTIAL CROSS SECTIONS

The photoproduction cross sections were obtained by relating the number of hadronic events N and the number of e^+e^- pairs N (pairs) produced in the same chamber volume to the known e^+e^- pair-production cross section σ_{pair}:

$$\sigma(\gamma p \rightarrow \text{hadrons}) = \frac{N}{N(\text{pairs})} \sigma_{pair}$$

Pair production cross sections on hydrogen used in this paper result from the theoretical work of Jost, Luttinger, and Slotnick (JLS).[43] Their covariant calculation, utilizing the unitarity of the S-matrix, has the advantage that electron screening of the proton is included. Knasel[44] evaluates by numerical means the formula of JLS to an accuracy of 0.1% above 20 MeV. The values of Knasel agree in both the high energy and low energy limits with the Bethe and Bethe-Heitler results,[45] respectively. The formula of Bethe and Heitler neglects electron screening of the proton and is therefore good only at small photon energies (below 50 MeV). The formula of Bethe has approximations of the order 1/k and is thus only good at high energies (greater than 10 GeV). Knasel applies various corrections to the result of the JLS cross section to account for retardation effects and radiative correction using the work of Mork and Mork and Olsen.[46] The

Table IV: Cross sections for pair production on hydrogen according to Knasel as a function of photon energy k.

k (MeV)	σ (mb)	k (MeV)	σ (mb)
100.0	11.66	1000.0	18.29
150.0	13.15	1250.0	18.65
175.0	13.69	1500.0	18.91
200.0	14.15	1750.0	19.11
300.0	15.45	2000.0	19.26
400.0	16.28	3000.0	19.65
500.0	16.85	4000.0	19.87
600.0	17.28	5000.0	20.02
700.0	17.62	8000.0	20.25
800.0	17.88	10000.0	20.33
900.0	18.10		

cross section values determined by Knasel for pair production on hydrogen are given in Table IV and are precise to ±0.5%, well within our statistical errors of ≈ 1.6%. Recent experimental work at DESY has determined the total pair production cross section in hydrogen with errors of about 1%.[47] These results are in agreement with the work of Knasel.

The number of e^+e^- pairs was determined by counting the pairs in the fiducial area on four frames per roll yielding ≈ 30 pairs per roll compared with ≈ 25 events per roll.

Corrections were made for pairs produced outside the energy selection (see Table I) and fiducial volume. The energy correction was made using the photon-energy spectra of Fig. 3 (weighted by the relative pair production cross section). The fiducial volume correction for the pairs was made from the photon energy spectra obtained from the events of reaction (1) when the vertex falls outside an ellipse defined by $[(\Delta x)^2 + (\Delta z/2)^2]^{1/2} = 2\text{mm}$; Δx (horizontal) and Δz (vertical) are the distances the vertex is from the central beam line. The beam line was determined from a least squares fit to the events of reaction (1). The factor two dividing Δz is to account for the larger measurement uncertainty in the vertical direction. These corrections are given in Table V.

Corrections were made for hadronic events outside the fiducial volume from the distribution of the primary vertices. For the energy correction we used the photon-energy spectra

Table V: Corrections to be applied to the events in Table III.

Topology		Corrections[a] in percent for E_γ(GeV) 2.8	4.7
$\gamma p \to \pi^+\pi^- p$	α)	-0.4 ± 0.4	+3.4 ± 0.5
	β)	-1.3 ± 0.2	-2.8 ± 0.3
	γ)	-2.3 ± 0.3	-9.6 ± 0.6
	ξ)	0 ± 2	0 ± 2
Other 3-prong	β)	-0.6 ± 0.1	-0.9 ± 0.1
	γ)	-1.1 ± 0.3	-7.0 ± 0.5
	ξ)	0 ± 1	0 ± 0.6
5-prong	β)	-0.1 ± 0.1	-0.3 ± 0.1
	γ)	-0.6 ± 0.3	-4.5 ± 0.4
7-prong	γ)	-	-3.2 ± 0.2
Pairs	α)	0 ± 2	0 ± 2
	β)	-1.2 ± 0.4	-2.1 ± 0.4
	γ)	-1.9 ± 0.4	-7.0 ± 0.6

[a] The entries α, β, γ, ξ denote corrections for:

α) scanning efficiency and wide-angle-pair contamination,

β) for events outside the fiducial volume (see text),

γ) for events outside the energy selection ($2.4 < E_\gamma < 3.3$ GeV and $4.1 < E_\gamma < 5.3$ GeV at $E_\gamma = 2.8$ and 4.7 GeV respectively), and

ξ) uncertainty in the kinematic reconstruction and event identification (± 2% error in $\gamma p \to \pi^+\pi^- p$ and ξ in other 3-prongs are correlated).

of Fig. 3. weighted by the relative topology cross section. These corrections are given in Table V.

For the calculation of cross sections, the unmeasurable and remeasurable events of Table III were distributed among the different channels in the same proportions as for the measurable events. In Table VI we give the cross sections by topology and for reaction (1). In Fig. 6 the cross section for reaction (1) as measured in this experiment is shown as a function of the photon energy together with the results of previous experiments.[2,48,55] Using the previously published[1a] 1 prong cross sections found in this experiment (based on ≈ 10% of the exposure), we obtain the total cross sections given in Table VI. The results are in agreement with the preliminary values reported for this experiment.[1a]

Table VI: Cross Sections

Cross sections by topology at the average photon energies E_γ = 2.8 and 4.7 GeV for events selected in the intervals $2.4 < E_\gamma < 3.3$ GeV and $4.1 < E_\gamma < 5.3$ GeV at 2.8 and 4.7 GeV, respectively. Errors include systematic uncertainties (3% for $\gamma p \to \pi^+\pi^- p$, 2% for other topologies).

Topology	Cross Section in μb For E_γ = 2.8 GeV FWHM = 0.15 GeV	 4.7 GeV 0.45 GeV
$\gamma p \to \pi^+\pi^- p$	30.6 ± 1.2	19.9 ± 0.8
OTHER 3-prong[a]	61.1 ± 1.9	61.5 ± 1.7
5-prong	8.4 ± 0.4	19.6 ± 0.6
7-prong	0.05 ± 0.03	0.84 ± 0.08
with strange[b] particle decay	8.1 ± 0.5	8.5 ± 0.5
1-prong[c]	22.7 ± 1.5	15.6 ± 1.2
Total	131 ± 3	126 ± 3

[a] An n-prong event has n charged particles without detected strange-particle decay.

[b] Cross sections for events with strange particle decay based on 50% of total flux.

[c] Cross sections for 1-prongs taken from ref. 1a which is based on 10% of the data.

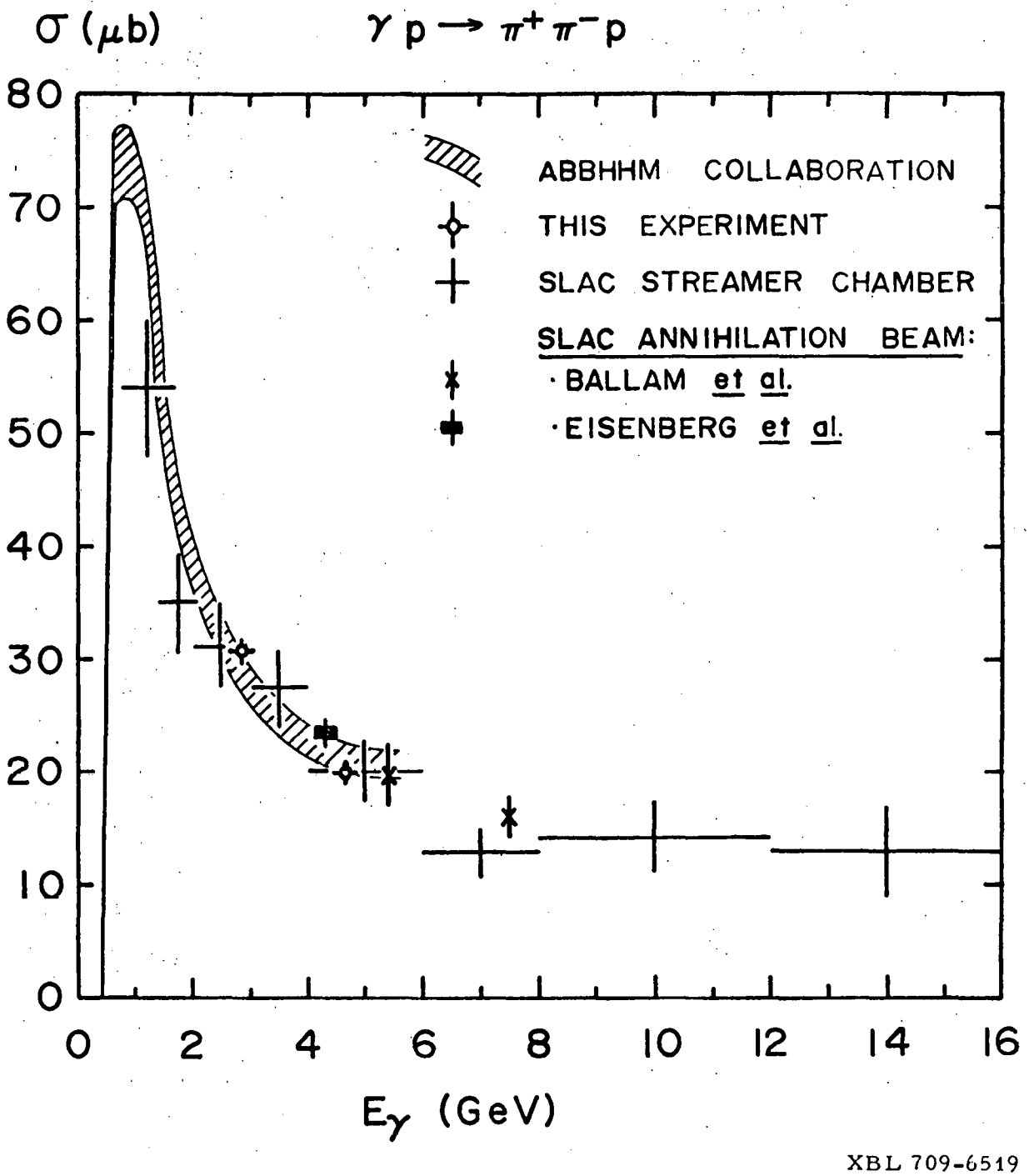

Fig. 6. Cross section versus energy for the reaction $\gamma p \rightarrow \pi^+ \pi^- p$.

IV. ρ^o PHOTOPRODUCTION IN THE REACTION $\gamma p \to \pi^+\pi^- p$

In sections IV A through D we give results for ρ^o production and decay in the reaction

$$\gamma p \to \pi^+\pi^- p \ . \qquad (1)$$

We find this reaction dominated by ρ^o production in the quasi-two body final state reaction

$$\gamma p \to \rho^o p \ .$$

A less significant feature of reaction (1) is $\Delta^{++}(1236)$ production which is discussed in section VI. The effects of contamination by wide-angle pairs and scanning losses of events with a short recoil proton in reaction (1) have been discussed in previous sections. The corrections were found to be negligible for events with $|t| > 0.02$ GeV^2 (t is the square of the four-momentum transfer between incoming and outgoing proton) and consequently, for all further studies only events with $|t| > 0.02$ GeV^2 were considered.

A. Dalitz and Chew-Low Plot Distributions

Figure 7 shows the Dalitz plot distributions at the two energies for $M^2(\pi^+p)$ vs. $M^2(\pi^+\pi^-)$, in reaction (1). A distinctive ρ^o band is clearly visible at low $M(\pi^+\pi^-)$. The

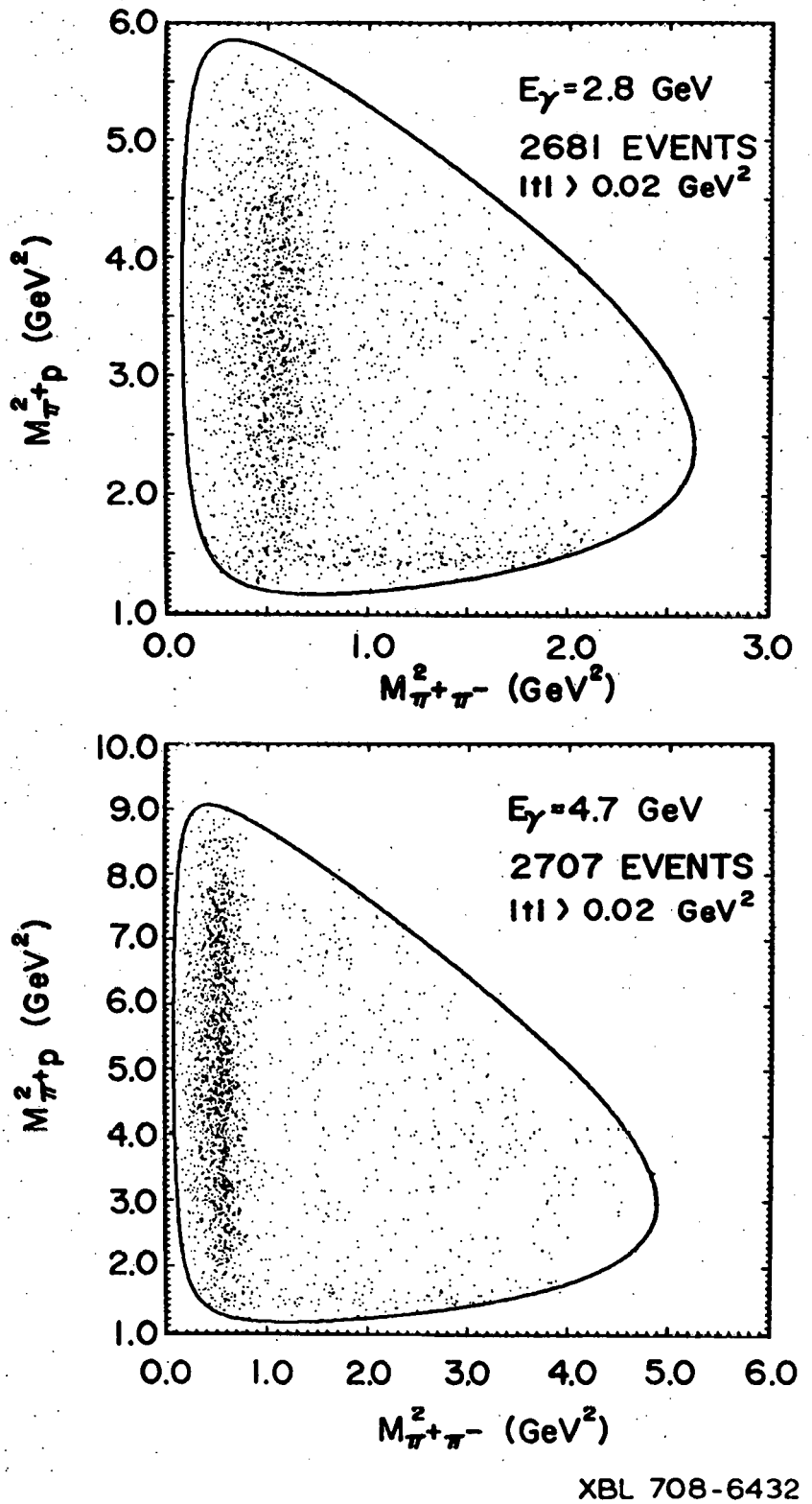

Fig. 7. Reaction $\gamma p \rightarrow \pi^+\pi^- p$: Dalitz plot density.

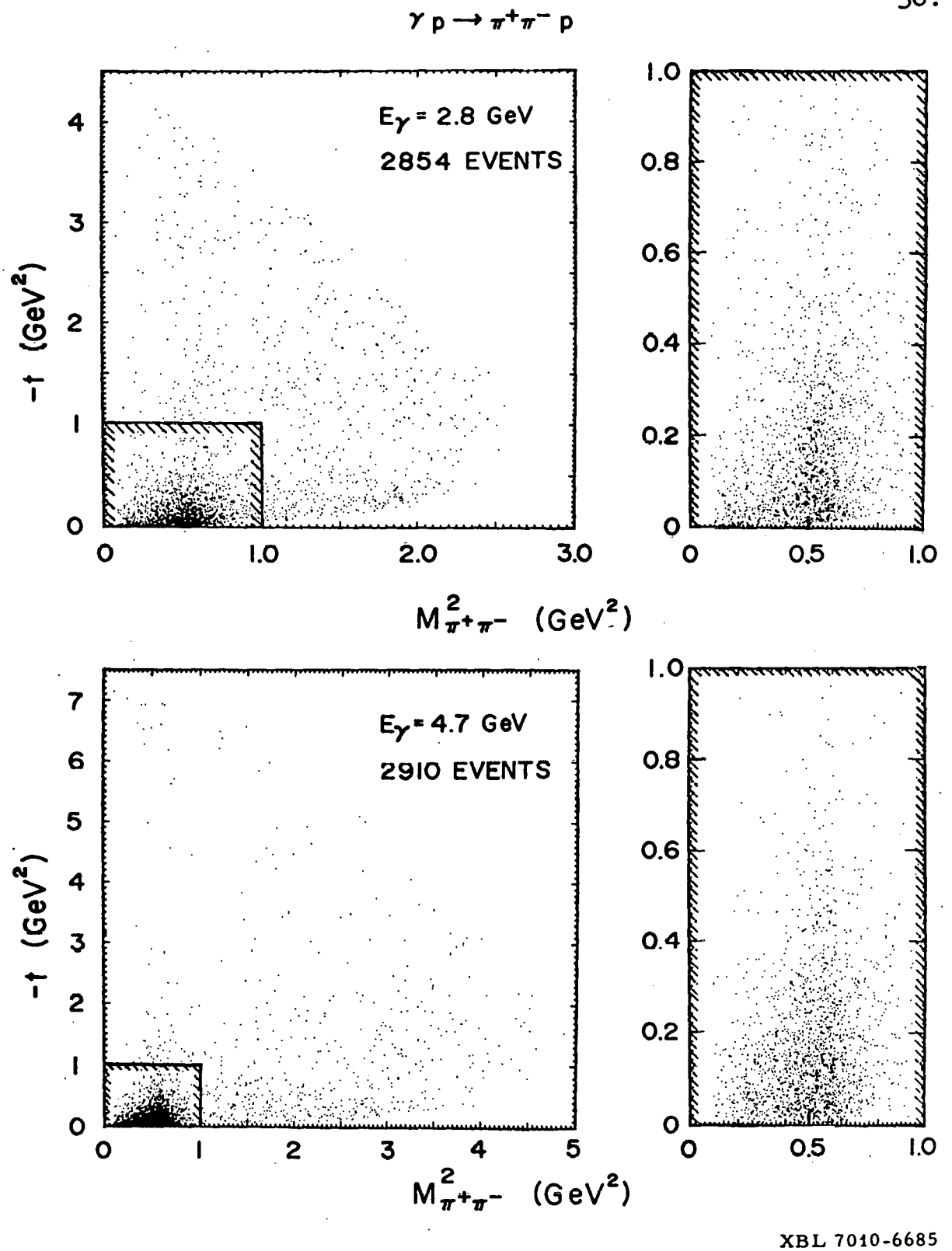

Fig. 8. Reaction $\gamma p \rightarrow \pi^+\pi^- p$: Chew-Low plot density. The shaded regions are shown on the right in an expanded scale.

$\sin^2\theta_H$ decay distribution of the ρ^o (see Section IV-C) is related to the non-uniform density of events in the ρ^o band as a function of $M^2(\pi^+p)$; at low and high $M(\pi^+p)$ there are relatively fewer events than for intermediate values. The $\Delta^{++}(1236)$ is significant at 2.8 GeV, and is less important at 4.7 GeV (see also Section VI). There appears to be no significant contributions from other resonances in the dipion or the proton-π^+ system. Little $\Delta^o(1236)$ production is found in the proton-π^- system as seen in Fig. 7.

The "Chew-Low plot" distributions (at the two energies) for $|t|$ vs. the square of the dipion mass are shown in Fig. 8. The distinctive ρ^o band is concentrated at low $|t|$. The ρ^o mass shift to low $M_{\pi\pi}$ is seen as a higher concentration of events at masses below M_ρ. It is also apparent that as $|t|$ increases the density distribution becomes more symmetric about the rho mass.

B. Cross Sections and the ρ^o Mass Shift

1. Parameterization and Model-Independent Results.

Figure 9 shows the $\pi^+\pi^-$ mass distributions. The top spectrum shows all events of reaction (1) at 2.8 GeV and 4.7 GeV; below, these distributions are repeated for the events grouped into various t intervals. The dominant feature is ρ^o production, which has the characteristic downward ρ^o mass shift found in previous photoproduction studies at CEA[3] and DESY.[4] We have looked in the $\pi^+\pi^-$ mass distributions for the

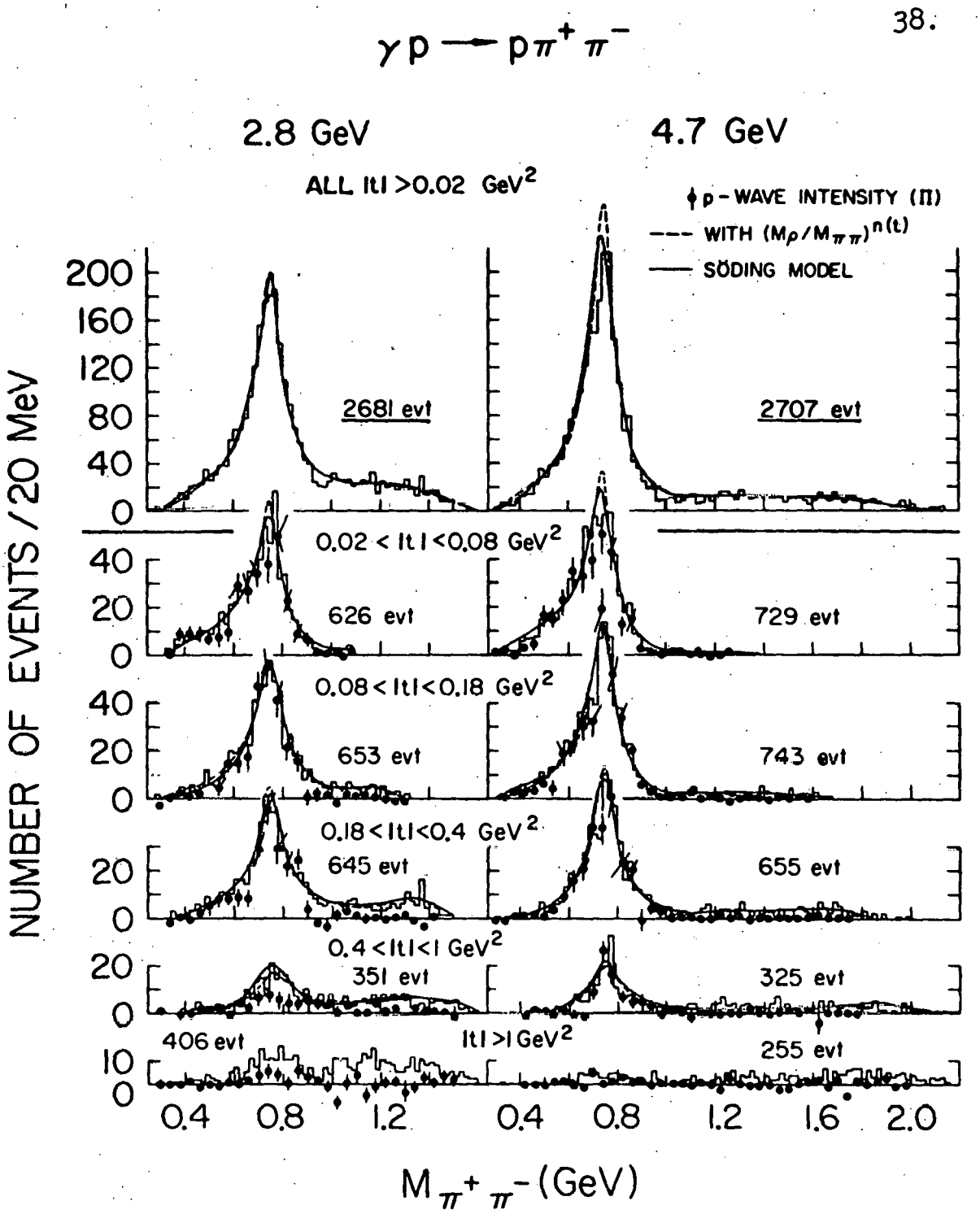

Fig. 9. Reaction $\gamma p \to \pi^+\pi^- p$: $\pi^+\pi^-$ mass distributions. The helicity conserving p-wave intensity Π (see text Eq. 5) is shown by the points ϕ. The curves give the results of a maximum likelihood fit using for the ρ^0 the parameterization $(M\rho/M\pi\pi)^{n(t)}$ (----) and the Söding model (——).

production of higher-mass mesons, in particular the vector mesons ρ' and ρ'' with mass of $\sim$ 1.3 and $\sim$ 1.7 GeV predicted by J. Shapiro[49] using the Veneziano model. The upper limits (1 σ) on their production cross sections at 4.7 GeV are 0.5 μb and 0.4 μb, respectively, assuming for both ρ' and ρ'' a width of 200 MeV and decay into $\pi^+\pi^-$ only. These upper limits agree with other experiments[6] but are still consistent with a recent Veneziano model calculation by Satz and Schilling.[50]

In the past, good fits to the $\pi^+\pi^-$ mass distributions were obtained (ABBHHM)[4] by multiplying the Breit-Wigner distribution with an energy dependent width according to Jackson[51] for the ρ^o by a mass-skewing factor $[M_\rho/M_{\pi\pi}]^4$ from the diffraction dissociation model of Ross and Stodolsky.[10] In order to test the Ross-Stodolsky factor we have multiplied the p-wave Breit-Wigner for the ρ^o by the factor $[M_\rho/M_{\pi\pi}]^{n(t)}$. Maximum likelihood fits were then made to the events of reaction (1) assuming the density distribution

$$dP(M^2_{\pi+p}, M^2_{\pi^+\pi^-}, t, t_\Delta) = \Big[f_\Delta \, N_\Delta BW_\Delta(M_\Delta, \Gamma_\Delta) \, e^{7.1\, t_\Delta}$$

$$+ f_\rho \, N_\rho \, BW_\rho(M_\rho, \Gamma_\rho) \, W(\cos\theta_H) \left[\frac{M_\rho}{M_{\pi^+\pi^-}}\right]^{n(t)} e^{A\rho t} \qquad (2)$$

$$+ (1 - f_\Delta - f_\rho) \cdot N_{PS} \cdot 1 \Big] \; d(\text{Phase Space})$$

where M_{π^+p} = π^+p invariant mass, t_Δ = square of the momentum transfer between incoming proton and the outgoing (π^+p) system. The parameters f_Δ and f_ρ are the fractions of events of $\Delta^{++}(1236)$ and ρ^o to be determined. $BW_\Delta(M_{\rho\pi^+})$ and $BW_\rho(M_{\pi^+\pi^-})$ are the resonant distributions for Δ^{++} and ρ^o,

$$BW_x(M) = \frac{M}{q(M)} \frac{\Gamma(M)}{(M^2 - M_o^2)^2 + M_o^2 \Gamma^2(M)} , \qquad (2.1)$$

$$\Gamma(M) = \Gamma_o \left(\frac{q(M)}{q(M_o)}\right)^3 \frac{\rho(M)}{\rho(M_o)} . \qquad (2.2)$$

ρ^o production:

$x = \rho$

$M = M_{\pi^+\pi^-}$

$M_o = M_\rho$ (parameter)

$\Gamma_o = \Gamma_\rho$ (parameter)

$q(M)$ = 3-momentum of the π^+ in the $\pi\pi$ rest system

$\rho(M) = \{q^2(M) + q^2(M_o)\}^{-1}$

Δ^{++} production:

$x = \Delta$

$M = M_{p\pi^+}$

M_o = 1236 MeV

Γ_o = 120 MeV

$q(M)$ = 3-momentum of the proton in the $p\pi^+$ rest system

$\rho(M) = \{2.2\ M_\pi^2 + q^2(M)\}^{-1}$

M_π = pion mass

The normalization N_Δ, N_ρ, and N_{PS} were determined by Monte Carlo integration. $W(\cos\theta_H) = 3/4 \sin^2\theta_H$ describes the θ dependence of the ρ^o decay distribution in the helicity system. The factor $\exp(7.1\ t_\Delta)$ approximates the t_Δ distribution of the $\Delta^{++}(1236)$. A brief description of the maximum liklihood fitting program can be found in Appendix B.

The contributions from the Δ^{++}, ρ^o and phase space together with the parameter n(t) were determined in the fit as a function of t. The fits described the $\pi^+\pi^-$ mass spectra well, as shown by the dashed curves in Fig. 9. The fitted values for n(t) are shown in Fig. 10 and Table VII. In contrast to the prediction of Ross and Stodolsky, namely $n(t = 0) = 4$, the parameter n is > 5 near $t = 0$; it drops to zero around $|t| = 0.5$ GeV^2.

Table VII: The parameter n(t) in the factor $\{M_\rho/M_{\pi\pi}\}^{n(t)}$ at 2.8 and 4.7 GeV. Results are also plotted in Fig. 10.

-t (GeV^2)	2.8 GeV	4.7 GeV
0.02 - 0.08	5.3 ± 0.3	5.3 ± 0.3
0.08 - 0.18	4.5 ± 0.3	4.9 ± 0.3
0.18 - 0.4	3.5 ± 0.4	2.8 ± 0.3
0.4 - 1.0	1.0 ± 0.9	0.3 ± 0.6

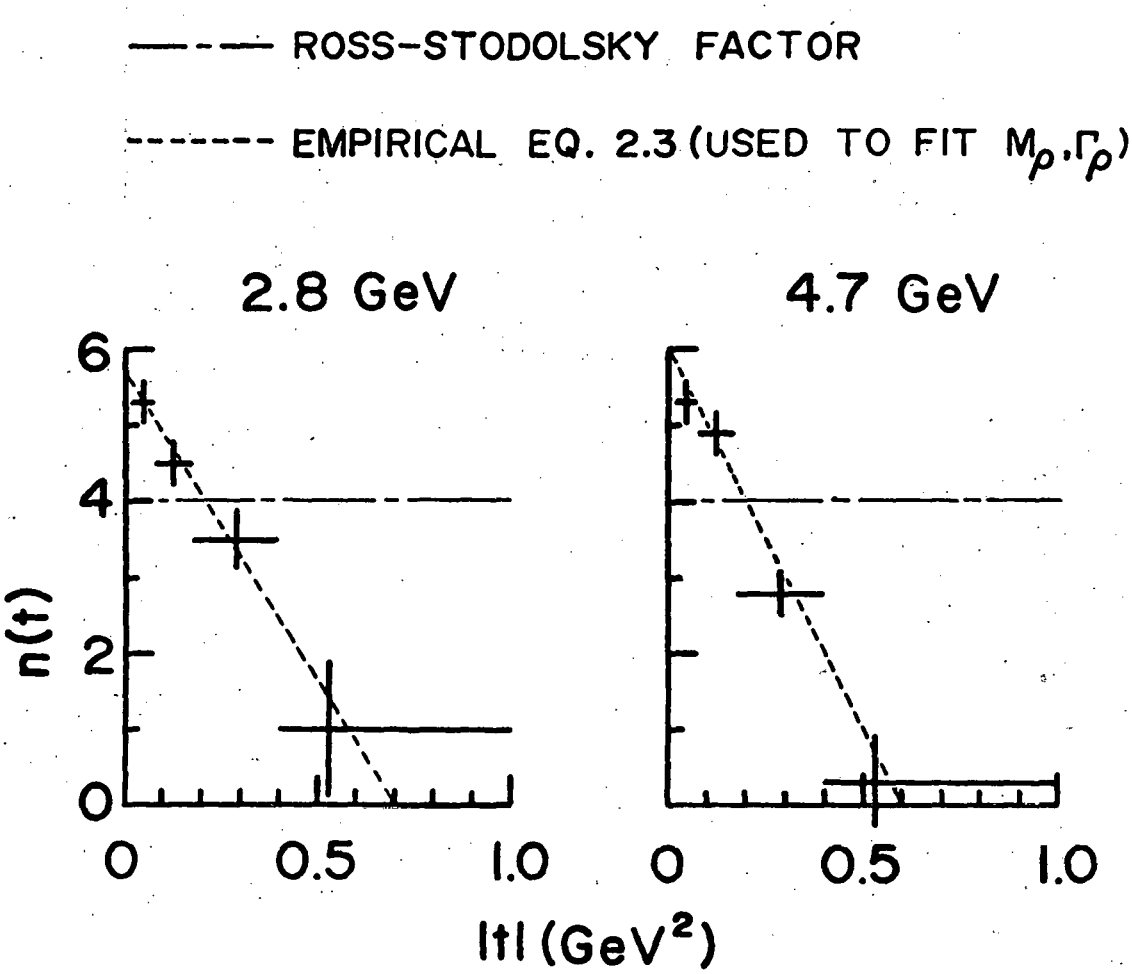

XBL 708-6433

Fig. 10. Fitted values for n(t) in the parameterization $(M_\rho/M_{\pi\pi})^{n(t)}$ as the mass skewing factor for the reaction $\gamma p \rightarrow \rho^o p$. For numerical values see Table VII.

For comparison, the curves corresponding to n(t) = 4 and the fitted value n(t) = 5.3 (see Table VII) are shown in Fig. 11 for the lowest t bin ($0.02 < |t| < 0.08$ GeV^2). The dashed line gives the fit results of n(t) (confidence level ≈ 30%), and is far better than that obtained with the factor n(t) = 4 shown as a solid line (confidence level < 0.1%).

The parameter n(t) was determined again allowing for ρ^o-ω interference (see Section V) by modulating the ρ^o amplitude by the factor $\mathcal{F}$ of Eq. 11 Section V. The mass mixing parameters were set at the values δ = 2.5 MeV and β = 0 degrees. No change was found for n(t) (for $0.02 < |t| < 0.08$ GeV^2 n(t) = 5.25 ± 0.3). This result is not surprising because the ρ^o-ω interference only affects appreciably the $\pi\pi$ mass distribution from 750 - 810 MeV. However, the factor $(M_\rho / M_{\pi\pi})^{n(t)}$ is most strongly influenced by the signals for $M_{\pi\pi}$ < 650 MeV and > 850 MeV.

A test was made to determine what influence the energy dependent width had on the determination of n(t). Replacing the Jackson form of Eq. 2.2 by a constant width in the Breit-Wigner of Eq. 2.1 we determined again the values of n(t), M_ρ, and Γ_ρ. For the lowest t bin ($0.02 < |t| < 0.08$ GeV^2) we obtain n(t) ≈ 4, however the predicted $\pi^+\pi^-$ mass spectrum does not agree with the data (confidence level < 0.01%); too much signal is predicted at low $M_{\pi\pi}$.

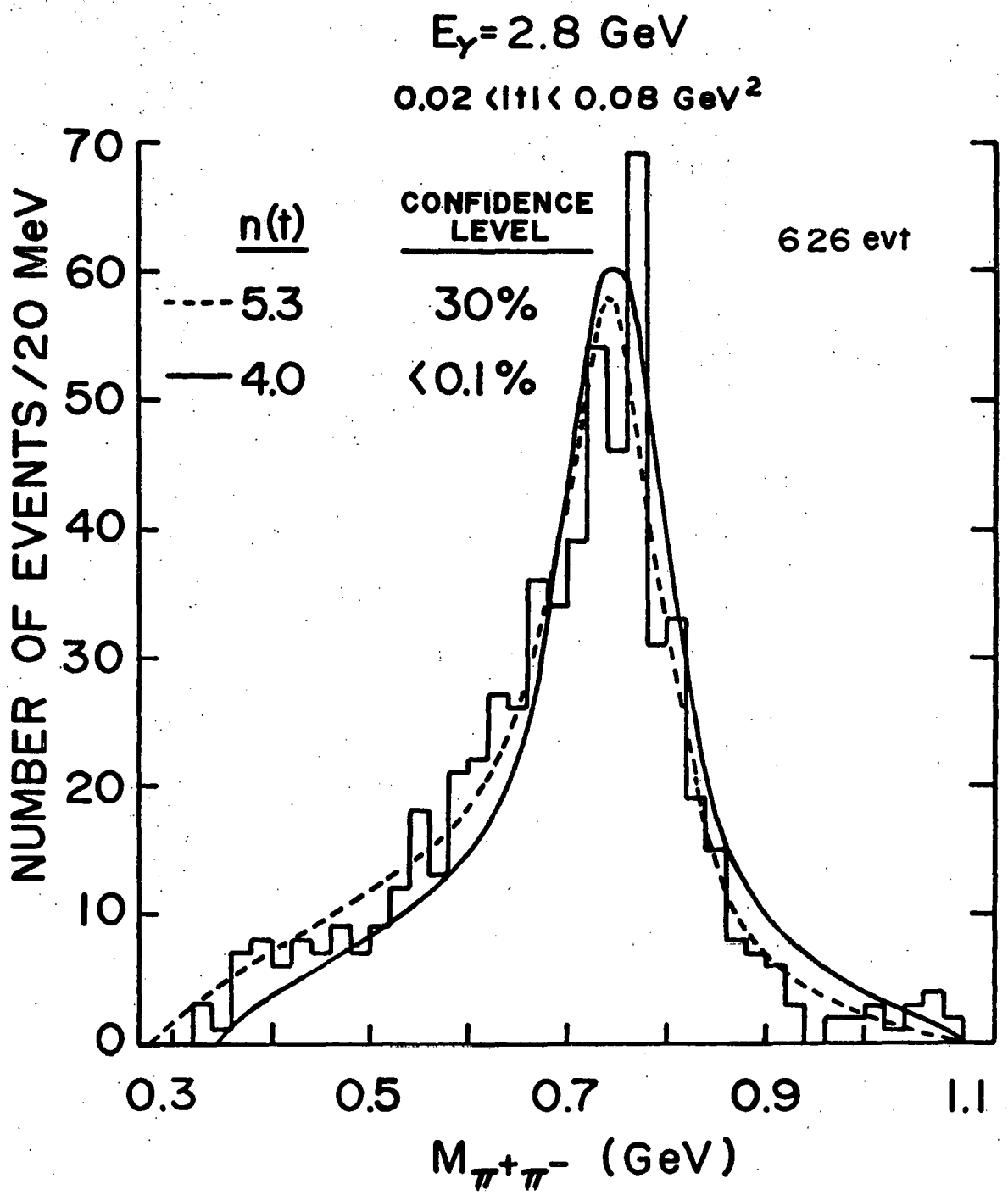

Fig. 11. Reaction $\gamma p \rightarrow \pi^+\pi^- p$: $M_{\pi^+\pi^-}$ at 2.8 GeV for events with $0.02 < |t| < 0.08$ GeV^2 (data of Fig.9). The curves show the results of maximum likelihood fits using Eq. 2 with the parameterization $(M\rho/M\pi\pi)^{n(t)}$ for n(t) = 4 (Ross-Stodolsky factor) and the optimum value n(t) = 5.3.

To determine the rho mass and width we approximate the n(t) dependence of Fig. 10 at

$$\begin{aligned} &2.8 \text{ GeV by } n(t) = 5.6 + 8t \text{ for } |t| < 0.7 \text{ GeV}^2, \\ &\qquad n(t) = 0 \text{ for } |t| > 0.7 \text{ GeV}^2; \\ &4.7 \text{ GeV by } n(t) = 6 + 10t \text{ for } |t| < 0.6 \text{ GeV}^2, \\ &\qquad n(t) = 0 \text{ for } |t| > 0.6 \text{ GeV}^2 . \end{aligned} \tag{2.3}$$

The parameters M_ρ, Γ_ρ and A_ρ of Eq. 2 (with the Jackson form for the ρ width, Eq. 2.2) were then determined in the maximum likelihood fit for events in the lowest three t bins ($0.02 < |t| < 0.4$ GeV^2) which contain $\approx 75\%$ of the events of Reaction (1). We obtained for the rho mass and width the values (766 ± 3), (145 ± 6) and (762 ± 3), (141 ± 5) MeV for 2.8 and 4.7 GeV, respectively. The values obtained for the exponential slope, A_ρ, were (6.36 ± 0.30) and (6.31 ± 0.26) GeV^{-2} for the two energies.

In Fig. 12 we give the exponential slope of the t distribution as a function of the $\pi^+\pi^-$ mass.[4] The slope, A, was obtained by fitting the events in a given $\pi^+\pi^-$ mass bin with $0.02 < |t| < 0.4$ GeV^2 to the form

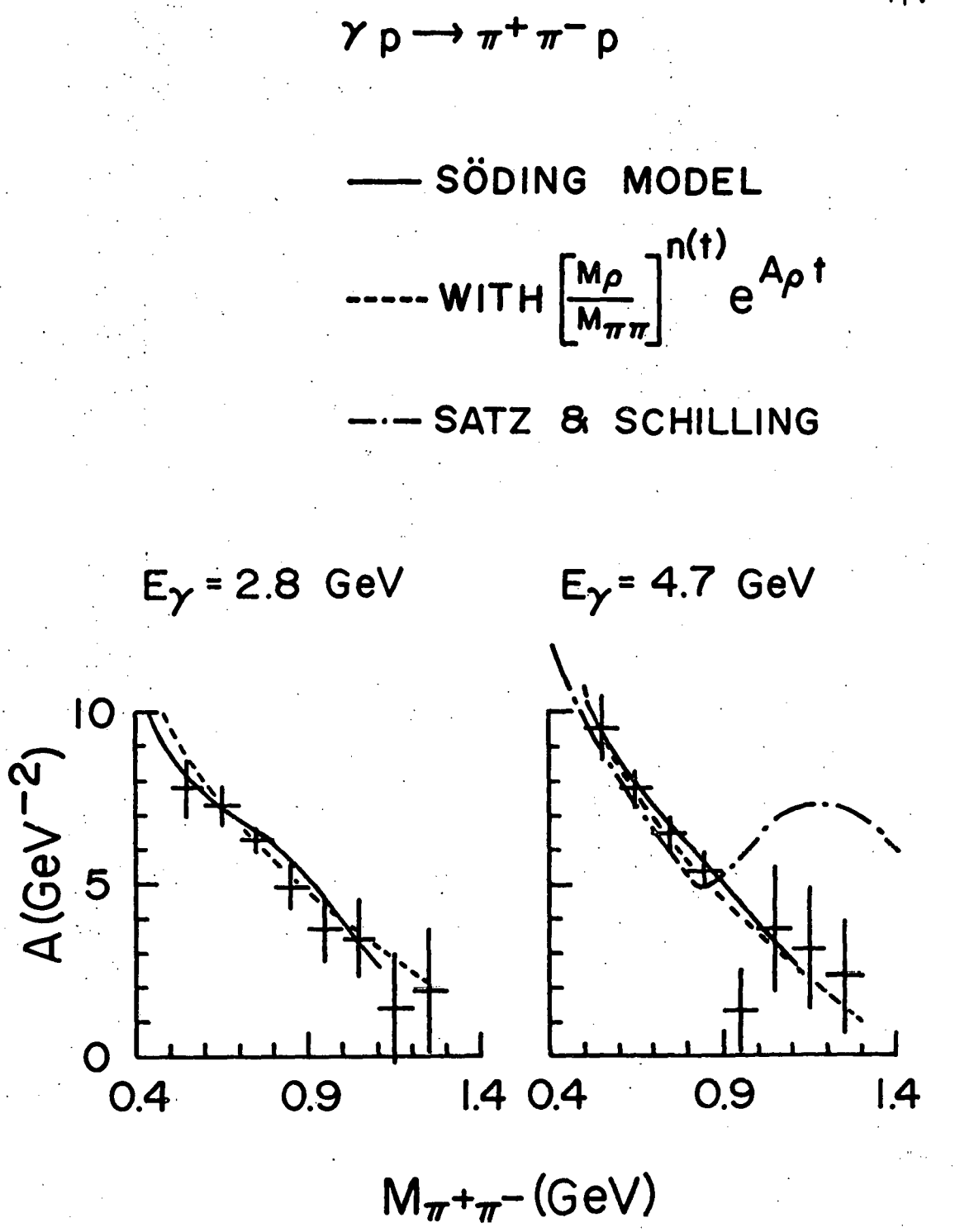

Fig. 12. Reaction $\gamma p \rightarrow \pi^+ \pi^- p$: Exponential Slope of the t distribution as a function of the $\pi^+\pi^-$ mass taking all events in a given $\pi^+\pi^-$ mass bin with $0.02 < |t| < 0.4$ GeV^2. The curves show the prediction of the Söding Model, Satz and Schilling (Ref. 50), and $A(M_{\pi\pi})$ of Eq. 3.

$$\frac{d\sigma}{dt}\,(M_{\pi\pi}) \propto e^{A(M_{\pi\pi})t}.$$

The strong variation of A with the $\pi^+\pi^-$ mass is related to the t dependence of the $\pi^+\pi^-$ mass distributions, i.e. n(t). This can be seen by writing the density distribution of Eq. 2 in the form

$$\frac{d\sigma}{dt}\,(t,M_{\pi\pi}) = B(M_{\pi\pi})\left(\frac{M_\rho}{M_{\pi\pi}}\right)^{n(t)} e^{A_\rho t} +$$

contributions from Δ^{++} and constant background. Assuming $A_\rho = 6.3\ \text{GeV}^{-2}$, $n(t) = \alpha + \beta t$, neglecting contributions from Δ^{++} and constant background, and taking the ln; we find

$$\ell n\,\frac{d\sigma}{dt} = \ell n\left[B(M_{\pi\pi})\cdot\left(\frac{M_\rho}{M_{\pi\pi}}\right)^{\alpha}\right] + \left[\beta\ \ell n\ (M_\rho/M_{\pi\pi}) + A_\rho\right]t\ .$$

The linear term in t is

$$A(M_{\pi\pi}) = \beta\ \ell n\ (M_\rho/M_{\pi\pi}) + A_\rho\ . \qquad (3)$$

Using β obtained from the approximate n(t) behavior found in this experiment (see Eq. 2.3 and Fig. 10), we show by the dashed curves of Fig. 12 $A(M_{\pi\pi})$ obtained from Eq. 3. $A(M_{\pi\pi})$ describes well the dependence of the exponential slope of the t distribution on the $\pi^+\pi^-$ mass.

The total ρ^o production cross section in Reaction (1) obtained by fitting with the parametrization $(M_\rho/M_{\pi\pi})^{n(t)}$ and correcting for the interval $|t| < 0.02$ GeV^2 is given in Table VIII (middle).

The analysis of the ρ^o decay in this experiment shows (see Section IV-C) that for $|t| < 0.4$ GeV^2 the ρ^o decay angular distribution is

$$W(\theta,\psi) = \frac{3}{8\pi}\left\{\sin^2\theta + P_\gamma \sin^2\theta \cos 2\psi\right\} . \qquad (4)$$

The angles are sketched in Fig. 18; θ is the polar angle of the decay π^+, ψ is the polarization angle defined as $\psi = \phi - \Phi$, where ϕ is the azimuthal angle of the π^+ with respect to the production plane, Φ is the angle between the photon electric vector and the production plane, and P_γ is the degree of linear polarization of the photon. All angles are calculated in the $\pi^+\pi^-$ helicity system. Equation 4 can be expressed in terms of the moments $Y_0^0(\theta)$, $Y_2^0(\theta)$ and Re $Y_2^2(\theta,\psi)$:

Table VIII: Total cross sections for $\gamma p \rightarrow p\pi^+\pi^-$; total and forward differential cross sections and slope A for production of $\pi^+\pi^-$ pairs in the s-channel c.m. helicity conserving p-wave state (Π) and for ρ^o production as determined from fits with the parameterization $(M\rho/M\pi\pi)^{n(t)}$ and the Söding model.

E_γ (GeV)	σ (μb)	$\frac{d\sigma}{dt}(t=0)$ (μb/GeV^2)	A (GeV^{-2})
	hel. cons. p-wave (Π)		
2.8	18.4 ± 1.1	144 ± 12	7.5 ± 0.6
4.7	14.0 ± 1.0	99 ± 7	7.1 ± 0.5
	ρ^o production with parameterization $[M\rho/M\pi\pi]^{n(t)}$		
2.8	20.8 ± 1.0	138 ± 8	6.6 ± 0.3
4.7	15.6 ± 0.7	106 ± 5	7.0 ± 0.3
	ρ^o production with Söding model		
2.8	18.3 ± 1.0	97 ± 7	5.3 ± 0.4
4.7	15.3 ± 0.7	88 ± 5	5.8 ± 0.3

$$W(\theta,\psi) = \frac{1}{\sqrt{4\pi}} Y_0^0(\theta) - \frac{1}{\sqrt{20\pi}} Y_2^0(\theta) + 2 P_\gamma \sqrt{\frac{3}{40\pi}} \text{Re } Y_2^2(\theta,\psi) \quad (4.1)$$

Because of its ψ dependence, Re $Y_2^2(\theta,\psi)$ is the least affected by background and therefore has been used to determine the s-channel c.m. helicity - conserving p-wave $\pi\pi$ intensity Π. Integrating Re Y_2^2 over Eq. 4 (or 4.1), we find

$$\begin{aligned} \Pi &= \frac{1}{P_\gamma} \sqrt{\frac{40\pi}{3}} \sum_i \text{Re } Y_2^2(\theta_i,\psi_i) \\ &= 2.5 \sum_i \frac{1}{P_\gamma} \sin^2\theta_i \cos 2\psi_i \end{aligned} \quad (5)$$

where the summation is over all events. The dots marked on the histograms of Fig. 9 show Π is a function of $M_{\pi\pi}$ for different t-intervals. We notice that a) in the ρ region Π accounts for almost all events and shows the same skewing as the mass distributions; b) above $M_{\pi\pi}$ = 1 GeV, Π is zero within errors, again emphasizing the absence of higher vector mesons; this also shows that the background which is present above 1 GeV does not contribute to Re Y_2^2. The total helicity-conserving p-wave cross section (corrected for the interval $|t| < 0.02$ GeV^2) is given at the top of Table VIII.

We have also studied the $\pi^+\pi^-$ mass dependence of other $Y_L^M(\theta,\psi)$ moments. In Fig. 13 we show the moments Y_0^0 to Y_4^0 and Y_6^0. The Y_2^0 moment shows the behavior expected for the $\sin^2\theta$ decay of the ρ^0. The slightly positive values of Y_2^0 above

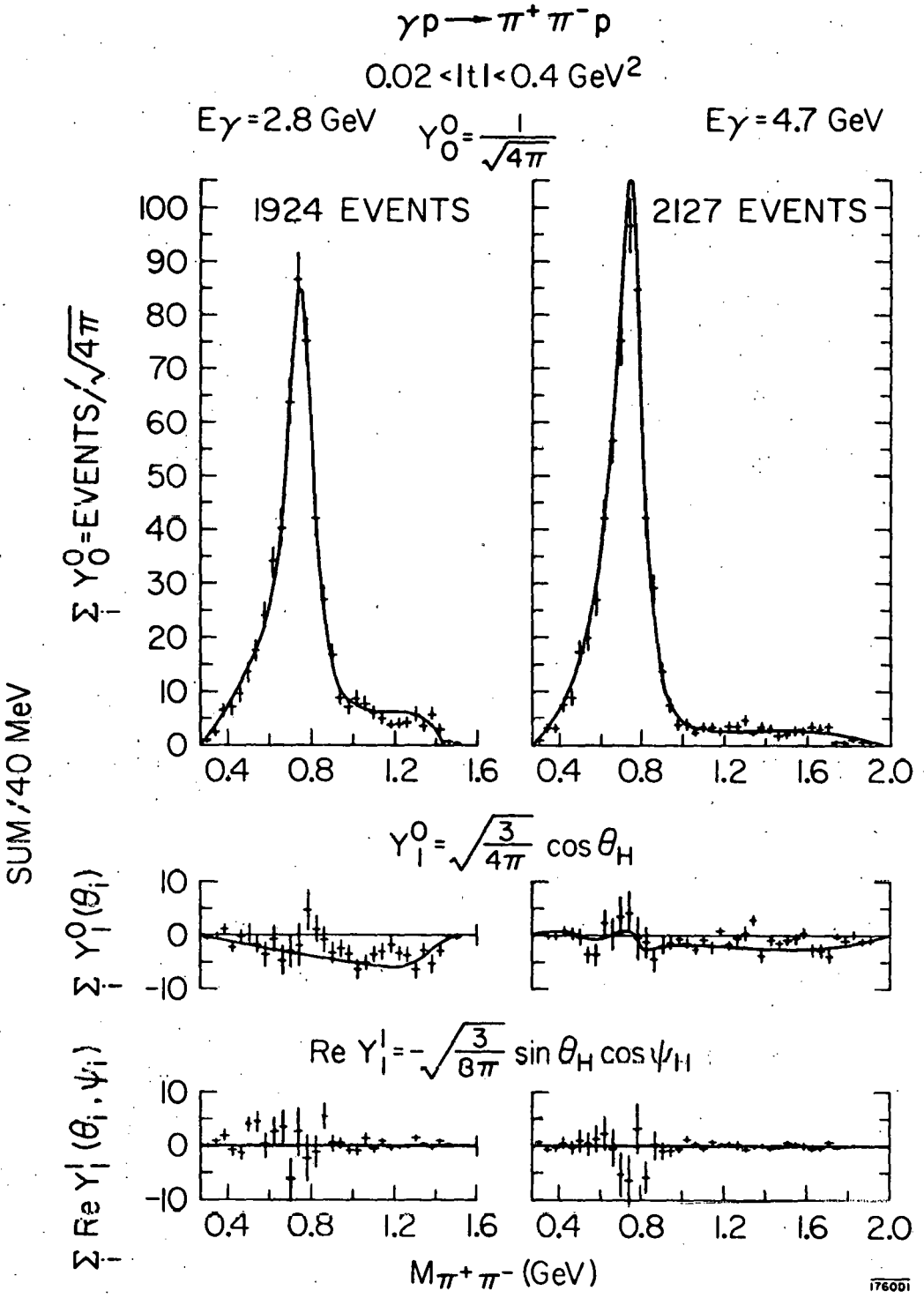

Fig. 13. (a) Reaction $\gamma p \rightarrow \pi^+\pi^- p$: The moments Y_0^0, $Y_1^0(\theta)$ and $Y_1^1(\theta, \psi)$ in the helicity frame as a function of $M_{\pi\pi}$ for $0.02 < |t| < 0.4$ GeV^2. The curves show the results of the Söding Model.

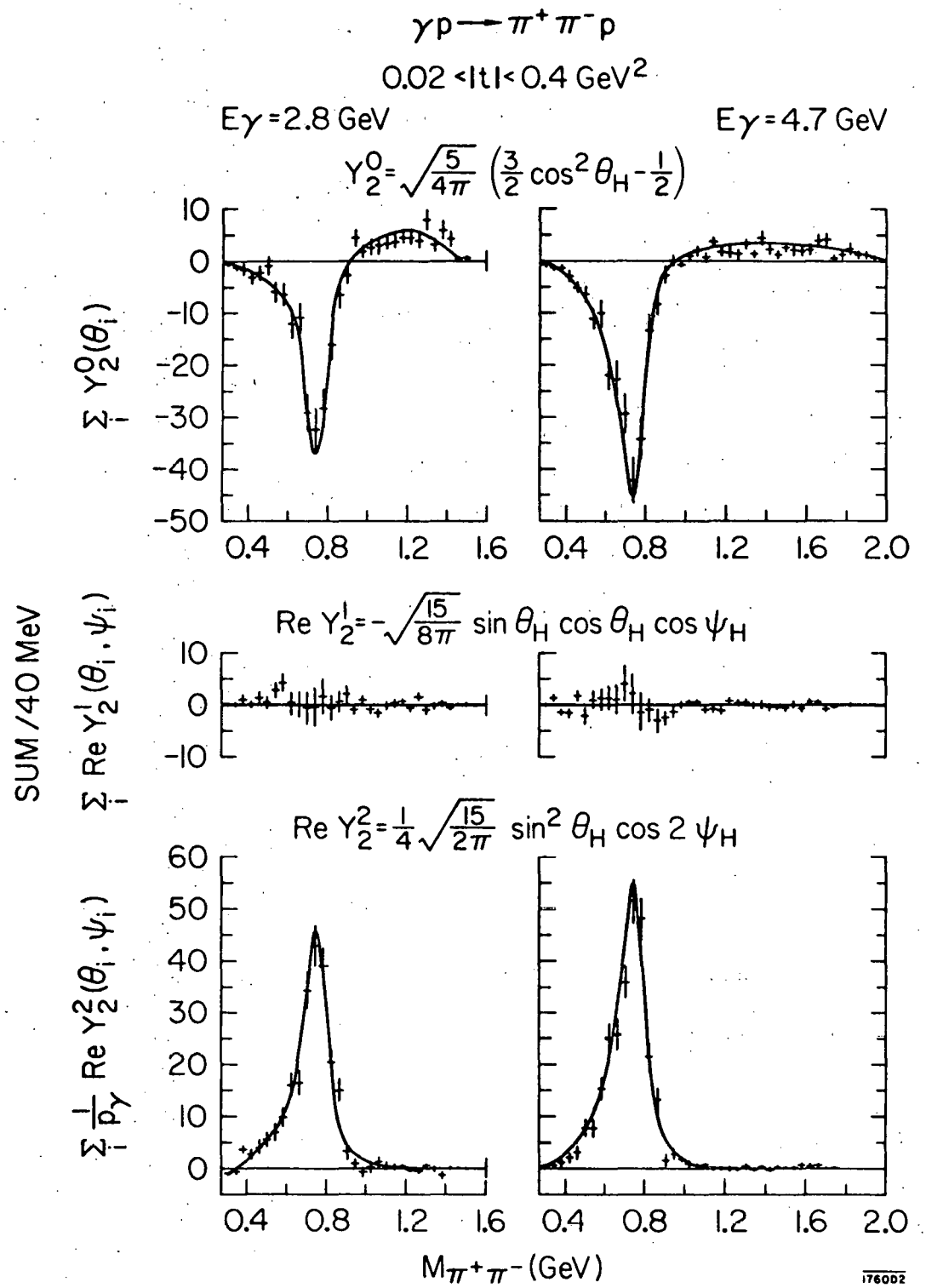

Fig. 13. (b) Reaction $\gamma p \to \pi^+\pi^- p$: The moments $Y_2^0(\theta)$, $Y_2^1(\theta,\psi)$, and $Y_2^2(\theta,\psi)$ in the helicity frame as a function of $M_{\pi\pi}$ for $0.02 < |t| < 0.4$ GeV^2. The curves show the results of the Söding Model.

Fig. 13. (c) Reaction $\gamma p \to \pi^+ \pi^- p$: The moments $Y_3^0(\theta)$, $Y_3^1(\theta, \psi)$, $Y_3^2(\theta, \psi)$, $Y_3^3(\theta, \psi)$, $Y_4^0(\theta)$, and $Y_6^0(\theta)$ in the helicity frame as a function of $M_{\pi\pi}$ for $0.02 < t < 0.4$ GeV^2. The curves show the results of the Söding Model.

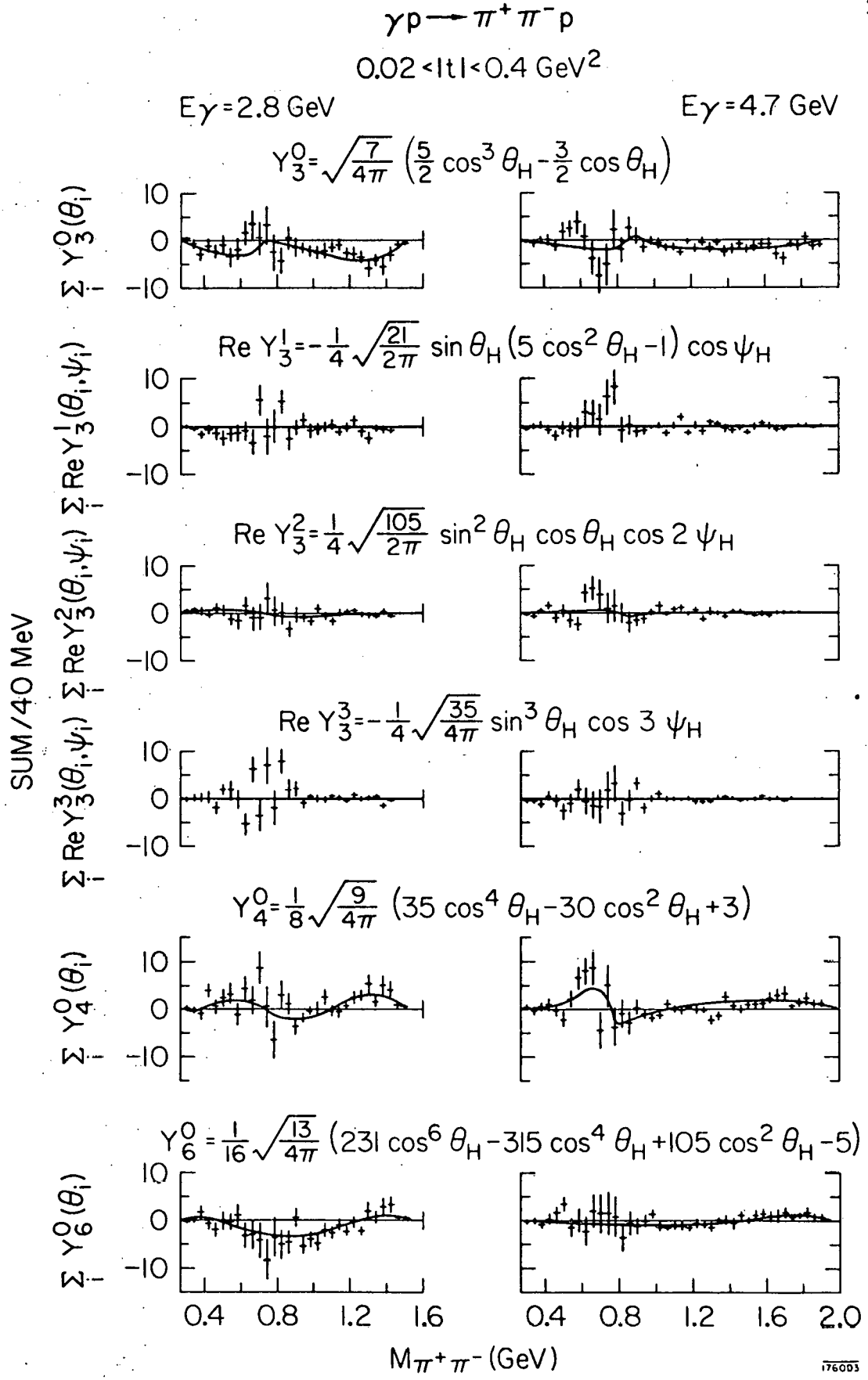
γp → π⁺π⁻p
0.02 < |t| < 0.4 GeV²
Eγ = 2.8 GeV
Eγ = 4.7 GeV
$Y_3^0 = \sqrt{\frac{7}{4\pi}}\left(\frac{5}{2}\cos^3\theta_H - \frac{3}{2}\cos\theta_H\right)$
$\mathrm{Re}\, Y_3^1 = -\frac{1}{4}\sqrt{\frac{21}{2\pi}}\sin\theta_H(5\cos^2\theta_H - 1)\cos\psi_H$
$\mathrm{Re}\, Y_3^2 = \frac{1}{4}\sqrt{\frac{105}{2\pi}}\sin^2\theta_H\cos\theta_H\cos 2\psi_H$
$\mathrm{Re}\, Y_3^3 = -\frac{1}{4}\sqrt{\frac{35}{4\pi}}\sin^3\theta_H\cos 3\psi_H$
$Y_4^0 = \frac{1}{8}\sqrt{\frac{9}{4\pi}}(35\cos^4\theta_H - 30\cos^2\theta_H + 3)$
$Y_6^0 = \frac{1}{16}\sqrt{\frac{13}{4\pi}}(231\cos^6\theta_H - 315\cos^4\theta_H + 105\cos^2\theta_H - 5)$
SUM/40 MeV
$\sum_i Y_3^0(\theta_i)$
$\sum_i \mathrm{Re}\, Y_3^1(\theta_i,\psi_i)$
$\sum_i \mathrm{Re}\, Y_3^2(\theta_i,\psi_i)$
$\sum_i \mathrm{Re}\, Y_3^3(\theta_i,\psi_i)$
$\sum_i Y_4^0(\theta_i)$
$\sum_i Y_6^0(\theta_i)$
10
0
−10
0.4
0.8
1.2
1.6
2.0
$M_{\pi^+\pi^-}$ (GeV)
176003

Fig. 13

1 GeV are due to the Δ^{++} reflection. The moment Y_4^0 shows a distinctive interference pattern in the ρ region at 4.7 GeV which can be interpreted as an interference between the ρ^0 and a $\pi^+\pi^-$ partial wave state of spin $J \geq 3$. At 2.8 GeV the moment Y_4^0 does not show a statistically significant interference effect. This is due to the large Δ^{++} production, which plays only a minor role at 4.7 GeV.

Figure 14 and Table IX show the differential cross sections $d\sigma/dt$ for ρ^0 production from an independent maximum likelihood fit separately for each t-interval with the density distribution of equation 2. For these fits the exponential t-dependence for the ρ^0 and Δ^{++} was removed, and we used for n(t) the linear behavior of Eq. 2.3. Also shown in Fig. 14 and Table IX are the differential cross sections for the helicity-conserving p-wave state, Π. Fitting the differential cross section values for $|t| < 0.4$ GeV^2 to the form

$$\frac{d\sigma}{dt} = \frac{d\sigma}{dt}/(t = 0)\ e^{At}$$

we obtain $d\sigma/dt$ $(t = 0)$ and A as given in Table VIII.[56] For $|t| < 0.4$ GeV^2 the differential cross sections and the slopes obtained for $\Pi(t)$ and for the ρ^0 fitted with the parameterization $(M_\rho/M_{\pi\pi})^{n(t)}$ agree within errors.

Table IX: Differential cross sections for production of $\pi^+\pi^-$ pairs in the s-channel c.m. helicity conserving p-wave state (7) and for ρ^o production with the parameterization $[M_\rho/M_{\pi\pi}]^{n(t)}$ and ρ^o production using the Söding model* at 2.8 and 4.7 GeV. Results are plotted in Fig. 14.

$-t$ (GeV^2)	$d\sigma/dt$ (μb/GeV^2)					
	E_γ = 2.8 GeV			E_γ = 4.7 GeV		
	Π	ρ^o with $(M_\rho/M_{\pi\pi})^{n(t)}$	ρ^o(Söding)	Π	ρ^o with $(M_\rho/M_{\pi\pi})^{n(t)}$	ρ^o(Söding)
0.02 - 0.05	120 ± 11	121 ± 9	80 ± 7	73 ± 7	85 ± 6	71 ± 4
0.05 - 0.075	88 ± 10	92 ± 8	69 ± 7	63 ± 7	72 ± 5	61 ± 5
0.075 - 0.10	67 ± 10	74 ± 7	63 ± 7	51 ± 6	54 ± 4	51 ± 5
0.10 - 0.15	56 ± 6	55 ± 4	50 ± 5	44 ± 4	45 ± 3	45 ± 3
0.15 - 0.20	36 ± 5	43 ± 4	42 ± 4	36 ± 4	35 ± 2.5	36 ± 3
0.20 - 0.25	29 ± 4	33 ± 3	28 ± 4	16 ± 3	18.7 ± 1.6	21.3 ± 2.1
0.25 - 0.30	19 ± 4	21 ± 3	24 ± 4	13 ± 3	17.7 ± 1.5	20.6 ± 2.2
0.30 - 0.35	15 ± 4	17 ± 2	18 ± 3	9.0 ± 2.2	11.0 ± 1.1	13.5 ± 1.6
0.35 - 0.40	7.7 ± 3.0	12 ± 2	13 ± 2	6.7 ± 1.8	8.4 ± 1.0	9.2 ± 1.5
0.40 - 0.50	4.3 ± 1.5	5.6 ± 1.1	7.2 ± 1.3	5.5 ± 1.1	5.7 ± 0.6	6.5 ± 1.0
0.50 - 0.70	3.2 ± 0.8	2.6 ± 0.6	2.9 ± 0.7	0.6 ± 0.5	2.2 ± 0.3	2.6 ± 0.5
0.7 - 1.0	1.0 ± 0.6	2.2 ± 0.4		0.9 ± 0.3	0.77 ± 0.16	
1.0 - 1.5	0.7 ± 0.4	0.74 ± 0.22		0.15 ± 0.20	0.33 ± 0.08	
1.5 - 2.5	0. ± 0.17	0.17 ± 0.09		0.20 ± 0.09	0.066 ± 0.027	
2.5 - t_{MAX}	0. ± 0.11	0.23 ± 0.08		0.015 ± 0.013	0.016 ± 0.008	

* The differential cross sections for $|t| > 0.7$ GeV^2 were determined by describing ρ^o production by a p-wave Breit-Wigner.

Fig. 14. Reaction $\gamma p \rightarrow \pi^+ \pi^- p$: Differential cross sections as a function of t for the helicity-conserving p-wave contribution Π, for ρ^o production as obtained from fits with the Söding model and using the parameterization $(M_\rho / M_{\pi\pi})^{n(t)}$. The shaded regions are shown on an expanded scale at the top. For numerical values see Table IX.

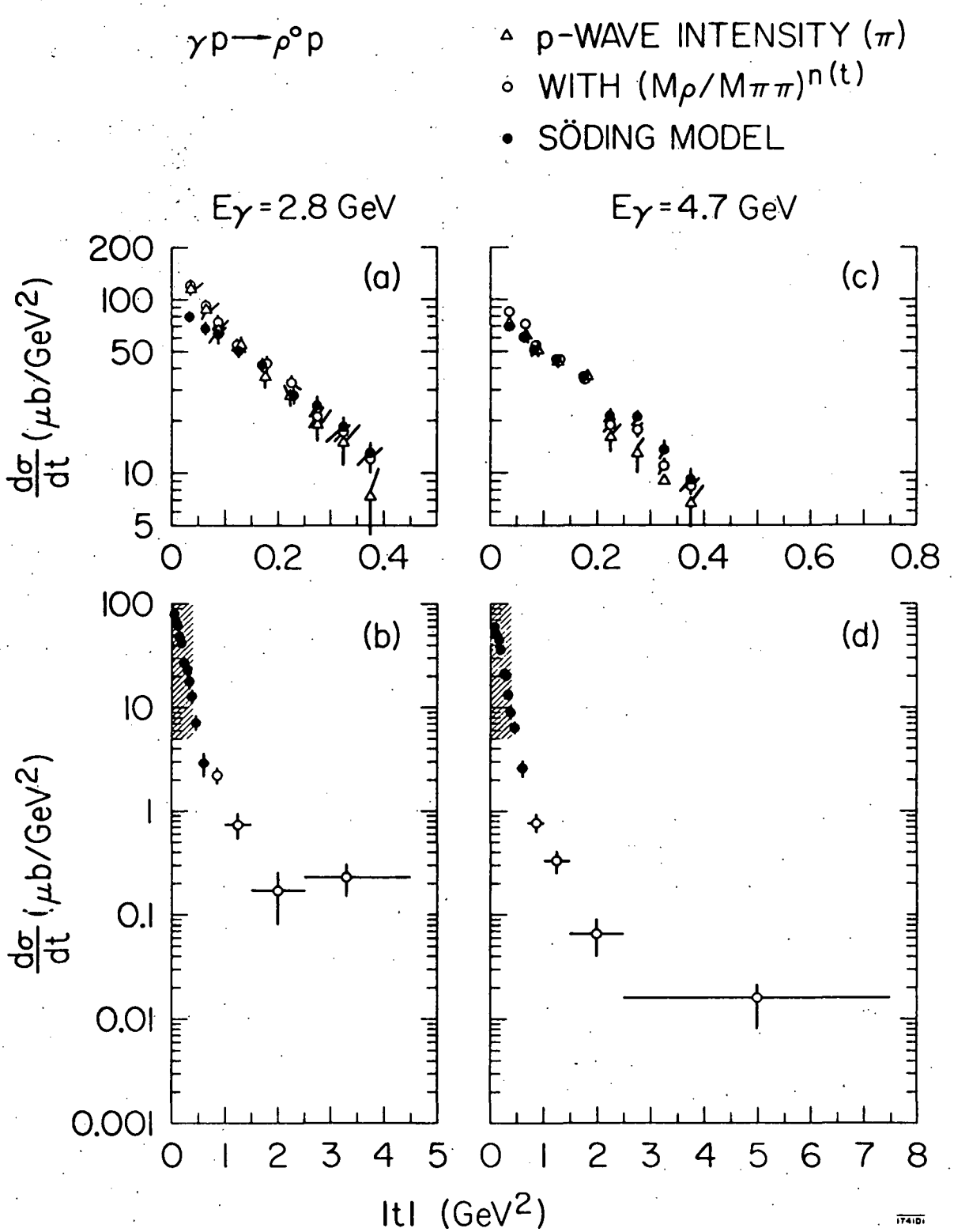
γp→ρ°p
△ p-WAVE INTENSITY (π)
○ WITH (Mρ/Mππ)^n(t)
• SÖDING MODEL
Eγ = 2.8 GeV
Eγ = 4.7 GeV
(a)
(b)
(c)
(d)
dσ/dt (μb/GeV²)
|t| (GeV²)
200
100
50
10
5
1
0.1
0.01
0.001
0
0.2
0.4
0.6
0.8
1
2
3
4
5
6
7
8
17410

2. The Söding Model

We have compared our data with the model of Söding,[11] which explains the ρ^o mass shift in terms of an interference between the ρ^o amplitude (Diag. I of Fig. 15) and a Drell-type background amplitude (Diag. II and III). In adding the Drell background terms to the ρ resonance production amplitude, one stands in danger of "double counting". For example, if one thinks of the ρ as being formed by repeated π exchange then Diag. II, III correspond to just one term in the sum of diagrams corresponding to $\gamma p \rightarrow \rho^o p$ followed by $\rho^o \rightarrow \pi^+\pi^-$.[53] T. Bauer[52] and J. Pumplin[53] avoid double counting by multiplying the Drell term in the p-wave state[54] by $e^{i\delta}\cos\delta$, where δ is the rho phase shift. In terms of a Breit-Wigner form

$$e^{i\delta}\cos\delta = \frac{M_\rho^2 - M^2}{(M_\rho^2 - M^2 - iM_\rho\Gamma)} .$$

The following justification for this factor is an argument of J. Pumplin.[53] In the lab frame the lifetime for forward ρ^o is $\approx E_\gamma/M_\rho \cdot \Gamma$ at high energies, which is long compared to the time associated with production and scattering $2\ E_\gamma/M_\rho^2$. It is therefore natural to treat the ρ as a stable elementary object in considering the dynamics of its production. Pumplin then adds to the Drell terms, a rho resonance production term, and

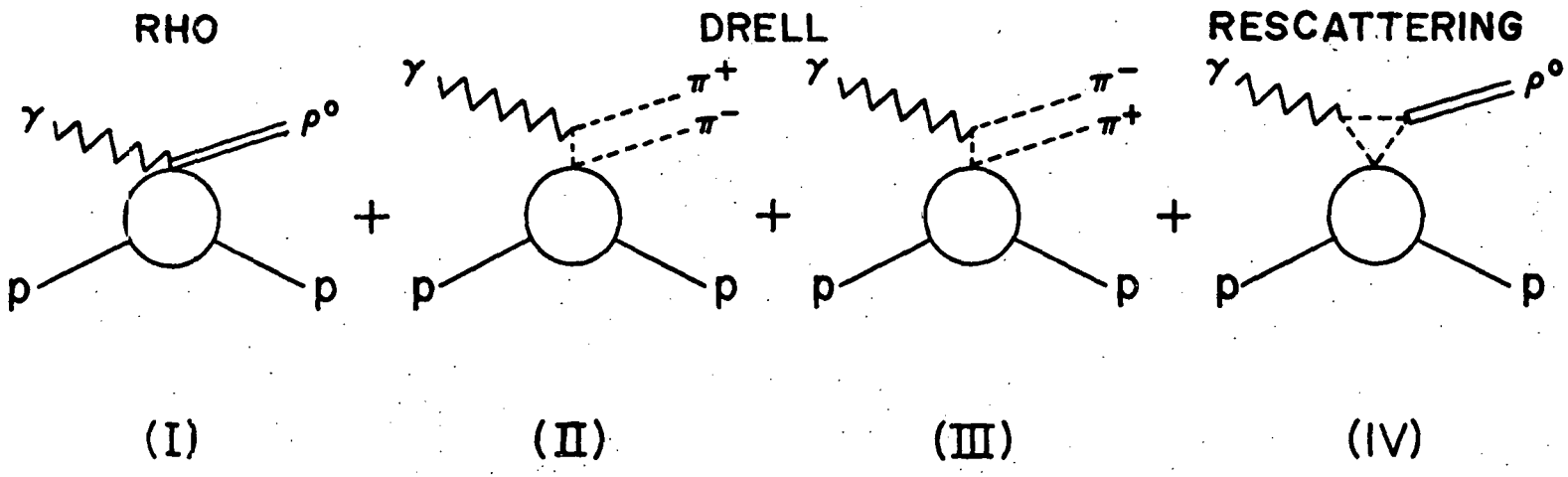

Fig. 15. Diagrams for the reaction $\gamma p \rightarrow \pi^+\pi^- p$ corresponding to the Söding Model. Diagram (IV) is added to account for double counting when adding the rho (Diag. I) and Drell (Diag. II-III) amplitudes.

a rescattering term (Diag. IV of Fig. 15) and shows that adding the absorptive part of the rescattering term (corresponding to the pions which form the ρ being on the mass shell) to the Drell terms is equivalent to multiplying the Drell terms by $e^{i\delta}\cos\delta$.

The results for this experiment for the Söding model without the rescattering correction can be found in reference 1-b.

The predictions of the Söding model have been calculated using a Monte Carlo program written by P. Söding, but modified by us to allow for the Bauer[52] and Pumplin[53] rescattering term and to permit noninterfering constant background and additional $\Delta^{++}(1236)$ amplitudes. A description of the Söding model as used in this experiment can be found in Appendix C.

The lowest three t bins ($0.02 < |t| < 0.4$ GeV^2) were used to determine the rho mass and width appropriate for the Söding model; we find $M_\rho = 778 \pm 3$ (769 ± 3) MeV and $\Gamma_\rho = 146 \pm 10$ (146 ± 10) MeV at 2.8 (4.7) GeV. As shown in Fig. 16 the Söding model (full curves) describes well the $\pi^+\pi^-$ mass distribution. The additional curves of Fig. 16 give the contributions from the rho, Drell, interference (ρ^o and Drell), constant background, and extra $\Delta^{++}(1236)$ terms. From these curves we note the following:

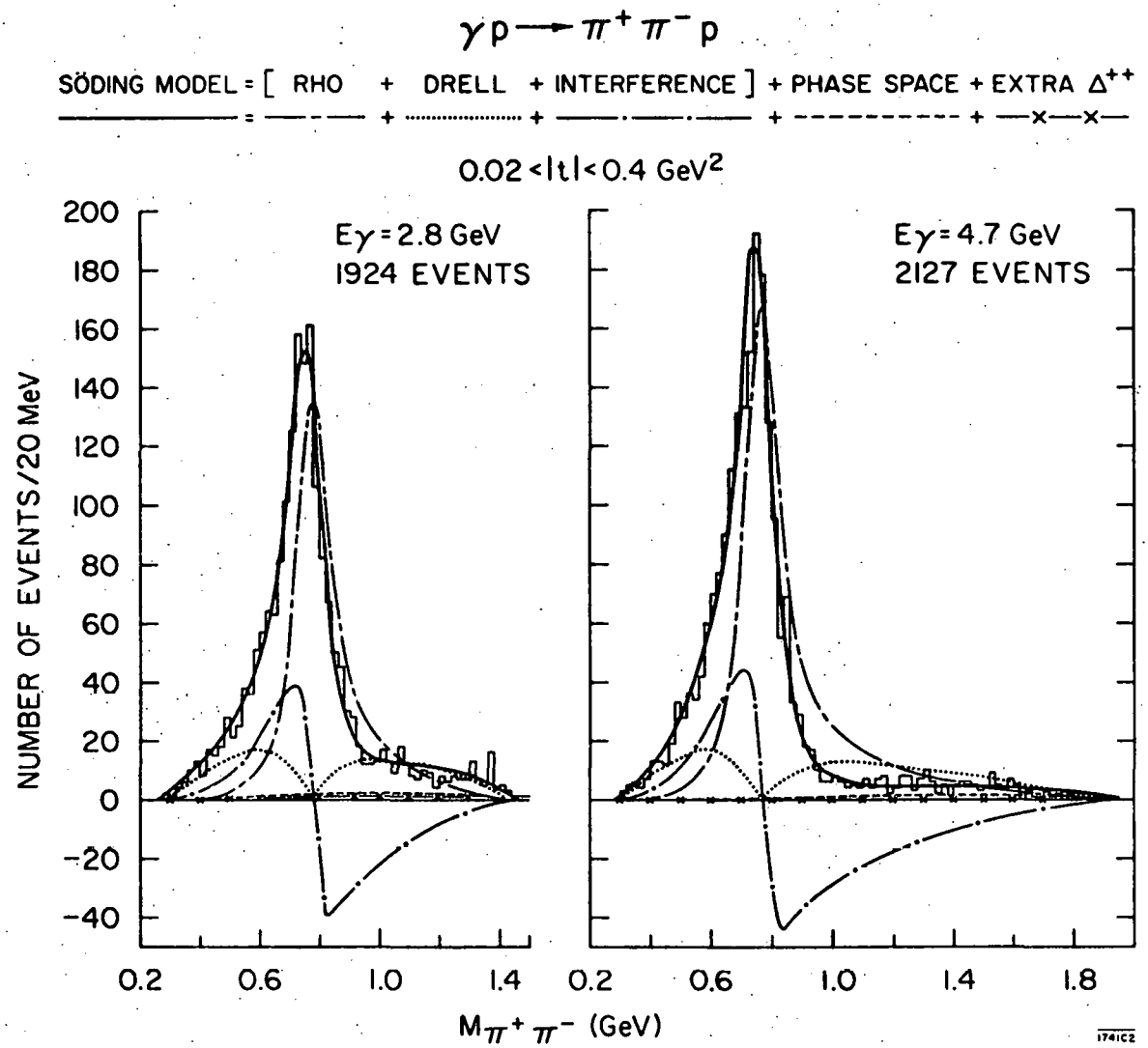

Fig. 16. The $\pi^+\pi^-$ mass distributions for the reaction $\gamma p \rightarrow \pi^+\pi^- p$ (data of Fig. 9). The full curve gives the predictions of the Söding Model; the other curves represent the individual contributions making up the Söding Model.

a) At M_ρ the ρ° production accounts for almost all the $\pi^+\pi^-$ signal.

b) The shape of the $\pi^+\pi^-$ mass distribution is a consequence of the interference term being positive below M_ρ and negative for $M_{\pi\pi} > M_\rho$.

c) The Söding model describes Reaction (1) well as indicated by the small contributions from constant background 5(3.3)% and extra Δ^{++} 2(0.7)% at 2.8(4.7) GeV.

The fitted values of $\sigma_{DRELL}/\sigma_\rho{}^\circ$ are shown in Fig. 17(a) as a function of t. The curves give the t dependence of $\sigma_{DRELL}/\sigma_\rho{}^\circ$ as calculated from the Söding model. The Söding model describes the t dependence of the $\pi^+\pi^-$ mass distributions (solid lines of Fig. 9) and of $\sigma_{DRELL}/\sigma_\rho{}^\circ$, and consequently, the related dependence of the exponential slope of the t distribution on the $\pi^+\pi^-$ mass[4,55] (solid lines of Fig. 12). The shape of the interference pattern observed for Y_4° and other Y_L^M of Fig. 13 is also correctly predicted. The total ρ° production cross sections obtained by fitting the Söding model to our data (and correcting for the interval $|t| < 0.02$ GeV^2) are given in Table VIII.

In Fig. 14 and Table IX we give the differential cross sections obtained from fits with the Söding model. From the differential cross section values for $|t| < 0.4$ GeV^2 we obtain $d\sigma/dt$ $(t = 0)$ and the exponential slope, A, as given in Table

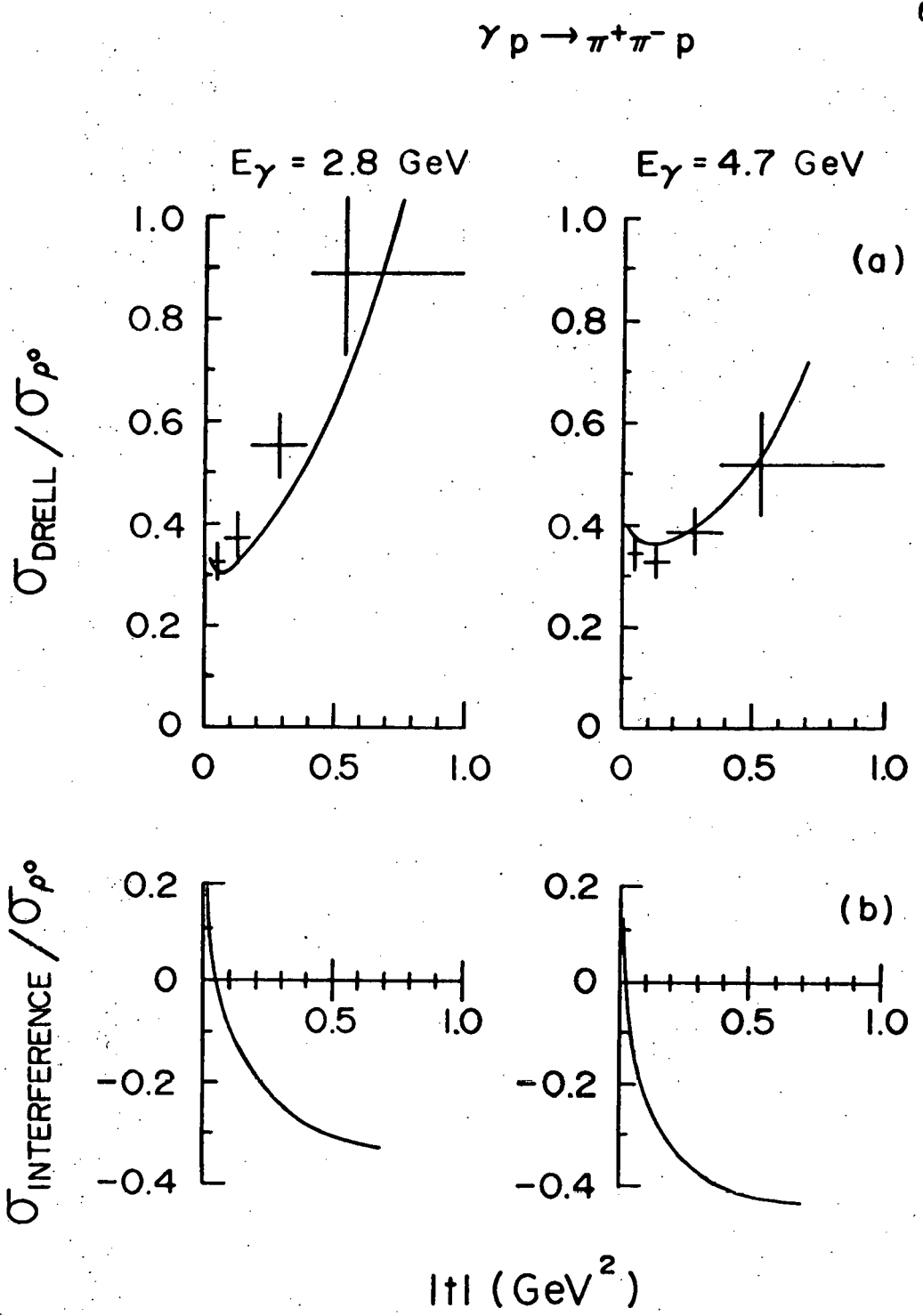

XBL 7010-6687

Fig. 17. (a) Ratio of the fitted Drell to rho cross sections $\sigma_{DRELL}/\sigma_\rho$ as a function of t. The curves show the predictions of the Söding Model. (b) Ratio of $\sigma_{INTERFERENCE}/\sigma_\rho$ as calculated from the Söding Model where $\sigma_{INTERFERENCE}$ is the integral of the interference term over phase space.

VIII. These values are smaller than those for the parameterization $(M_\rho/M_{\pi\pi})^{n(t)}$ or for Π by 25% (17%) at 2.8 (4.7) GeV for the forward differential cross section and ≈ 20% for the slope. The smaller values of the Söding model are a consequence of two effects: 1) the interference term is strongest at small $|t|$ and 2) the integral over the interference term $\sigma_{\text{INTERFERENCE}}$ from $M_{\pi\pi}$ = threshold to $M_{\pi\pi} = M_{MAX}(t)$ decreases and becomes negative with increasing $|t|$. This behavior is seen in Fig. 17(b) where we give the t dependence of $\sigma_{\text{INTERFERENCE}}/\sigma_\rho$ as calculated from the Söding model. Thus the differential cross section for ρ° production will be smaller than the parameterization values which counts almost all the $\pi^+\pi^-$ signal as rho at small momentum transfers. Conversely, at larger momentum transfers the ρ° production as determined by the Söding model may become larger than the parameterization values.

We note that there are theoretical difficulties with the Söding model, namely:

(1) The Söding diagrams are not gauge invariant.

(2) There are uncertainties in the off-mass shell correction.

(3) The resonant ρ° production amplitude is assumed to be purely imaginary.

However, as has been shown the model does explain well Reaction (1) and describes many important features of the data.

3. Comparison with the Vector Dominance Model

The optical theorem can be used to relate the total photoproduction cross section, $\sigma_{TOT}(\gamma p)$, to the forward Compton scattering $d\sigma/dt(\gamma p \rightarrow \gamma_o p)_{t=0}$, which in turn can be related by the vector dominance model to the forward diffractive photoproduction cross sections,[57,58]

$$\sigma_{TOT}(\gamma p) = \sqrt{4\pi\alpha} \sum_V \left[\left(\frac{\gamma_V^2}{4\pi} \right)^{-1} \frac{d\sigma}{dt}(\gamma p \rightarrow V^o p)_{t=0} \right]^{1/2} ,$$

where V^o is a vector meson. In addition to ρ^o we have contributions from ω and ϕ; their contributions are shown in Table X and together contribute less than 20 μb to $\sigma_T(\gamma p)$. Assuming that each of these contributions has the same phase, we can determine $\frac{\gamma_\rho^2}{4\pi}$ from our values for $\sigma_T(\gamma p)$ (see Section III) and $\frac{d\sigma}{dt}(\gamma p \rightarrow \rho^o p)_{t=0}$. Using the forward differential cross section for ρ^o production determined by the Söding model we obtain $\frac{\gamma_\rho^2}{4\pi} = 0.26 \pm 0.04$ at 2.8 and 0.28 ± 0.04 at 4.7 GeV. This should be compared to the value $\frac{\gamma_\rho^2}{4\pi} = 0.52 \pm 0.03$ determined by the Orsay Group.[59] Also in disagreement with the Orsay value is the result for $\gamma_\rho^2/4\pi$ using for the ρ^o forward differential cross section the s-channel c.m. helicity-conserving p-wave $\pi\pi$ contribution, II: $\frac{\gamma_\rho^2}{4\pi} = 0.37 \pm 0.04$ at 2.8 and 0.32 ± 0.04 at 4.7 GeV.

Table X: Vector dominance calculation for ω and ϕ contributions to $\sigma_{TOT}(\gamma p)$ at 2.8 and 4.7 GeV.

V^o	$\frac{\gamma_V^2}{4\pi}$ (a)	E_γ	$\frac{d\sigma}{dt}(\gamma p \to V^o p)_{t=0}$ (b)	Contribution to $\sigma_T(\gamma p)$
		GeV	$\mu b/GeV^2$	μb
ω	3.7 ± 0.7	2.8	13 ± 4	11 ± 2
		4.7	15 ± 4	12 ± 2
ϕ	2.8 ± 0.4	2.8	1.5 ± 0.6	$\pm (4 \pm 1)$
		4.7	2.6 ± 0.5	$\pm (6 \pm 1)$

(a) Ref. 59.

(b) For ω see Ref. 1d (this experiment) and for ϕ see Ref. 4, 60.

C. Conservation of s-Channel Helicity in ρ^o Photoproduction.

We now discuss the ρ decay angular distributions. The analysis uses the formalism of Schilling et al.[2] We present the results in three reference systems which differ in the choice of the spin quantization axis (z-axis) (see Fig. 18): the Gottfried-Jackson system, where the z-axis is chosen as the direction of the incident photon in the ρ^o rest system; the helicity system where the z-axis is opposite to the direction of the outgoing proton in the ρ^o rest system; and the Adair system, where the z-axis is along the direction of the incident photon in the overall c.m. system. The y-axis is always normal to the production plane. For forward-produced ρ^o mesons, all three systems coincide.

We define the following angles (see Fig. 18 and footnote 61): Φ is the angle of the photon electric polarization vector with respect to the production plane and is the same in the total c.m.s. and the ρ^o rest system; θ and ϕ are the polar and azimuthal angles of the π^+ in the ρ^o rest system. The decay angular distribution $W(\cos\theta, \phi, \Phi)$ for rho mesons produced by linearly polarized photons can be expressed in terms of nine independent measurable spin density matrix parameters ρ^{α}_{ik}:[2,62]

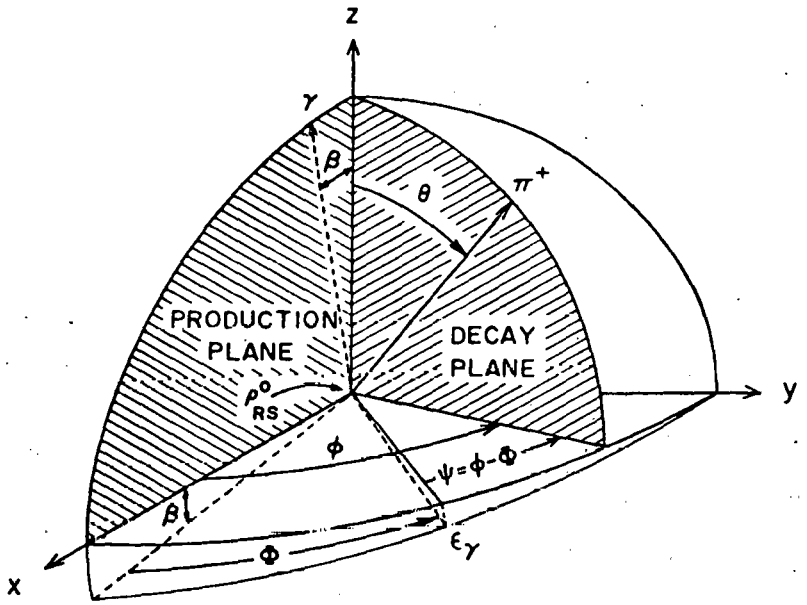

DEFINITION OF QUANTIZATION AXIS (z):

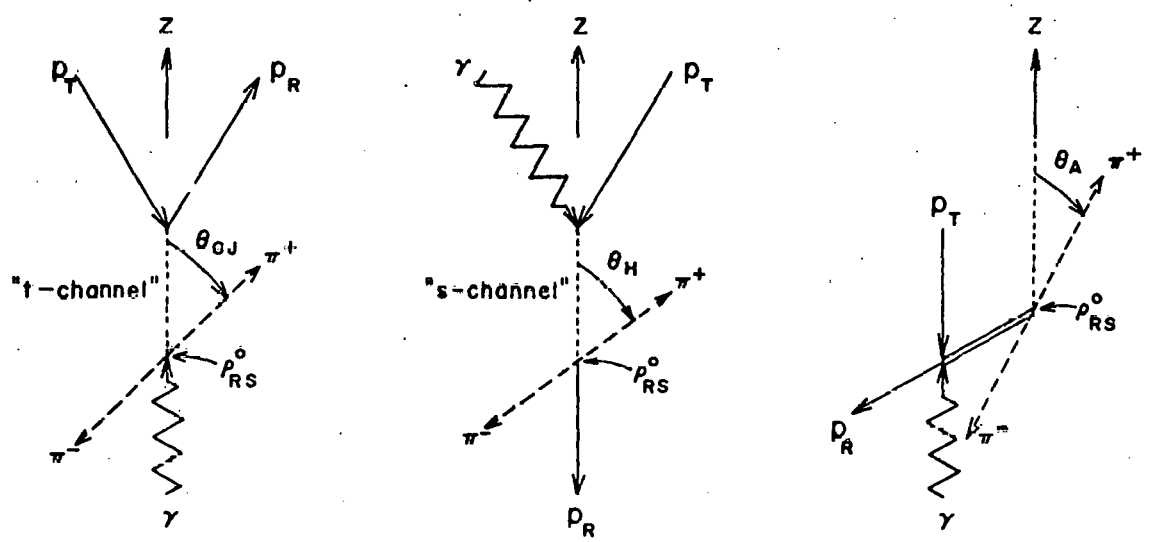

GOTTFRIED-JACKSON HELICITY ADAIR

Fig. 18. Definition of decay angles and quantization axis for the three reference system used to study the ρ^0 decay.

$$W = \frac{3}{4\pi}\left\{\frac{1}{2}\left(1 - \rho^0_{00}\right) + \frac{1}{2}\left(3\rho^0_{00} - 1\right)\cos^2\theta\right.$$

$$- \sqrt{2}\,\mathrm{Re}\,\rho^0_{10}\,\sin 2\theta\,\cos\phi - \rho^0_{1-1}\sin^2\theta\,\cos 2\phi$$

$$- P_\gamma\cos 2\Phi\left[\rho^1_{11}\sin^2\theta + \rho^1_{00}\cos^2\theta\right. \qquad (6)$$

$$\left. - \sqrt{2}\,\mathrm{Re}\,\rho^1_{10}\,\sin 2\theta\,\cos\phi - \rho^1_{1-1}\sin^2\theta\,\cos 2\phi\right]$$

$$- P_\gamma\sin 2\Phi\left[\sqrt{2}\,\mathrm{Im}\,\rho^2_{10}\,\sin 2\theta\,\sin\phi\right.$$

$$\left.\left. + \mathrm{Im}\,\rho^2_{1-1}\,\sin^2\theta\,\sin 2\phi\right]\right\} .$$

Here, P_γ is the degree of linear polarization of the photon, which is calculated from the Compton scattering process to be 93% at 2.8 GeV and 91% at 4.7 GeV (see Section II-D). The matrix elements ρ^0_{ik} describe the rho decay in the case of an unpolarized beam; the additional terms ρ^1_{ik} and ρ^2_{ik} result from the linear polarization of the photon.

Matters are simplified if we use the angle $\psi = \phi - \Phi$ (see Fig. 18) which for forward ρ production, is the angle between the photon-polarization and ρ^0 decay planes. If the rho is transverse and linearly polarized (just as the photon) then it can be shown in the helicity system that

$$\rho^1_{1-1} = \frac{1}{2} , \qquad \text{Im } \rho^2_{1-1} = -\frac{1}{2} , \tag{6.1}$$

all other $\rho^\alpha_{ik} = 0$ in Eq. 6. In this case a little trigonometry shows that

$$W(\cos\theta,\psi) \propto \sin^2\theta \cos^2\psi . \tag{6.2}$$

For a decay distribution of Eq. 6.2 we intuitively define ψ as the azimuthal angle of the decay π^+ with respect to the plane of polarization of the transverse and linearly polarized rho.

Figure 19 shows the distributions of the polar angle θ and the angle ψ in the helicity system for events in the rho mass region with $0.02 < |t| < 0.4$ GeV^2 where t is the square of the four-momentum transfer between incoming and outgoing proton. The $\cos\theta_H$ distributions are proportional to $\sin^2\theta_H$; i.e., the rho mesons are produced in Reaction (1) with c.m.s. helicity ± 1. The ψ distributions are proportional to $(1 + P_\gamma \cos 2\psi_H)$ (this equals $2\cos^2\psi$ for $P_\gamma = 1$) and shows that the rho is almost completely linearly polarized. The density distribution shown in the scatter plot of $\cos\theta_H$ versus ψ_H is proportional to $\sin^2\theta_H \cos^2\psi_H$ and indicates an absence of correlations in $\cos\theta_H$ and ψ_H.

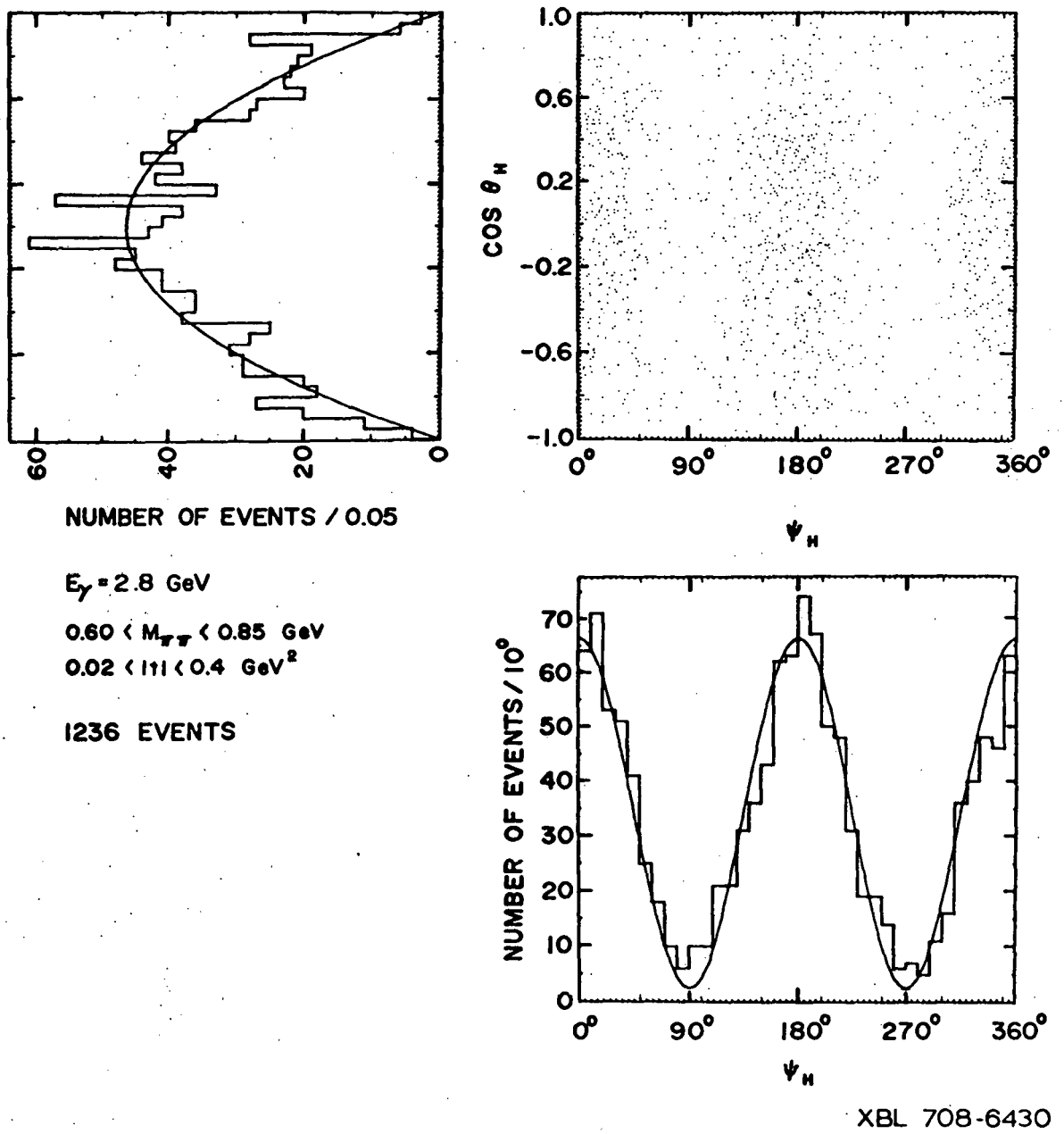

Fig. 19. (a) Reaction $\gamma p \rightarrow \rho^0 p$ at 2.8 GeV: Rho decay angular distributions in the helicity system without background subtraction. The curves are proportional to $\sin^2\theta$ and $(1 + P_\gamma \cos 2\psi)$.

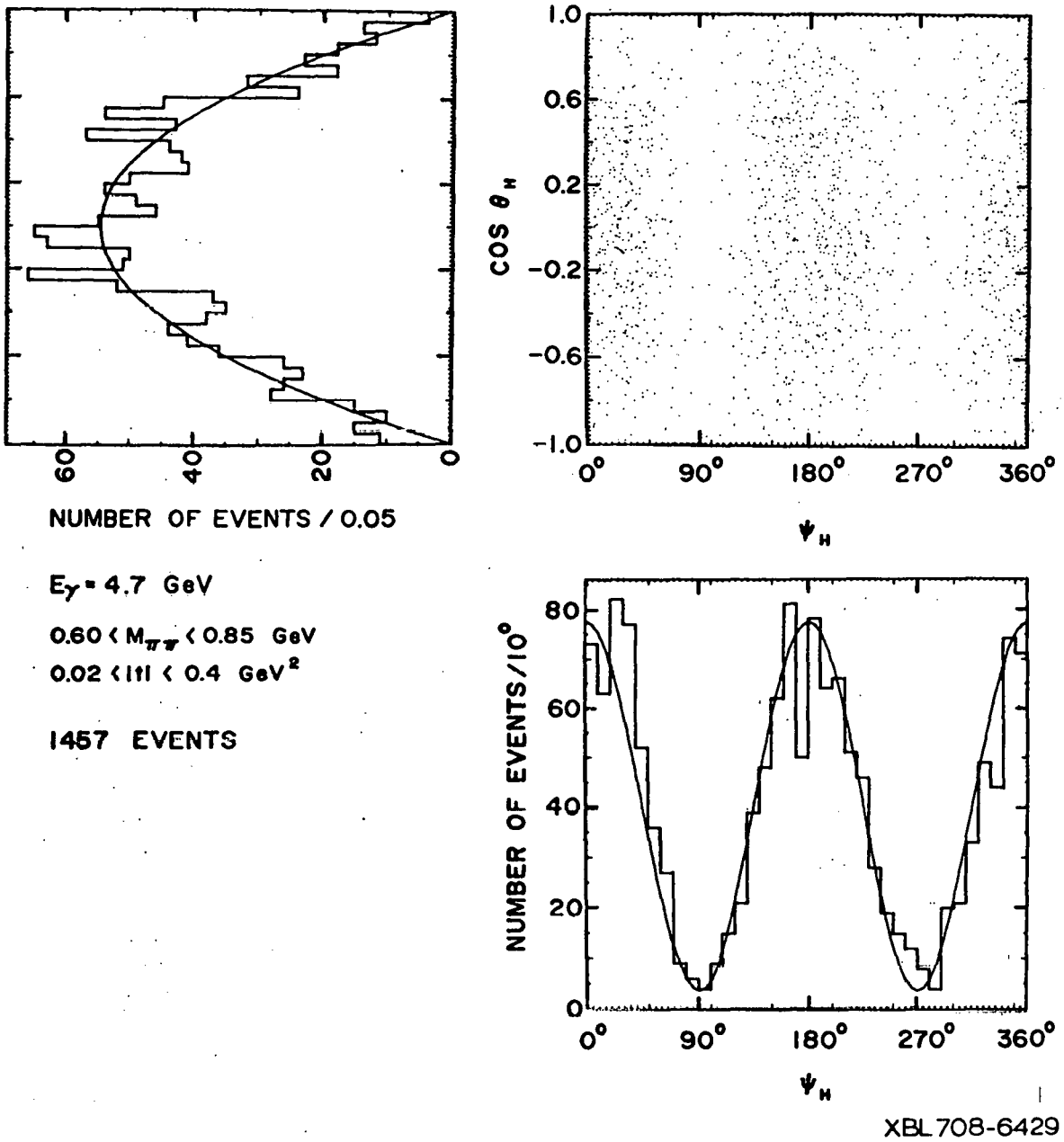

Fig. 19. (b) Reaction $\gamma p \rightarrow \rho^o p$ at 4.7 GeV: Rho decay angular distributions in the helicity system without background subtraction. The curves are proportional to $\sin^2\theta$ and $(1 + P_\gamma \cos 2\psi)$.

The matrices ρ^0_{ik}, ρ^1_{ik} and ρ^2_{ik} can be used to examine the production mechanism; for example, the contributions σ^N, σ^U from natural parity ($P = (-1)^J$) and unnatural parity ($P = -(-1)^J$) exchanges in the t-channel can be obtained with the parameter P_σ, defined by

$$P_\sigma = \frac{\sigma^N - \sigma^U}{\sigma^N + \sigma^U} . \qquad (7)$$

To leading order in energy P_σ is given by[2,78]

$$P_\sigma = 2\,\rho^1_{1-1} - \rho^1_{oo} . \qquad (8)$$

The expression (8) for P_σ is an invariant under rotations around the normal to the production plane.

For the special case of $J^P = 0^+$ (e.g. Pomeron) and $J^P = 0^-$ (e.g. pion) exchanges the relationship of Eq. 8 is easily shown to be valid. We expect for 0^+ exchange and forward ρ^o production that the rho polarization direction will be the same as the incident photon

$$\hat{\epsilon}_\rho = \hat{\epsilon}_\gamma .$$

Then the decay matrix is proportional to

$$M \propto \hat{\pi}^+ \cdot \hat{\epsilon}_\rho = \hat{\pi}^+ \cdot \hat{\epsilon}_\gamma$$

which results in the decay angular distribution

$$W(\cos\theta,\psi) \propto \sin^2\theta \cos^2\psi \ , \qquad (8.1)$$

and we know from Eq. 6.1 and 6.2 that if the flip terms are zero and Im $\rho^2_{1-1} = -\rho^1_{1-1}$ Eq. 8.1 follows for $\rho^1_{1-1} = \frac{1}{2}$. Using Eq. 8 we find that indeed $P_\sigma = +1$ for the natural parity exchange 0^+. However, in order to conserve parity and angular momentum for 0^- exchange, the rho polarization is 90° from the incident photon polarization direction.

$$\hat{\epsilon}_\rho = \hat{\epsilon}_\gamma \times \hat{k}.$$

Then the decay matrix is proportional to

$$M \propto \hat{\pi}^+ \cdot \hat{\epsilon}_\rho = \pi^+ \cdot (\hat{c}_\gamma \times \hat{k})$$

which results in the decay angular distribution

$$W(\cos\theta,\psi) \propto \sin^2\theta \cos^2(90^\circ + \psi) = \sin^2\theta \sin^2\psi \ . \qquad (8.2)$$

In this case we find Eq. 8.2 follows from the general decay distribution of Eq. 6, when the "flip" terms are zero (including ρ^1_{oo}), Im $\rho^2_{1-1} = -\rho^1_{1-1}$, and $\rho^1_{1-1} = -1/2$. Using Eq. 8 we find that indeed $P_\sigma = -1$ for the case of the unnatural parity

exchange 0^-.

We studied the influence of possible background by determining the ρ^{α}_{ik} as a function of the $\pi^+\pi^-$ mass $M_{\pi\pi}$ with the method of moments, using all events in a given $\pi^+\pi^-$ mass interval. Fig. 20 shows the $M_{\pi\pi}$ dependence of ρ^{0}_{00} and ρ^{1}_{1-1} in the helicity system and that of P_σ. There is a pronounced difference between their values inside and outside of the rho region. The values $\rho^{0}_{00} \cong 0.5$ and $P_\sigma \cong 1$ in the rho region are clearly associated with the production of the rho.

We took the background contribution into account by determining the rho density matrix parameters through a maximum likelihood fit including ρ^0, Δ^{++} and flat background contributions using the density distribution of Eq. 2 but replacing $W(\cos\theta_H)$ with $W(\cos\theta,\phi,\Phi)$ of Eq. 6.[63] This method was checked by evaluating the ρ^{α}_{ik} inside and outside of the rho region and interpolating the contribution from the background. Within errors, the same result was obtained. Even if all events in the mass region $0.60 < M_{\pi\pi} < 0.85$ GeV are used without background subtraction the values of the ρ^{α}_{ik} do not change by more than one standard deviation. A further check of the influence of the background on the values of the ρ^{α}_{ik} was made by using the Söding model. We have evaluated the Söding model assuming for the ρ^0 production the values obtained from the maximum likelihood fit for the density matrix parameters. An analysis of the resulting $\pi^+\pi^-$ angular distribution shows that the Drell

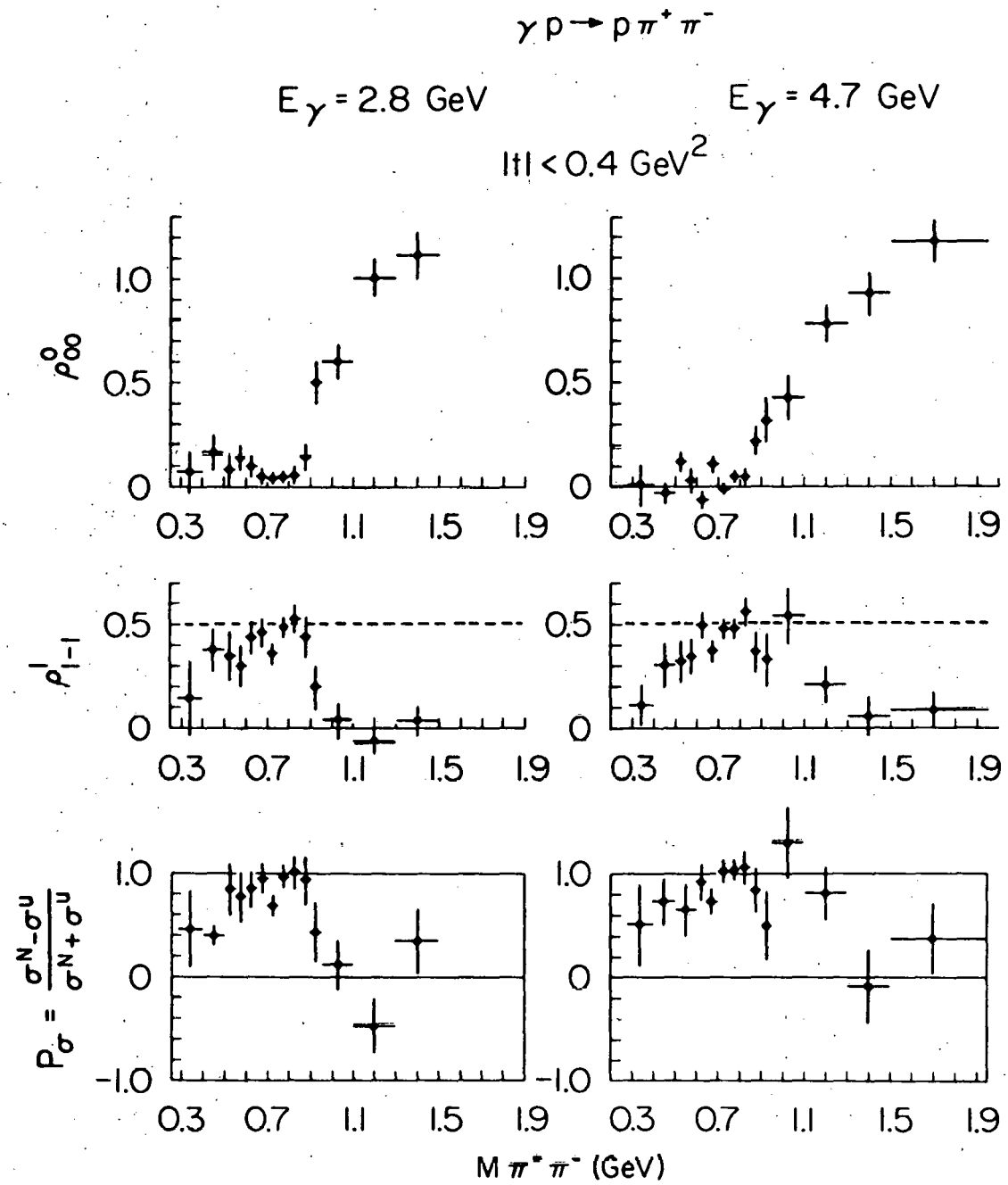

XBL 708-1978

Fig. 20. Reaction $\gamma p \to \pi^+\pi^- p$: The two density matrix elements ρ^0_{00} and ρ^1_{1-1} in the s-channel helicity system, and the parity asymmetry, P_σ, as a function of $M_{\pi\pi}$.

term does not significantly alter the decay angular distribution of the rho. At 4.7 GeV the Drell term is ≈ 90% p-wave and ≈ 10% $J^P = 3^-$. We conclude that the rho density matrix parameters are insensitive to the assumed form of the background.

In Fig. 21 and Table XI P_σ is shown as a function of t. We see that rho production is completely dominated by natural parity exchange up to $|t| = 1$ GeV^2. Averaging P_σ over the range $|t| \leq 1$ GeV^2 we find the contribution from unnatural parity exchange to be 3.1 ± 3.1% at 2.8 GeV and -1.1 ± 2.8% at 4.7 GeV.

In Fig. 22 and Table XI we display the quantity Σ defined as[2]

$$\sum = \frac{\sigma_{\parallel} - \sigma_{\perp}}{\sigma_{\parallel} + \sigma_{\perp}} = \frac{\rho^1_{11} + \rho^1_{1-1}}{\rho^0_{11} + \rho^0_{1-1}} \qquad (9)$$

which has been measured in counter experiments. Here $\sigma_{\parallel}$ and $\sigma_{\perp}$ are the cross sections for the pions from symmetric rho decay ($\theta = \frac{\pi}{2}$, $\phi = \frac{\pi}{2}$)[64] to emerge in the plane of the photon polarization ($\Phi = \frac{\pi}{2}$) or perpendicular to it ($\Phi = 0$). Our values of Σ at 2.8 GeV are in agreement with measurements at 2.4 GeV made by Criegee, et al.[7] and at 3.5 GeV by Diambrini-Palazzi, et al.[8]

Before giving the density matrix parameters, we remark that the ρ^α_{ik}'s can be expressed in terms of bilinear combinations of the helicity or spin amplitudes $T_{\lambda_\rho o \lambda_p', \lambda_\gamma \lambda_p}$ where the λ's denote helicities or spins of the respective particles of the reaction $\gamma p \rightarrow \rho^o p$.[2] For example,

Table XI: P_σ and Σ for the reaction $\gamma p \rightarrow \rho^o p$. Results are plotted in Figs. 21 and 22.

t (GeV)	$P_\sigma = \frac{\sigma^N - \sigma^U}{\sigma^N + \sigma^U}$		$\Sigma = \frac{\sigma_{\parallel} - \sigma_{\perp}}{\sigma_{\parallel} + \sigma_{\perp}}$	
	2.8 GeV	4.7 GeV	2.8 GeV	4.7 GeV
0.02 - 0.05	1.11 ± 0.10	1.18 ± 0.08	0.96 ± 0.10	1.12 ± 0.11
0.05 - 0.08	0.89 ± 0.12	0.79 ± 0.11	0.84 ± 0.15	0.85 ± 0.14
0.08 - 0.12	0.99 ± 0.09	1.09 ± 0.08	0.96 ± 0.13	1.13 ± 0.11
0.12 - 0.18	0.87 ± 0.12	0.97 ± 0.09	0.86 ± 0.19	1.01 ± 0.12
0.18 - 0.25	0.93 ± 0.13	1.07 ± 0.12	1.08 ± 0.26	0.93 ± 0.17
0.25 - 0.40	0.54 ± 0.15	0.92 ± 0.12	0.66 ± 0.17	1.16 ± 0.16
0.4 - 1.0	1.00 ± 0.21	0.92 ± 0.15	1.1 ± 0.4	1.25 ± 0.27

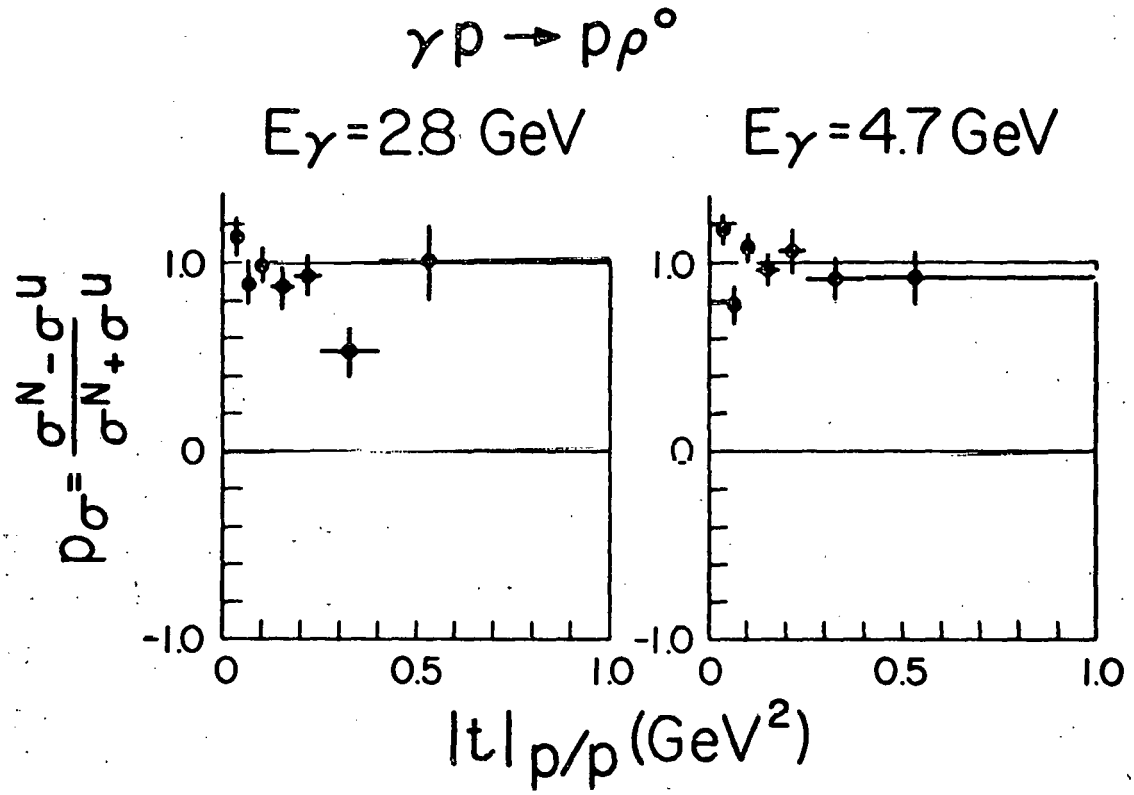

XBL 708-1979

Fig. 21. Reaction $\gamma p \rightarrow \rho^{o} p$: The parity asymmetry P_{σ} as a function of t. P_{σ} is the same in all three systems (Gottfried-Jackson, Helicity, Adair). See data in Table XI.

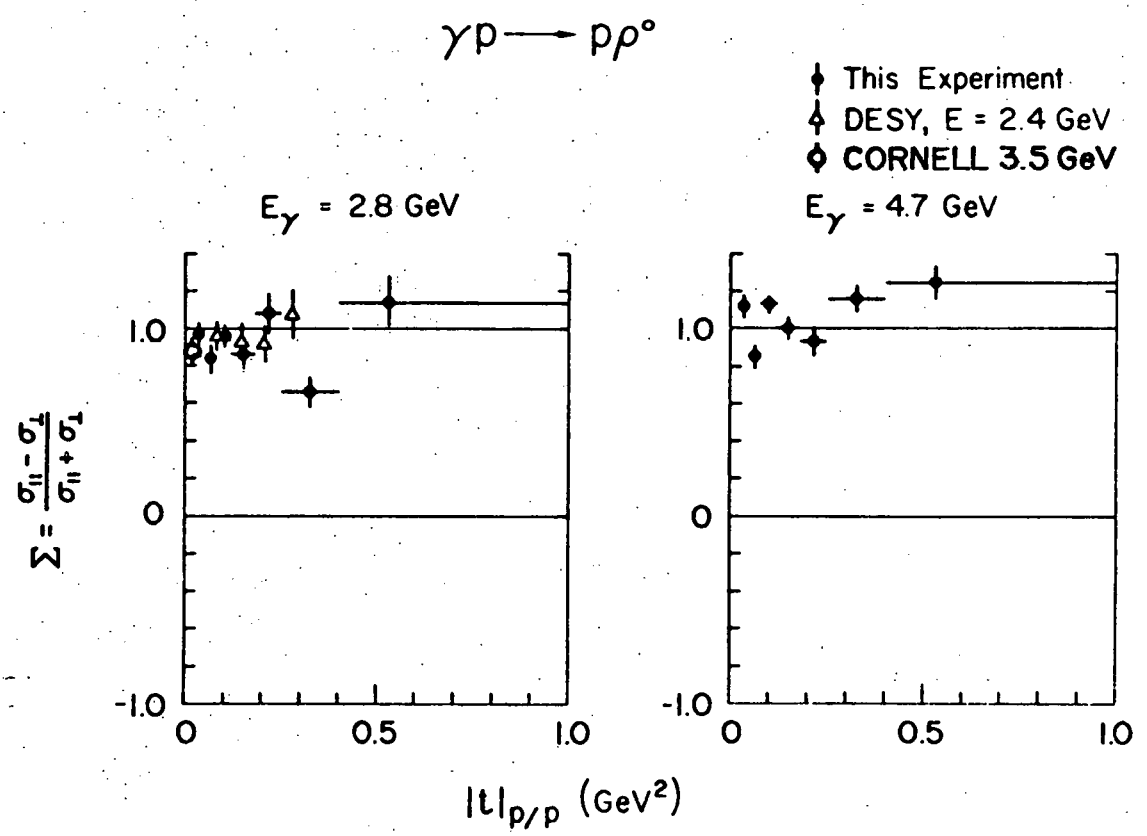

XBL 708-1977

Fig. 22. Reaction $\gamma p \rightarrow \rho^{o} p$: The asymmetry Σ as a function of t. Σ is the same in all three systems (Gottfried-Jackson, Helicity, Adair). See data in Table XI. The DESY and Cornell values are from Ref. 7 and 8, respectively.

$$\rho^{o}_{oo} = \frac{1}{2N} \sum_{\lambda_{p'},\lambda_{p}} \left[|T_{o\lambda_{p'},+1\lambda_{p}}|^2 + |T_{o\lambda_{p'},-1\lambda_{p}}|^2 \right]$$

where N is a normalization factor, receives only contributions from helicity-flip or spin-flip amplitudes. However,

$$\rho^{1}_{1-1} = \frac{1}{2N} \sum_{\lambda_{p'},\lambda_{p}} \left[T_{+1\lambda_{p'},-1\lambda_{p}} T^{*}_{-1\lambda_{p'},+1\lambda_{p}} \right.$$

$$\left. + T_{+1\lambda_{p'},+1\lambda_{p}} T^{*}_{-1\lambda_{p'},-1\lambda_{p}} \right]$$

has contributions from both flip (1st term) and non-flip (2nd term) amplitudes. Of the nine independent measurable spin density matrix parameters of Eq. 6 only ρ^{1}_{1-1} and ρ^{2}_{1-1} receive contributions from helicity (or spin) non-flip amplitudes.

Finally, Fig. 23 and Table XII show the density matrix parameters themselves, evaluated in the Gottfried-Jackson, helicity and Adair systemsas a function of t.

Table XII: **Rho-Density Matrix Elements for the Reaction $\gamma p \rightarrow p\rho^0$.**
Results are plotted in Fig. 23

a) $E_\gamma = 2.8$ GeV, Gottfried-Jackson system

$\lvert t\rvert (GeV^2)$	0.02 - 0.05	0.05 - 0.08	0.08 - 0.12	0.12 - 0.18	0.18 - 0.25	0.25 - 0.40	0.4 - 1.0
ρ^0_{00}	0.079 ± 0.030	0.119 ± 0.035	0.298 ± 0.041	0.431 ± 0.047	0.455 ± 0.051	0.525 ± 0.052	0.476 ± 0.071
$Re\rho^0_{10}$	0.143 ± 0.019	0.195 ± 0.023	0.180 ± 0.020	0.158 ± 0.024	0.146 ± 0.027	-0.002 ± 0.027	-0.089 ± 0.046
ρ^0_{1-1}	0.151 ± 0.037	0.112 ± 0.035	0.111 ± 0.033	0.161 ± 0.035	0.160 ± 0.037	0.267 ± 0.038	0.071 ± 0.057
ρ^1_{00}	-0.140 ± 0.056	-0.057 ± 0.048	-0.231 ± 0.071	-0.328 ± 0.081	-0.390 ± 0.085	-0.359 ± 0.094	-0.483 ± 0.118
ρ^1_{11}	0.091 ± 0.040	0.048 ± 0.045	0.092 ± 0.040	0.114 ± 0.037	0.208 ± 0.042	0.212 ± 0.045	0.134 ± 0.067
$Re\rho^1_{10}$	-0.085 ± 0.035	-0.170 ± 0.033	-0.167 ± 0.029	-0.113 ± 0.037	-0.111 ± 0.042	-0.059 ± 0.042	0.119 ± 0.067
ρ^1_{1-1}	0.505 ± 0.045	0.414 ± 0.055	0.358 ± 0.039	0.270 ± 0.046	0.258 ± 0.047	0.125 ± 0.060	0.246 ± 0.088
$Im\rho^2_{10}$	0.136 ± 0.035	0.249 ± 0.040	0.229 ± 0.032	0.274 ± 0.034	0.259 ± 0.042	0.341 ± 0.033	0.094 ± 0.073
$Im\rho^2_{1-1}$	-0.462 ± 0.036	-0.417 ± 0.053	-0.254 ± 0.058	-0.240 ± 0.054	-0.244 ± 0.058	-0.046 ± 0.040	-0.095 ± 0.091

Table XII (continued) - 2

b) $E_\gamma = 2.8$ GeV, helicity system

$\lvert t\rvert (GeV^2)$	0.02 - 0.05	0.05 - 0.08	0.08 - 0.12	0.12 - 0.18	0.18 - 0.25	0.25 - 0.40	0.4 - 1.0
ρ^0_{00}	-0.045 ± 0.030	-0.034 ± 0.033	0.021 ± 0.029	0.026 ± 0.036	0.016 ± 0.042	-0.071 ± 0.042	0.173 ± 0.064
$Re\rho^0_{10}$	0.013 ± 0.018	-0.032 ± 0.020	0.008 ± 0.023	0.026 ± 0.027	-0.028 ± 0.026	0.112 ± 0.027	0.140 ± 0.043
ρ_{1-1}	0.078 ± 0.037	0.027 ± 0.040	-0.024 ± 0.041	-0.045 ± 0.040	-0.052 ± 0.048	-0.001 ± 0.047	-0.079 ± 0.060
ρ^1_{00}	-0.061 ± 0.056	0.018 ± 0.059	-0.036 ± 0.047	-0.015 ± 0.055	0.041 ± 0.059	0.172 ± 0.063	-0.088 ± 0.108
ρ^1_{11}	0.042 ± 0.046	0.001 ± 0.050	-0.008 ± 0.042	-0.049 ± 0.050	-0.011 ± 0.054	-0.050 ± 0.061	-0.073 ± 0.079
$Re\rho^1_{10}$	0.015 ± 0.030	0.071 ± 0.030	0.026 ± 0.037	-0.009 ± 0.039	0.004 ± 0.037	-0.037 ± 0.042	-0.138 ± 0.062
ρ^1_{1-1}	0.539 ± 0.044	0.453 ± 0.052	0.458 ± 0.043	0.427 ± 0.050	0.484 ± 0.064	0.355 ± 0.062	0.457 ± 0.085
$Im\rho^2_{10}$	-0.050 ± 0.034	0.012 ± 0.040	0.012 ± 0.034	0.016 ± 0.037	-0.073 ± 0.044	0.036 ± 0.031	-0.070 ± 0.064
$Im\rho^2_{1-1}$	-0.496 ± 0.039	-0.551 ± 0.053	-0.427 ± 0.054	-0.445 ± 0.049	-0.424 ± 0.053	-0.465 ± 0.043	-0.157 ± 0.101

Table XII (continued) - 3

c) $E_\gamma = 2.8$ GeV, Adair systems

$\lvert t \rvert (GeV^2)$	0.02 - 0.05	0.05 - 0.08	0.08 - 0.12	0.12 - 0.18	0.18 - 0.25	0.25 - 0.40	0.4 - 1.0
ρ^0_{00}	-0.023 ± 0.029	-0.029 ± 0.033	0.066 ± 0.032	0.114 ± 0.043	0.084 ± 0.040	0.238 ± 0.040	0.512 ± 0.073
$Re\rho^0_{10}$	0.063 ± 0.019	0.060 ± 0.019	0.104 ± 0.022	0.141 ± 0.023	0.129 ± 0.030	0.237 ± 0.030	0.115 ± 0.041
ρ^0_{1-1}	0.088 ± 0.037	0.030 ± 0.040	-0.002 ± 0.039	-0.001 ± 0.039	-0.020 ± 0.045	0.152 ± 0.045	0.091 ± 0.055
ρ^1_{00}	-0.071 ± 0.055	0.039 ± 0.054	-0.052 ± 0.054	-0.084 ± 0.071	-0.054 ± 0.056	-0.027 ± 0.071	-0.442 ± 0.123
ρ^1_{11}	0.048 ± 0.044	-0.009 ± 0.049	0.001 ± 0.042	-0.015 ± 0.049	0.038 ± 0.050	0.051 ± 0.048	0.105 ± 0.066
$Re\rho^1_{10}$	-0.026 ± 0.033	-0.019 ± 0.031	-0.064 ± 0.034	-0.114 ± 0.034	-0.148 ± 0.044	-0.202 ± 0.046	-0.168 ± 0.062
ρ^1_{1-1}	0.531 ± 0.043	0.464 ± 0.053	0.450 ± 0.043	0.392 ± 0.049	0.438 ± 0.059	0.258 ± 0.063	0.276 ± 0.087
$Im\rho^2_{10}$	0.008 ± 0.035	0.096 ± 0.041	0.099 ± 0.032	0.132 ± 0.035	0.063 ± 0.044	0.195 ± 0.035	0.007 ± 0.074
$Im\rho^2_{1-1}$	-0.499 ± 0.038	-0.531 ± 0.051	-0.405 ± 0.056	-0.404 ± 0.051	-0.427 ± 0.058	-0.372 ± 0.035	-0.155 ± 0.086

Table XII (continued) - 4

d) $E_\gamma = 4.7$ GeV, Gottfried-Jackson system

$\lvert t\rvert (GeV^2)$	0.02 - 0.05	0.05 - 0.08	0.08 - 0.12	0.12 - 0.18	0.18 - 0.25	0.25 - 0.40	0.4 - 1.0
ρ^0_{00}	0.143 ± 0.029	0.227 ± 0.036	0.312 ± 0.038	0.357 ± 0.033	0.474 ± 0.047	0.577 ± 0.044	0.476 ± 0.064
$Re\rho^0_{10}$	0.158 ± 0.016	0.234 ± 0.020	0.148 ± 0.021	0.167 ± 0.019	0.114 ± 0.022	0.017 ± 0.027	-0.029 ± 0.036
ρ^0_{1-1}	0.066 ± 0.029	0.082 ± 0.033	0.133 ± 0.032	0.148 ± 0.030	0.229 ± 0.036	0.199 ± 0.026	0.077 ± 0.048
ρ^1_{00}	-0.172 ± 0.041	-0.187 ± 0.054	-0.245 ± 0.060	-0.315 ± 0.056	-0.554 ± 0.063	-0.338 ± 0.085	-0.377 ± 0.095
ρ^1_{11}	0.061 ± 0.037	0.083 ± 0.038	0.119 ± 0.036	0.147 ± 0.031	0.193 ± 0.035	0.195 ± 0.036	0.157 ± 0.048
$Re\rho^1_{10}$	-0.117 ± 0.028	-0.179 ± 0.029	-0.159 ± 0.029	-0.196 ± 0.033	-0.186 ± 0.028	-0.111 ± 0.045	0.064 ± 0.051
ρ^1_{1-1}	0.521 ± 0.037	0.302 ± 0.044	0.416 ± 0.038	0.302 ± 0.037	0.259 ± 0.049	0.273 ± 0.041	0.269 ± 0.059
$Im\rho^2_{10}$	0.152 ± 0.026	0.202 ± 0.029	0.277 ± 0.033	0.301 ± 0.025	0.305 ± 0.036	0.249 ± 0.039	0.256 ± 0.051
$Im\rho^2_{1-1}$	-0.326 ± 0.044	-0.413 ± 0.042	-0.343 ± 0.043	-0.278 ± 0.037	-0.158 ± 0.047	-0.090 ± 0.051	0.164 ± 0.076

Table XII (continued) - 5

e) $E_\gamma = 4.7$ GeV, helicity system

$\lvert t\rvert$(GeV^2)	0.02 - 0.05	0.05 - 0.08	0.08 - 0.12	0.12 - 0.18	0.18 - 0.25	0.25 - 0.40	0.4 - 1.0
ρ^0_{00}	-0.009 ± 0.022	-0.037 ± 0.025	0.027 ± 0.031	0.021 ± 0.029	-0.002 ± 0.035	0.062 ± 0.028	0.208 ± 0.054
$\mathrm{Re}\rho^0_{10}$	0.009 ± 0.018	0.001 ± 0.019	0.010 ± 0.023	-0.024 ± 0.019	0.031 ± 0.023	0.067 ± 0.027	0.043 ± 0.037
ρ^0_{1-1}	-0.001 ± 0.031	-0.064 ± 0.041	-0.003 ± 0.035	-0.031 ± 0.033	-0.006 ± 0.044	-0.052 ± 0.042	-0.048 ± 0.056
ρ^1_{00}	-0.087 ± 0.038	0.052 ± 0.032	-0.051 ± 0.043	-0.001 ± 0.045	0.054 ± 0.045	-0.049 ± 0.057	-0.140 ± 0.078
ρ^1_{11}	0.018 ± 0.039	-0.035 ± 0.041	0.025 ± 0.039	-0.020 ± 0.039	-0.105 ± 0.047	0.048 ± 0.048	0.040 ± 0.055
$\mathrm{Re}\rho^1_{10}$	0.033 ± 0.027	-0.022 ± 0.028	-0.001 ± 0.037	0.008 ± 0.028	-0.007 ± 0.028	0.018 ± 0.046	-0.076 ± 0.053
ρ^1_{1-1}	0.548 ± 0.039	0.420 ± 0.054	0.521 ± 0.036	0.484 ± 0.038	0.563 ± 0.050	0.434 ± 0.051	0.390 ± 0.065
$\mathrm{Im}\rho^2_{10}$	0.014 ± 0.024	-0.023 ± 0.030	-0.002 ± 0.027	-0.028 ± 0.028	0.009 ± 0.031	-0.007 ± 0.039	0.099 ± 0.056
$\mathrm{Im}\rho^2_{1-1}$	-0.388 ± 0.047	-0.475 ± 0.042	-0.508 ± 0.047	-0.510 ± 0.038	-0.470 ± 0.051	-0.344 ± 0.054	-0.366 ± 0.069

Table XII (continued) - 6

f) $E_\gamma = 4.7$ GeV, Adair system

$\lvert t\rvert$ (GeV^2)	0.02 - 0.05	0.05 - 0.08	0.08 - 0.12	0.12 - 0.18	0.18 - 0.25	0.25 - 0.40	0.4 - 1.0
ρ^0_{00}	0.005 ± 0.023	-0.014 ± 0.028	0.059 ± 0.032	0.044 ± 0.030	0.079 ± 0.038	0.207 ± 0.041	0.320 ± 0.056
$\mathrm{Re}\rho^0_{10}$	0.056 ± 0.017	0.078 ± 0.019	0.031 - 0.023	0.074 ± 0.018	0.135 ± 0.023	0.170 ± 0.021	0.092 ± 0.035
ρ^0_{1-1}	0.005 ± 0.031	-0.054 ± 0.040	0.014 ± 0.034	-0.022 ± 0.033	0.036 ± 0.042	0.021 ± 0.040	0.002 ± 0.056
ρ^1_{00}	-0.086 ± 0.038	0.017 ± 0.038	-0.073 ± 0.045	-0.032 ± 0.050	-0.030 ± 0.047	-0.072 ± 0.077	-0.296 ± 0.078
ρ^1_{11}	0.017 ± 0.039	-0.019 ± 0.041	0.035 ± 0.038	-0.003 ± 0.039	0.059 ± 0.045	-0.061 ± 0.047	0.120 ± 0.052
$\mathrm{Re}\rho^1_{10}$	-0.008 ± 0.028	-0.085 ± 0.028	-0.067 ± 0.036	-0.084 ± 0.027	-0.162 ± 0.028	-0.072 ± 0.040	-0.105 ± 0.048
ρ^1_{1-1}	0.550 ± 0.038	0.405 ± 0.053	0.507 ± 0.037	0.466 ± 0.038	0.519 ± 0.050	0.419 ± 0.050	0.306 ± 0.072
$\mathrm{Im}\rho^2_{10}$	0.049 ± 0.024	0.036 ± 0.030	0.078 ± 0.029	0.070 ± 0.027	0.114 ± 0.031	0.091 ± 0.040	0.225 ± 0.056
$\mathrm{Im}\rho^2_{1-1}$	-0.382 ± 0.047	-0.472 ± 0.042	-0.498 ± 0.046	-0.499 ± 0.040	-0.441 ± 0.050	-0.320 ± 0.052	-0.233 ± 0.072

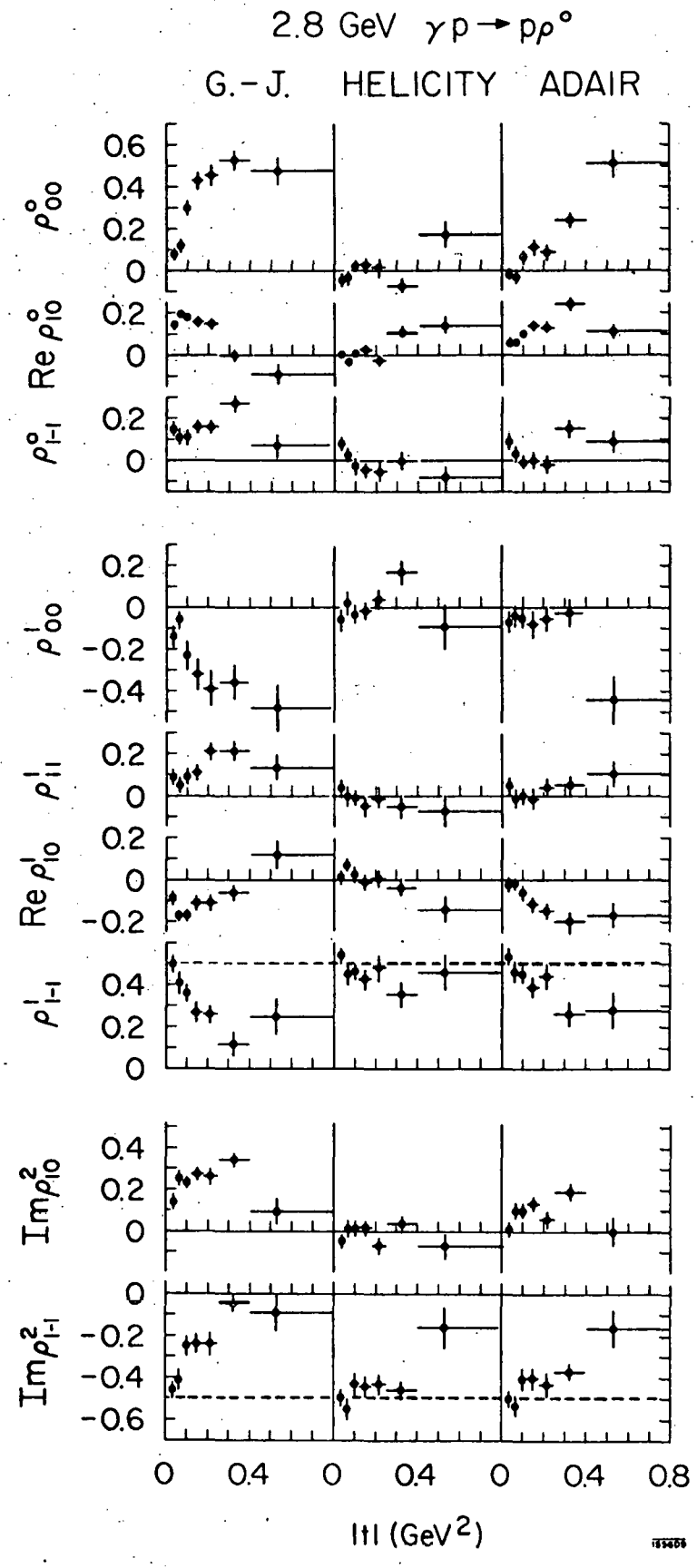

Fig. 23. (a) Reaction $\gamma p \rightarrow \rho^0 p$ at 2.8 GeV: The spin density matrix parameters as a function of t in the Gottfried-Jackson, helicity and Adair systems. Helicity (spin for Adair) conservation requires all $\rho^{\alpha}_{ik}=0$ except those indicated by a dashed line at $\left|\rho^{1,2}_{1-1}\right| = 1/2$, see Eq. 6.1. For numerical values see Table XII.

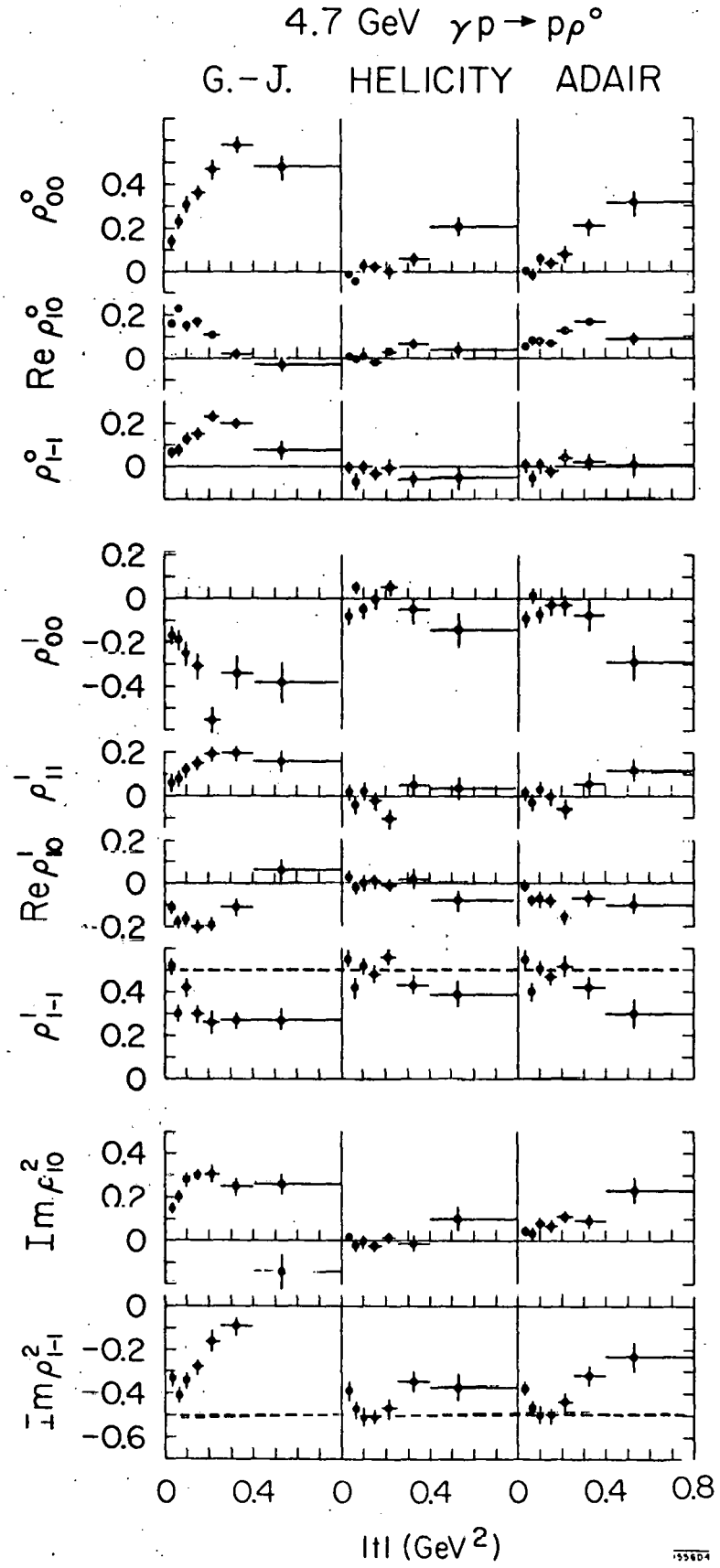

Fig. 23. (b) Reaction $\gamma p \rightarrow \rho^0$ at 4.7 GeV: The spin density matrix parameters as a function of t in the Gottfried-Jackson, helicity and Adair systems. Helicity (spin for Adair) conservation requires all $\rho^{\alpha}_{ik}=0$ except those indicated by a dashed line at $\left|\rho^{1,2}_{1-1}\right| = 1/2$, see Eq. 6.1. For numerical values see Table XII.

We conclude from the behavior of the ρ^{α}_{ik}:

1. The density matrix parameters vary rapidly in the Gottfried-Jackson system.[3,65] The t-channel helicity-flip amplitudes increase rapidly with increasing $|t|$. This behavior rules out t-channel helicity conservation and hence excludes a zero spin particle exchange without absorption as the only contributor to rho production.

2. The ρ^{α}_{ik} in the Adair system also vary significantly with t (see also Fig. 24). This excludes[4] the hypothesis of spin independence in the total c.m. system for rho production.[65]

3. In the helicity system the helicity-flip contributions are zero within errors up to $|t| = 0.4$ GeV^2, i.e., the rho behaves like a photon with the spin aligned along its direction of motion. In other words, the rho production mechanism conserves s-channel c.m.s. helicity. The fact that the flip contributions are minimum in the helicity system is further demonstrated in Fig. 25. The rho density matrix as calculated in the helicity frame was rotated by an angle β around the production normal and a least squares fit made to find that value of β for which flip terms become minimal, that is, we minimized

$$\chi^2(\beta) = \sum_{i,k,\alpha} \left| \frac{\rho^{\alpha}_{ik}(\beta) - \rho^{\alpha}_{ik}\ (\text{photon})}{\Delta\ \rho^{\alpha}_{ik}(\beta)} \right|^2 ,$$

where ρ^{α}_{ik} (photon) is the rho density matrix of the photon (Eq. 6.1). Fig. 25 shows β as a function of the rho c.m.s.

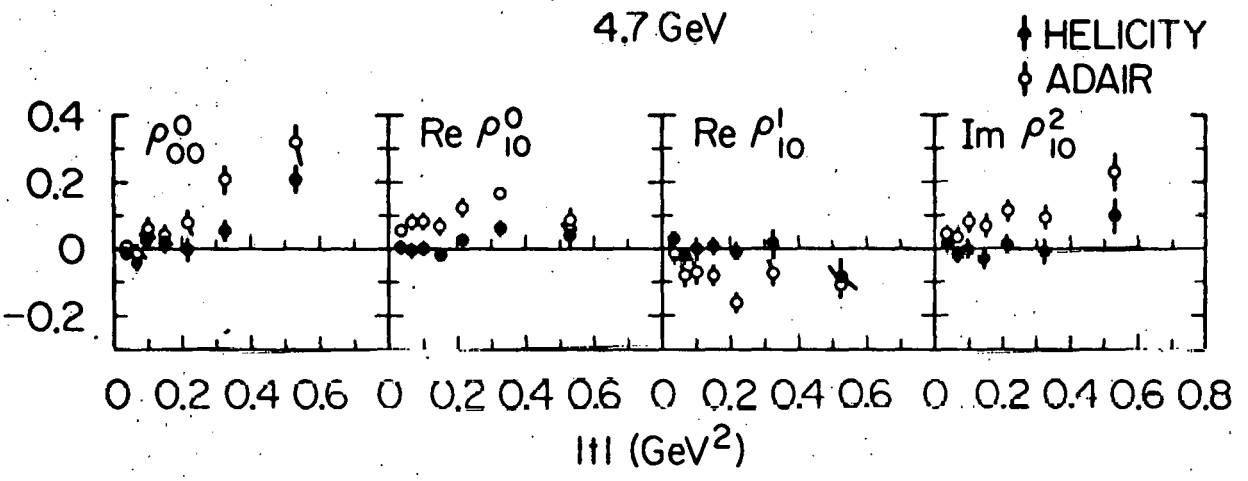

Fig. 24. Reaction $\gamma p \to \rho^0 p$: Comparison of the spin, density matrix parameters ρ^0_{00}, $\mathrm{Re}\rho^0_{10}$, $\mathrm{Re}\rho^1_{10}$, and Im ρ^2_{10} in the helicity ($\blacklozenge$) and Adair ($\lozenge$) system as a function of t (data of Fig. 23). Helicity (spin for Adair) conservation requires all these ρ^α_{ik} to be zero.

production angle θ_{cm} together with lines indicating where the data points should fall if the flip terms are minimal in the Gottfried-Jackson (G.J.), helicity (H), or Adair system (A), respectively. For $\theta_{cm} \lesssim 25^{\circ}$, the helicity system is clearly preferred.

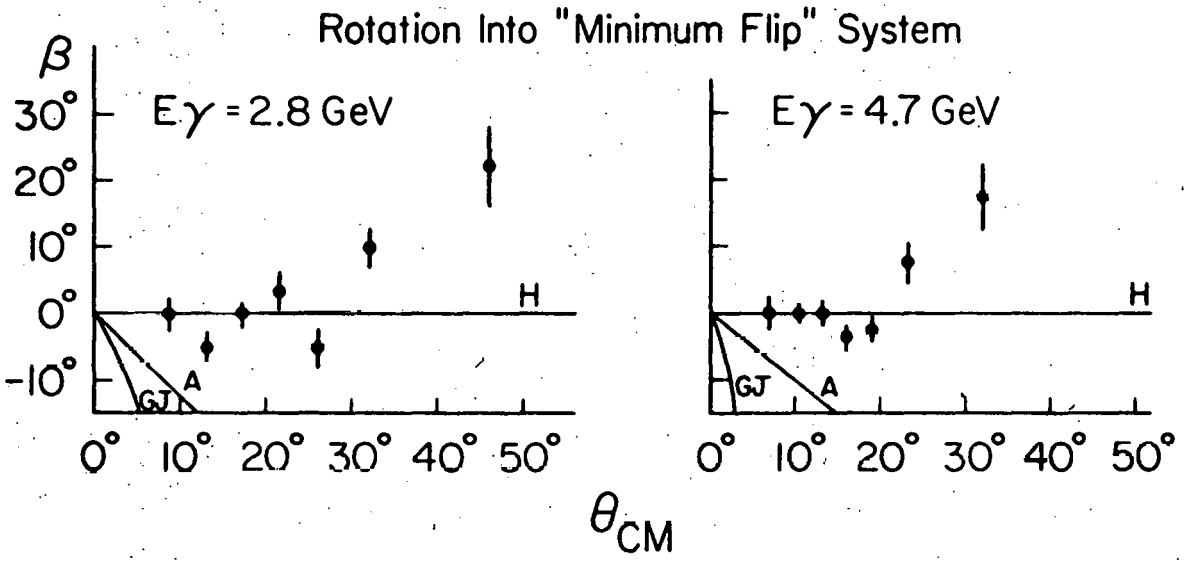

XBL 704-657

Fig. 25. The angle β (measured from the helicity system) for rotation into the "minimum flip" system as a function of the c.m.s. rho production angle θ_{cm}. For the curves labeled GJ, A, and H, see text.

D. OTHER MODELS

The ρ^o mass shift and decay density matrix elements for ρ^o photoproduction have been discussed by others.[50,66-68] In particular, Mannheim and Maor[68] utilize the t-channel kinematics of a two-body reaction and obtain a t dependence of the ρ^o mass shape. However, at t = 0 they have $n(t) = 4$ in the factor $(M_\rho/M_{\pi\pi})^{n(t)}$, in contrast to the data (see Figs.10-11). They do predict s-channel helicity conservation at low $|t|$, but not at large $|t|$ where helicity-flip terms become important. Their predictions about helicity conservation are compatible with this experiment.

The study by Satz-Schilling[50] presents a dual resonance model which, at high energies, describes the whole of Reaction (1). The three-particle final state description includes both resonance and multi-peripheral aspects as well as any "background". Their model describes the $\pi^+\pi^-$ mass distribution and predicts signals for the higher mass vector mesons $\rho'(1250)$ and $\rho''(1550)$ (see Section IV-B). The flattening of the diffraction peak with increasing $M_{\pi\pi}$ is also predicted by this model and is shown at 4.7 GeV in Fig. 12. The behavior of A for $M_{\pi\pi} < 0.9$ GeV describes the data well. However, the increase in A for $M_{\pi\pi} > 0.9$ GeV due to the ρ' is not supported by the data, indicating a weaker ρ' production than predicted by the model.

The model of Kramer and Quinn[67] describes, at high energies, Reaction (1) in the ρ^o-resonance region where the production proceeds by diffraction-dissociation of the photon into a pion pair which interacts strongly in the p-wave state. They also include the effects of initial and final absorptive interactions with the proton. They obtain s-channel helicity conservation for ρ^o production which is dependent on the dipion mass as terms proportional to $M_{\pi\pi}^2 - M_\rho^2$ in the helicity amplitudes become important. For low masses they describe the decrease in the diffractive slope with increasing $M_{\pi\pi}$ and consequently the related t-dependence of the ρ^o mass shift. In constrast to the data near $t = 0$ they predict the Ross-Stodolsky exponent $n(t) = 4$ at $t = 0$.

V. THE ρ^o-ω INTERFERENCE PARAMETERS IN DIFFRACTIVE PHOTOPRODUCTION OF VECTOR MESONS ON HYDROGEN

The discussion below differs from that of Moffeit et al.[1f] only in that some introductory material has been removed.

Clear evidence for ρ^o-ω interference has been observed in photoproduction on carbon by Biggs et al.[20] at Daresbury with 140,000 events, at a mean photon energy of 4.2 GeV. The ρ^o-ω interference is inferred from the shape of the $\pi^+\pi^-$ mass spectrum near M_ω; they obtained constructive interference for $M_{\pi\pi} < M_\omega$ and destructive interference for $M_{\pi\pi} > M_\omega$ in agreement with the prediction of A. Goldhaber, Fox, and Quigg (GFQ).[21] The interference is determined by measuring the relative phase, β, of $\omega \to \pi^+\pi^-$ and $\rho^o \to \pi^+\pi^-$ amplitudes. For photoproduction of ρ^o and ω, the value $\beta = 0$ is predicted assuming the vector dominance model (VDM) and that the photon transforms as the U-spin singlet member of an SU(3) octet. The Daresbury experiment obtained the value $\beta = 2.0 \pm 5.1^o$.

Horn[23] and GFQ[21] have pointed out that the ρ^o-ω phase should be the same in ρ^o and ω production from e^+e^- colliding beams as in diffractive photoproduction (see also Ref. 20, 69). This follows from the observation that the production amplitudes shown in Fig. 26a,b, differ mainly by the presence or absence of a diffractive process, which does not distinguish between ρ^o and ω. For $e^+e^- \to \pi^+\pi^-$ the Orsay storage

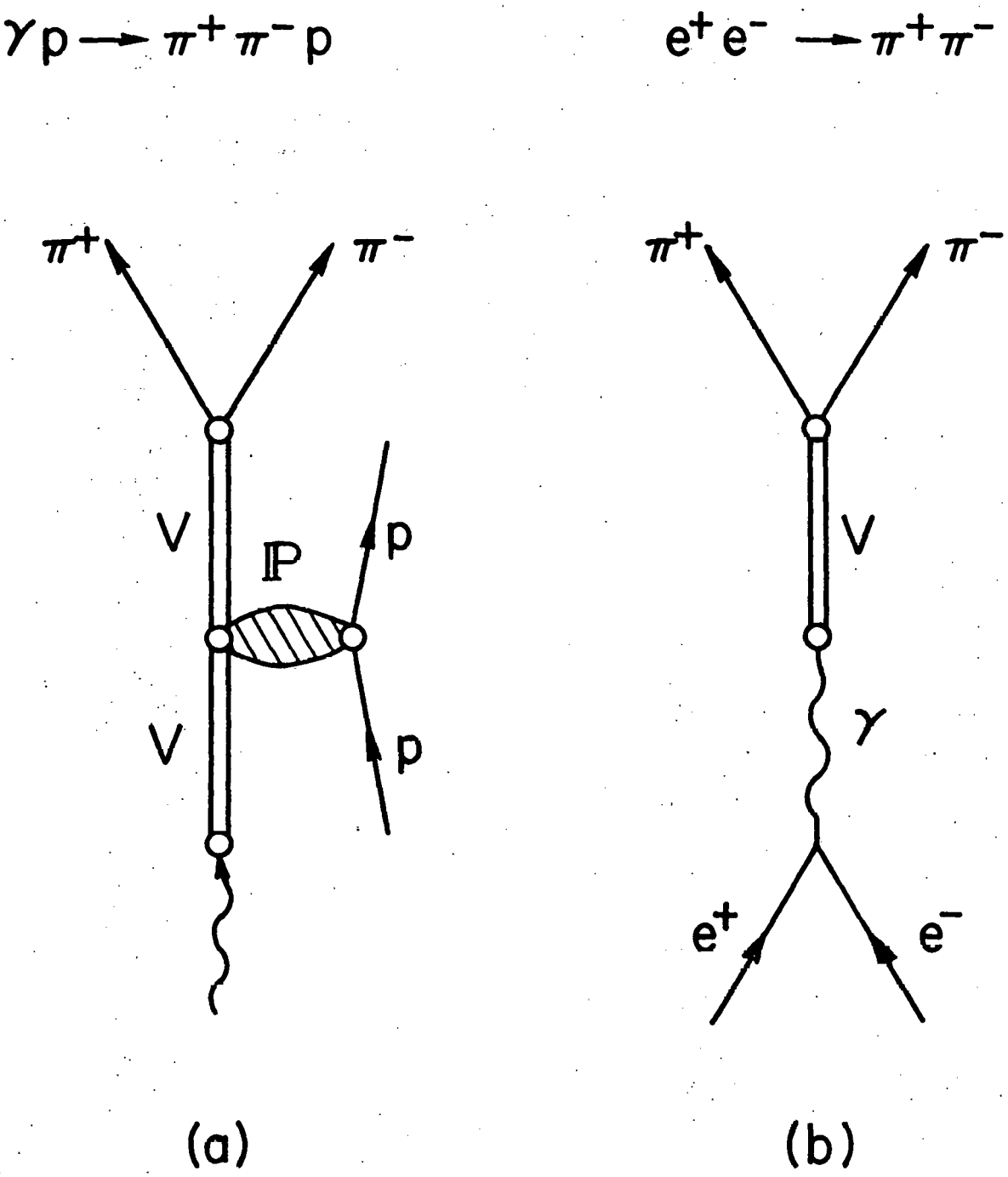

Fig. 26. (a) Production mechanism assumed for $\gamma p \rightarrow \pi^+\pi^- p$.
(b) Feynman diagram for $e^+e^- \rightarrow \pi^+\pi^-$.

ring group[16] reported $\beta = 55 \pm 28^{\circ}$, however, the disagreement with $\beta = 0$ is not statistically compelling.

We have analyzed events of the reaction

$$\gamma p \rightarrow \pi^+\pi^- p \qquad (1)$$

in terms of ρ°-ω interference. For the present study we combined the 2854 events at $E_\gamma = 2.8$ GeV and the 2910 events at $E_\gamma = 4.7$ GeV that fit Reaction (1).

In Fig. 27 we show the $\pi^+\pi^-$ mass distribution for the events of Reaction (1) in the region of the ρ°. We show by the dashed curve the results of a maximum-likelihood fit to the events of Reaction (1) using the density distribution of Eq. 2 to account for ρ°, Δ^{++}, and phase space production. Although the dashed curve accounts for the gross skewing of the ρ° shape, there is an excess of events just below M_ω and a depletion of events just above M_ω.

To analyze our data we chose the mass mixing theory and adopted the notation of GFQ.[21] Here we briefly re-derive their result. The informed reader may skip to Eq. 11.

In the spirit of the vector dominance model we assume that, before mixing, the ρ and ω are produced (by diffraction scattering of the intermediate vector meson) in pure states which conserve G parity, i.e.,

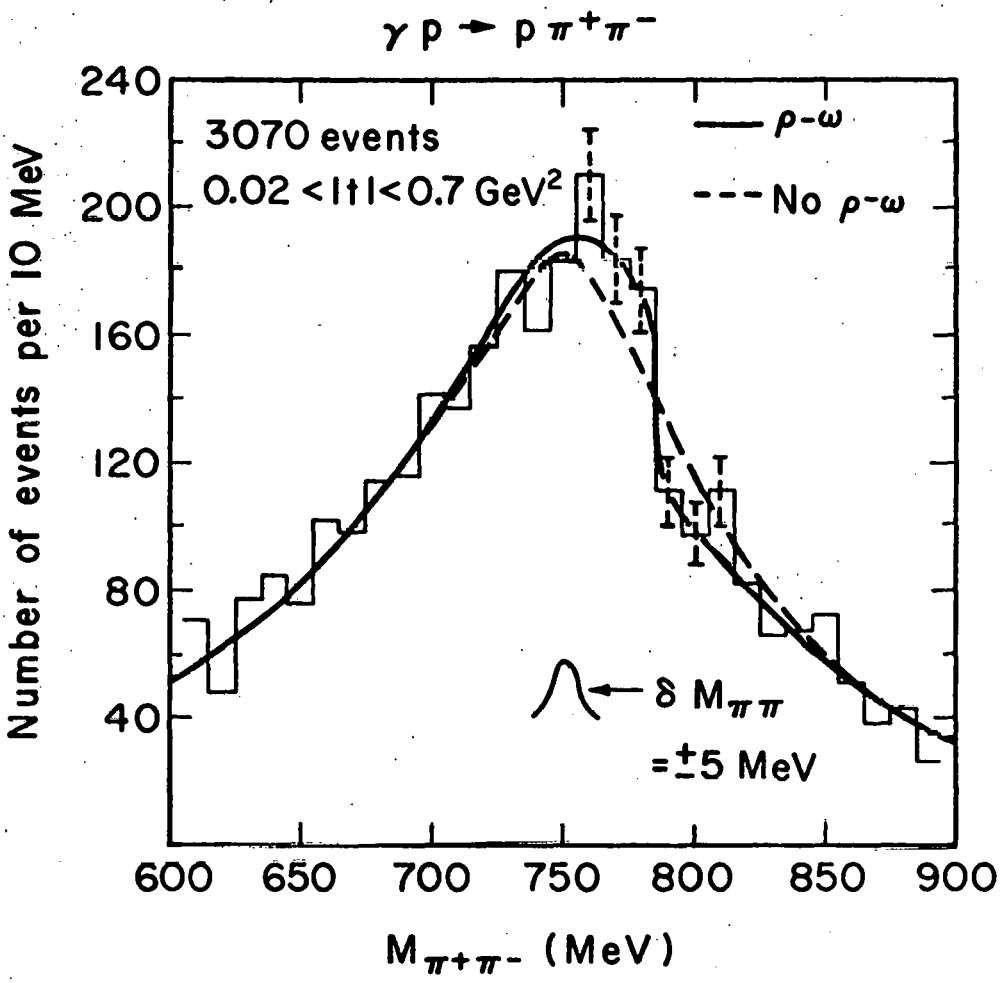

XBL706-3083

Fig. 27. Reaction $\gamma p \rightarrow \pi^+\pi^- p$: $\pi^+\pi^-$ mass distribution for the combined data at 2.8 and 4.7 GeV. The curves give the results of maximum-likelihood fits with (——) and without (----) ρ^o-ω interference.

$$\left.\begin{array}{l} |A_\rho\rangle \rightarrow 2\pi \text{ only} \\ |A_\omega\rangle \rightarrow 3\pi \text{ only} \end{array}\right\} \text{ initial state.}$$

These states are then mixed by the G-violating term δ (assumed to be real[21]) in the propagator matrix P.

Using the usual abbreviation for the Breit-Wigner denominators, $\mu_\rho = m_\rho - m - i\,\Gamma_\rho/2$, μ_ω = similar, and m for the dipion mass, we have

$$P = \begin{vmatrix} \mu_\rho & -\delta \\ -\delta & \mu_\omega \end{vmatrix}^{-1} = \frac{1}{\mu_\rho \mu_\omega - \delta^2} \begin{vmatrix} \mu_\omega & +\delta \\ +\delta & \mu_\rho \end{vmatrix} .$$

Dropping the δ^2 term gives

$$P = \begin{vmatrix} \frac{1}{\mu_\rho} & \frac{\delta}{\mu_\rho \mu_\omega} \\ \frac{\delta}{\mu_\rho \mu_\omega} & \frac{1}{\mu_\omega} \end{vmatrix} .$$

After mixing, the 2π amplitude is

$$S(\pi^+\pi^-) = \Big(T(\rho \to 2\pi),\ T(\omega \to 2\pi) \Big) \Big(P \Big) \begin{pmatrix} A_\rho \\ A_\omega \end{pmatrix} ,$$

where the T' are decay amplitudes in the absence of mass mixing [we take $T(\omega \to 2\pi) = 0$], and the A's are the vector meson production amplitudes,

$$S_{(\pi^+\pi^-)} = \frac{A_\rho \, T_\rho}{(m_\rho - m - i\frac{\Gamma_\rho}{2})} \cdot \left(1 + \frac{A_\omega}{A_\rho} \, e^{i\beta} \, \frac{\delta}{m_\omega - m - i\frac{\Gamma_\omega}{2}} \right) , \quad (10)$$

where $\beta = \text{Arg}\,[A_\omega / A_\rho]$.

That is, in the presence of ρ^{o}-ω interference, the $\pi^{+}\pi^{-}$ mass distribution is given by the ρ line shape (including kinematical dependences), multiplied by a modulating factor, $\mathcal{F}$, which characterizes the interference:

$$\mathcal{F} = \left|1 + \left|\frac{A_\omega}{A_\rho}\right| e^{i\beta} \frac{\delta}{m_\omega - m - i\Gamma_\omega/2}\right|^2 . \qquad (11)$$

On the other hand, the Daresbury group analyzed the ρ-ω interference using the phenomenological parameterization

$$S(\pi^{+}\pi^{-}) \propto \left(\frac{1}{m^2 - m_\rho^{\,2} + i m_\rho \Gamma_\rho} + \frac{\xi\, e^{i\alpha}}{m^2 - m_\omega^{\,2} + i m_\omega \Gamma_\omega}\right) . \qquad (12)$$

Factoring out the ρ Breit-Wigner and comparing Eqs. 12 and 10, one obtains

$$\left|\frac{A_\omega}{A_\rho}\right| e^{i\beta}\, \delta \approx (m_\rho - m - i\frac{\Gamma_\rho}{2})\, \xi\, e^{i\alpha} .$$

Evaluating the right side at the ω mass yields the convenient approximation

$$\left|\frac{A_\omega}{A_\rho}\right| e^{i\beta}\ \delta \approx \frac{\Gamma_\rho}{2}\ \xi\ e^{i(\alpha-\phi_\rho)}\ , \qquad (13)$$

where $\tan \phi_\rho = \dfrac{\Gamma_\rho}{2(m_\rho - m_\omega)}$,

$$\delta \approx \left|\frac{A_\rho}{A_\omega}\right| \frac{\Gamma_\rho}{2}\ \xi \text{ and } \beta = \alpha - \phi_\rho\ .$$

The Daresbury group obtained $\xi = 0.0097 \pm 0.0008$, $M_\rho = 767.7 \pm 1.9$ MeV, $\Gamma_\rho = 146.1 \pm 2.9$ MeV, $M_\omega = 783.2 \pm 1.6$ MeV, $\alpha = 104.0 \pm 5.1$ deg, and $\left|\frac{A_\rho}{A_\omega}\right|^2 = 7.0^{+2.1}_{-1.5}$. These values, along with Eq. 13, give

$$\delta = 1.9 \pm 0.25 \text{ MeV},$$
$$\beta = 2.0 \pm 5.1 \text{ deg}.$$

To investigate ρ^o-ω interference in Reaction (1) we assumed that the density distribution of Eq. 2 adequately represents the kinematical effects in ρ^o production. We then made a maximum-likelihood fit, modulating the ρ^o amplitude of Eq. 2 by the factor $\mathcal{F}$ of Eq. 11. Since β is undefined for $\delta = 0$, we fit the real and imaginary parts of $\exp(i\beta)$.

For convenience we define

$$\tau \equiv 3 \left|\frac{A_\omega}{A_\rho}\right| \delta \ . \qquad (14)$$

The solid line in Fig. 27 gives the best fit obtained with this form, which is better than that obtained without the factor $\mathcal{F}$ by ≈ 2.5 standard deviations. The fit gives

$$\tau \cos\beta = 2.6 \pm 0.9 \text{ MeV},$$
$$\tau \sin\beta = -0.4 \pm 0.9 \text{ MeV},$$

resulting in a value of $\tau = 2.6 \pm 1.0$ MeV. Figure 28 shows contours of equal χ^2 in the $\tau \cos\beta$ and $\tau \sin\beta$ plane, where $\Delta\chi^2 = -2\Delta$ [ln (likelihood)].

In order to relate τ to the ρ^o-ω interference parameter, δ, we must make assumptions concerning the amplitudes A_ω and A_ρ. Figures 29 a-d shows the diagrams for the ρ^o and ω photoproduction amplitudes resulting from natural-parity exchange [$P = (-1)^J$] and unnatural-parity exchanges [$P = (-1)^{J+1}$]. Analysis of the ρ^o decay in this experiment (see Section IV-C) has shown that the reaction $\gamma p \rightarrow \rho^o p$ proceeds almost completely through natural parity exchange; i.e., the amplitude corresponding to Fig. 29c can be neglected. Because the natural- and unnatural-parity exchange amplitudes are orthogonal, only the

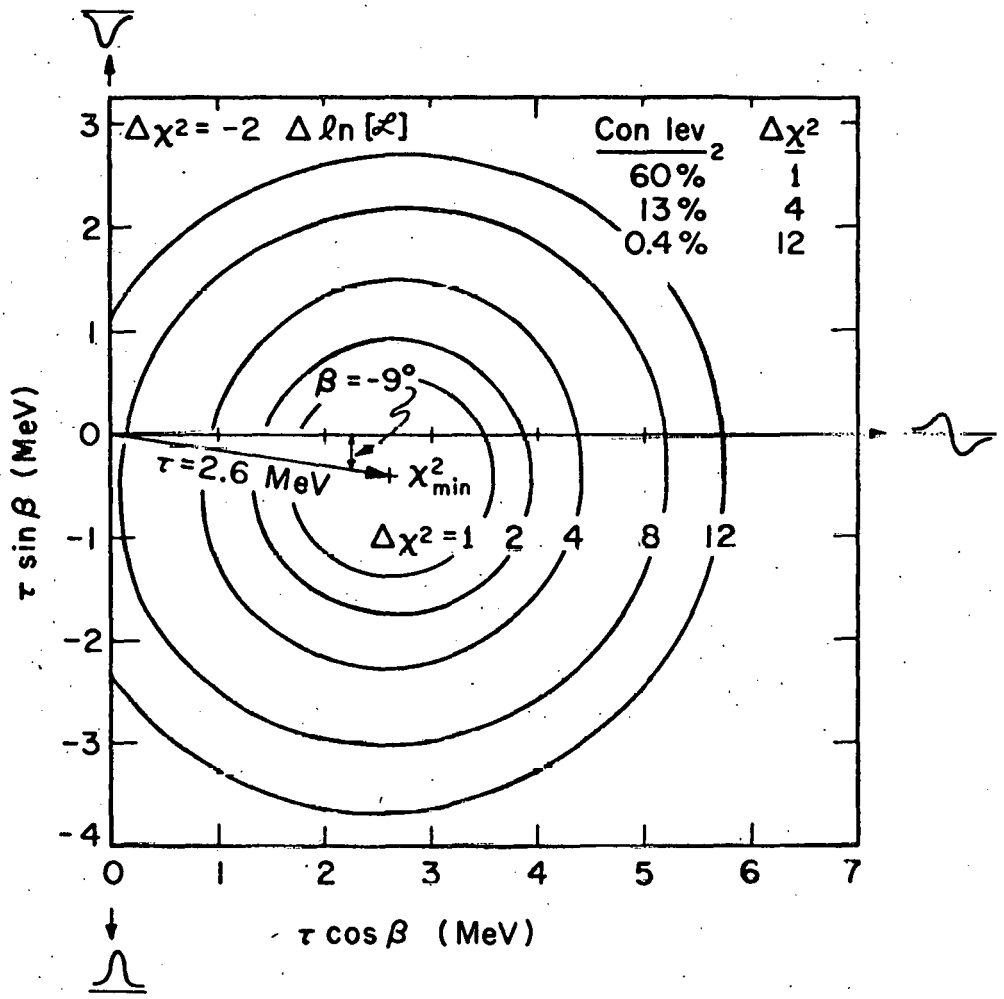

XBL706-3085

Fig. 28. Contours of equal χ^2 in the plane of $\tau \cos\beta$ and $\tau \sin\beta$ ($\tau = 3\left|\frac{A_\omega}{A_\rho}\right| \delta$); δ is the mass mixing parameter, and β is the relative phase of the $\omega \to \pi^+\pi^-$ and $\rho^0 \to \pi^+\pi^-$ amplitude.

natural-parity exchange amplitude for the ω interferes with the ρ^o.

Using VDM and assuming that the ρ and ω elastic scattering amplitudes on protons are equal gives $|A_\omega/A_\rho| = \gamma_\rho/\gamma_\omega$, where γ_V^{-1} is proportional to the photon-vector-meson coupling constant. Augustin et al.,[59] using the Orsay Storage Ring, obtained $\gamma_\omega^2/\gamma_\rho^2 = 7.1 \pm 0.7$.[70] With this value and Eq. 14 our result for τ gives

$$\delta = 2.3 \pm 0.9 \text{ MeV}.$$

In comparing the results for diffractive photoproduction on carbon and on hydrogen, consideration must be given to nuclear effects. An indication of whether coherent nuclear effects are important in the interpretation of the Daresbury experiment can be obtained by comparing their determination[69] of the ratio $\gamma_\omega^2/\gamma_\rho^2$ with the Orsay storage ring results,[59] where nuclear effects are not present. As previously mentioned, the Daresbury group obtained $\gamma_\omega^2/\gamma_\rho^2 = 7.0\ ^{+2.1}_{-1.4}$, whereas the Orsay results are $\gamma_\omega^2/\gamma_\rho^2 = 7.1 \pm 0.7$. Hence, neglecting differences in ρ^o and ω coherent nuclear scattering appears to be justified within errors. If incoherent processes are also ignored, the Daresbury result for the mass-mixing parameter, δ, may be compared with the results from diffractive photoproduction on hydrogen and from colliding e^+e^- beams.[20]

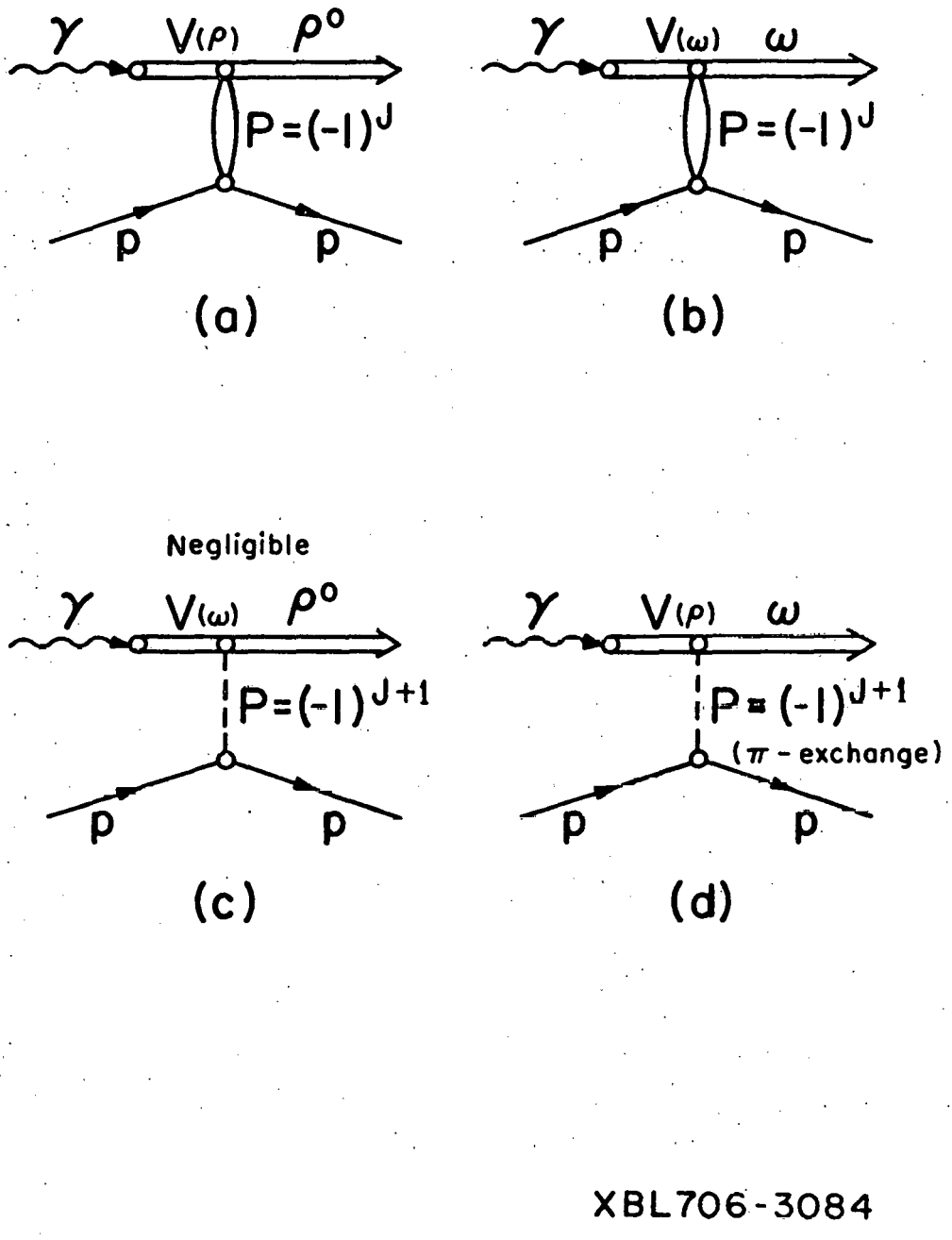

Fig. 29. Production diagrams for ρ^{o} and ω amplitudes resulting from (a,b) natural-parity exchanges, and (c,d) unnatural-parity exchanges.

Given in Table XIII are the values for δ and β. Because our value of δ is about 2.5 standard deviations from $\delta = 0$, we do not give an error for β. The results for δ and β as determined by the colliding-beams experiment and by photoproduction from carbon are given in Table XIII for comparison. Our determination for δ corresponds to $BR[\frac{\omega \rightarrow 2\pi}{\omega \rightarrow all}] = 1.3^{+1.2}_{-0.9}\%$. The parameter δ has been estimated by GFQ from the Coleman-Glashow model[72] to be about 2.5 MeV; this corresponds to $BR[\frac{\omega \rightarrow 2\pi}{\omega \rightarrow all}] = 1.45\%$.

Table XIII: Values of the phase angle (β) and mixing parameter (δ).

Source	β (deg)	δ (MeV)
Theory (Refs. 21, 23)	0	2.5
$e^+e^- \rightarrow \pi^+\pi^-$ (Ref. 16)	55 ± 28	3.5 ± 1.3
$\gamma C \rightarrow \pi^+\pi^- C$ (Ref. 20)	2.0 ± 5.1	1.9 ± 0.25
$\gamma p \rightarrow \pi^+\pi^- p$ [a] (this expt.)	≈ -9	2.3 ± 0.9

[a] No error quoted on β; $\mathrm{Re}(\delta^{i\beta}) = 2.3 \pm 0.9$ MeV and $\mathrm{Imag}(\delta\, e^{i\beta}) = -0.4 \pm 0.9$ MeV.

VI. Δ PRODUCTION IN THE REACTION $\gamma p \rightarrow \pi^+\pi^- p$

In Fig. 30 we show the $\pi^{\pm}p$ mass spectra for Reaction (1). At both energies a clear Δ^{++} signal is found; some Δ^{o} production may also be present. The shaded distributions are for events selected with $|t_\Delta| < 0.4$ GeV^2 (t_Δ is the square of the four momentum transfer between target proton and outgoing $p\pi^+$ system), and $M_{\pi^+\pi^-} > 1.0$ GeV so as to remove most of the ρ^o reflection and to minimize other backgrounds. Corrections for Δ^{++} production due to contamination from wide-angle electron-positron pair production and for scanning losses of Δ^{++} events with short recoil protons (proton momentum < 0.14 GeV/c) were found to be less than 1% (< 4 Δ^{++} events) from a Monte Carlo simulation.[73]

Maximum likelihood fits were made to the Dalitz plot assuming Δ^{++}, Δ^{o}, ρ production, and a constant background. The parameterization of equation 2 was used to describe the ρ^o production. The Söding model (see Section IV), which also fits the $\pi^+\pi^-$ mass distributions well, was not used because the Drell terms in this model already contain contributions to Δ production. In order to state a total Δ cross section, $\sigma(\Delta\pi)$, we must choose a reasonable parameterization of the Δ production amplitude T_Δ. In place of the usual Breit-Wigner forms, e.g., those discussed by Jackson,[51] which describe the Δ shape well near resonance but fail far away,[74] we feel it is more meaningful to use a purely phenomenological form[73] derived

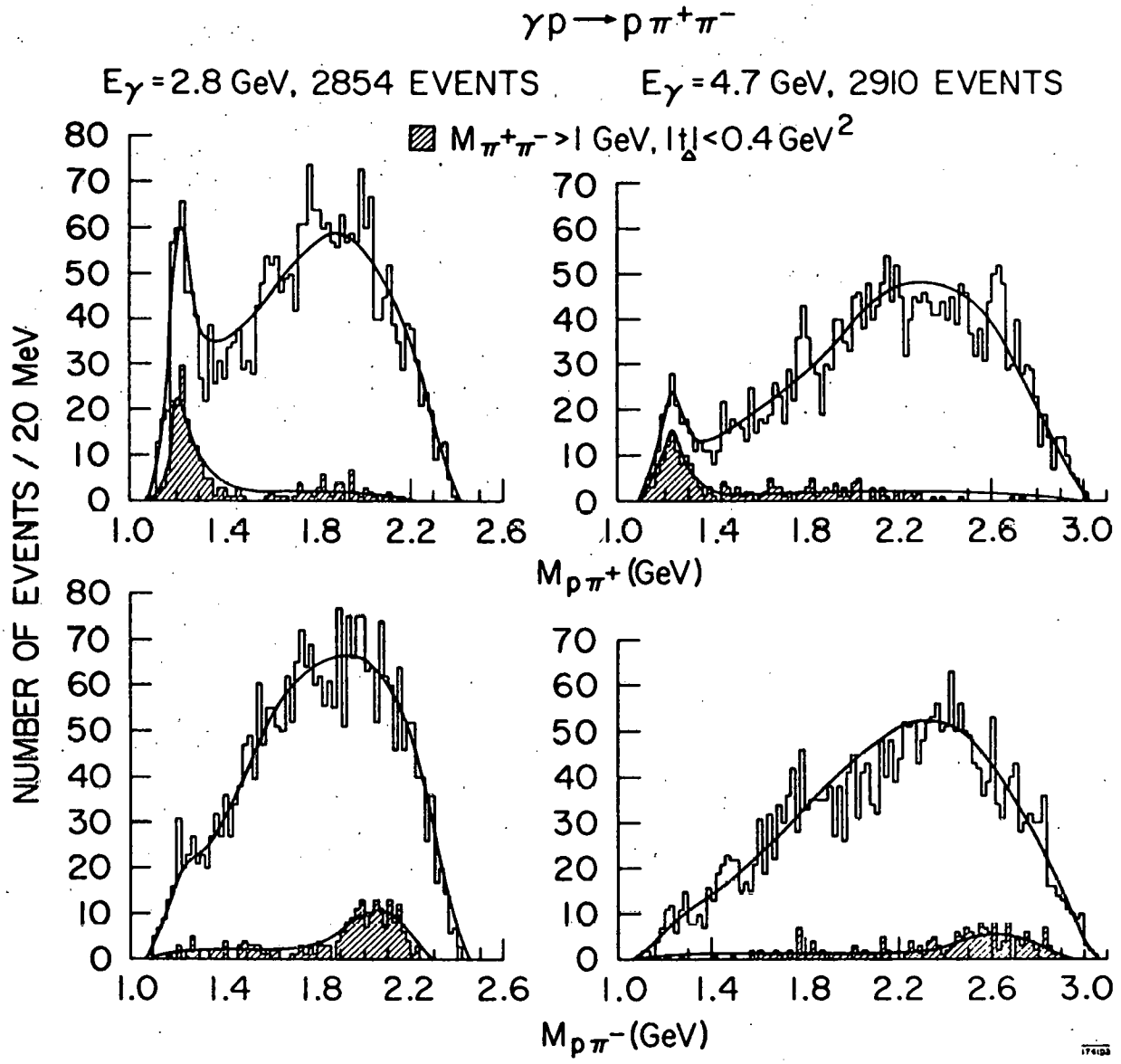

Fig. 30. (a) Reaction $\gamma p \rightarrow \pi^+\pi^- p$: Effective mass distributions for the $p\pi^+$ and $p\pi^-$ systems. The shaded histograms represent events with $|t_\Delta| < 0.4$ GeV^2 and $M_{\pi^+\pi^-} > 1.0$ GeV. The curves are the result of the fitting with Eq. 2, using the experimental phase shifts δ_{33} to describe the Δ shape.

from the experimental phase shifts δ_{33}:

$$|T_\Delta|^2 \propto \frac{\sin^2\delta_{33}}{\Gamma(M)} = \frac{1}{\Gamma(M)} \frac{\left(M_\Delta \Gamma(M)\right)^2}{\left(M_\Delta^2 - M^2\right)^2 + \left(M_\Delta \Gamma(M)\right)^2} \qquad (15)$$

where $\Gamma(M)$ follows from $\tan \delta_{33} = M_\Delta \Gamma(M) / \left(M_\Delta^2 - M^2\right)$ and $M_\Delta = 1.236$ GeV. The values of δ_{33} have been taken from a phase shift analysis.[75] The full curves of Fig. 30 were obtained from the maximum likelihood fit with Eq. 15 describing the Δ signal. If instead the second part of Eq. 15 is used together with a conventional parameterization for $\Gamma(M)$ as was done, e.g., by Boyarski et al.,[28] one finds a value of $\sigma(\Delta\pi)$ larger by $\sim$ 20%. Fig. 30(b) shows by the dotted curved the fit to our data with this same parameterization for $\Gamma(M)$ ($M_\Delta = 1236$ MeV, $\Gamma_o = 120$ MeV). For comparison we have included the full curve of Fig. 30(a) obtained from the δ_{33} phase shifts. Clearly, the phenomenological form derived from the experimental phase shifts is preferred. Furthermore, if we fit M_Δ and Γ_o in the usual Breit-Wigner form using the same parameterization for $\Gamma(M)$ as Boyarski et al.[28] we find $M_\Delta = 1217 \pm 3$ MeV and $\Gamma_o = 72 \pm 8$ MeV in the 2.8 GeV data.

In Table XIV the total cross sections for production of Δ^{++} and Δ^o ($p\pi^-$ decay mode only) are given for the two energies.

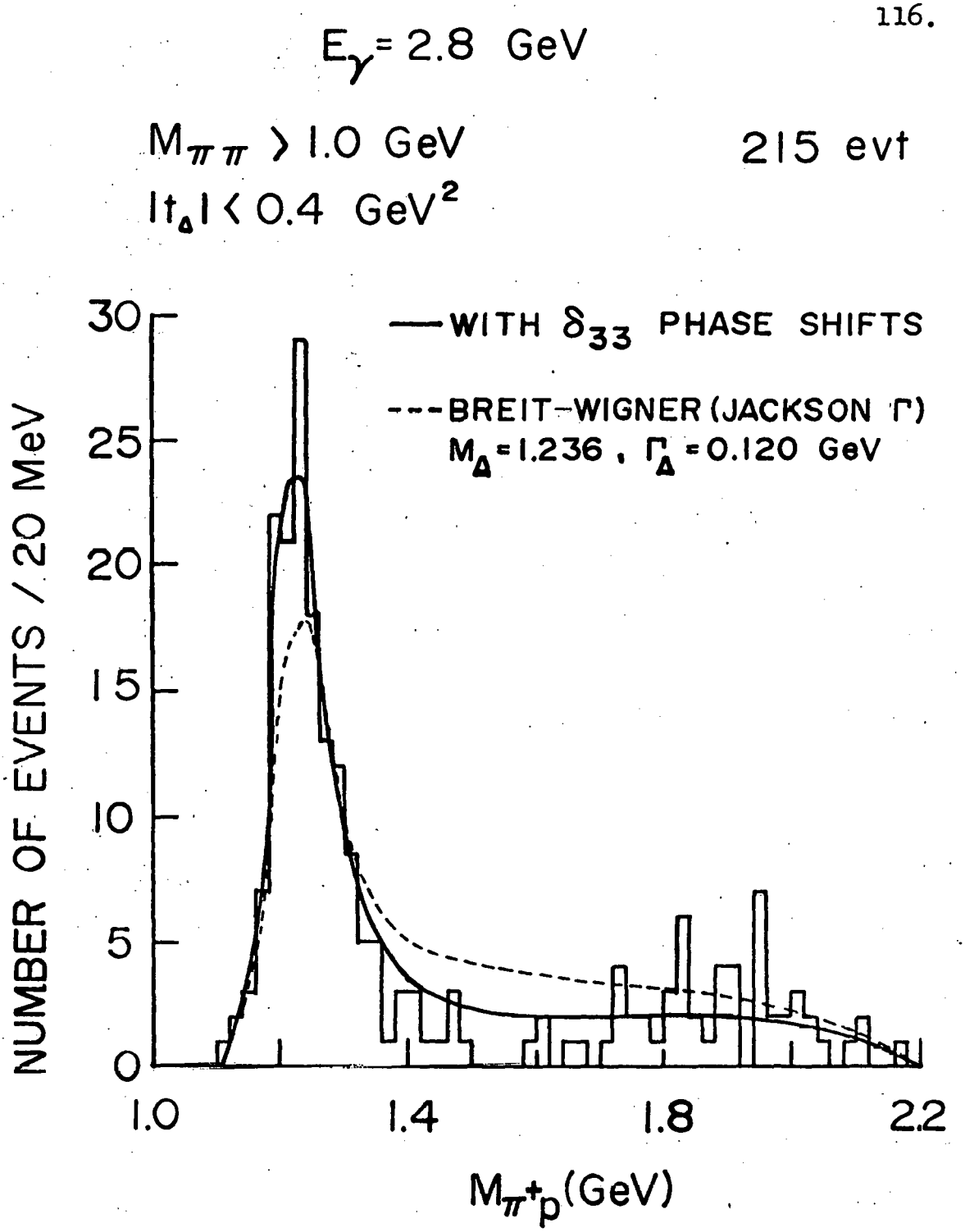

Fig. 30. (b) Reaction $\gamma p \to \pi^+ \pi^- p$: $M_{p\pi^+}$ at 2.8 GeV for events with $|t_\Delta| < 0.4$ GeV^2 and $M_{\pi^+\pi^-} > 1.0$ GeV (shaded area of Fig. 30(a) top-left with expanded scale). The curves give the comparison of the Δ shape with the δ_{33} phase shifts and a Breit-Wigner shape (Eq. 2.2).

Table XIV: Cross Sections for $\gamma p \rightarrow \Delta\pi$ and Parity Asymmetry P_σ for $\gamma p \rightarrow \Delta^{++}\pi^-$.

E_γ (GeV)	$\sigma_{\Delta^{++}\pi^-}$ (μb)	$\sigma_{\Delta^0\pi^+ \hookrightarrow p\pi^-}$ (μb)	P_σ $\lvert t_\Delta \rvert < .5$ GeV^2
2.8	3.6 $\pm$ 0.4	0.5 $\pm$ 0.2	-0.27 $\pm$ 0.12
4.7	1.0 $\pm$ 0.1	0.16 $\pm$ 0.09	-0.53 $\pm$ 0.15

Figure 31 shows the differential cross sections $d\sigma/dt_\Delta$ for Δ^{++} production obtained from the same maximum likelihood fit (using Eq. 15) as described above for each t-interval separately. Also shown are the measurements of Boyarski et al.[28] at $E_\gamma = 5.0$ GeV. Measurements in the backward direction have been made by Anderson et al.[76]

The Δ^{++} angular distributions have been analyzed in terms of the Δ spin density matrix in the (Δ^{++}) Gottfried-Jackson frame. The z axis is taken as the direction of the incident proton in the Δ rest frame; the y axis is defined as the normal to the production plane ($\hat{y} \propto \hat{\gamma} \times \hat{\pi}^-$). The electric vector $\underline{\epsilon}$ of the photon makes an angle Φ with the production plane: $\cos\Phi = \hat{\gamma}\cdot(\hat{\epsilon}\times\hat{y})$, $\sin\Phi = \hat{y}\cdot\hat{\epsilon}$. The decay angles θ and ϕ are the polar and azimuthal angles of the outgoing proton in the Δ rest system: $\cos\theta = \hat{p}\cdot\hat{z}$, $\cos\phi = \hat{y}\cdot(\hat{z}\times\hat{p})/|\hat{z}\times\hat{p}|$, $\sin\phi = -(\hat{y}\times\hat{z})\cdot(\hat{z}\times\hat{p})/|\hat{z}\times\hat{p}|$. The decay angular distribution $W(\cos\theta,\phi,\Phi)$ is then given by:[77]

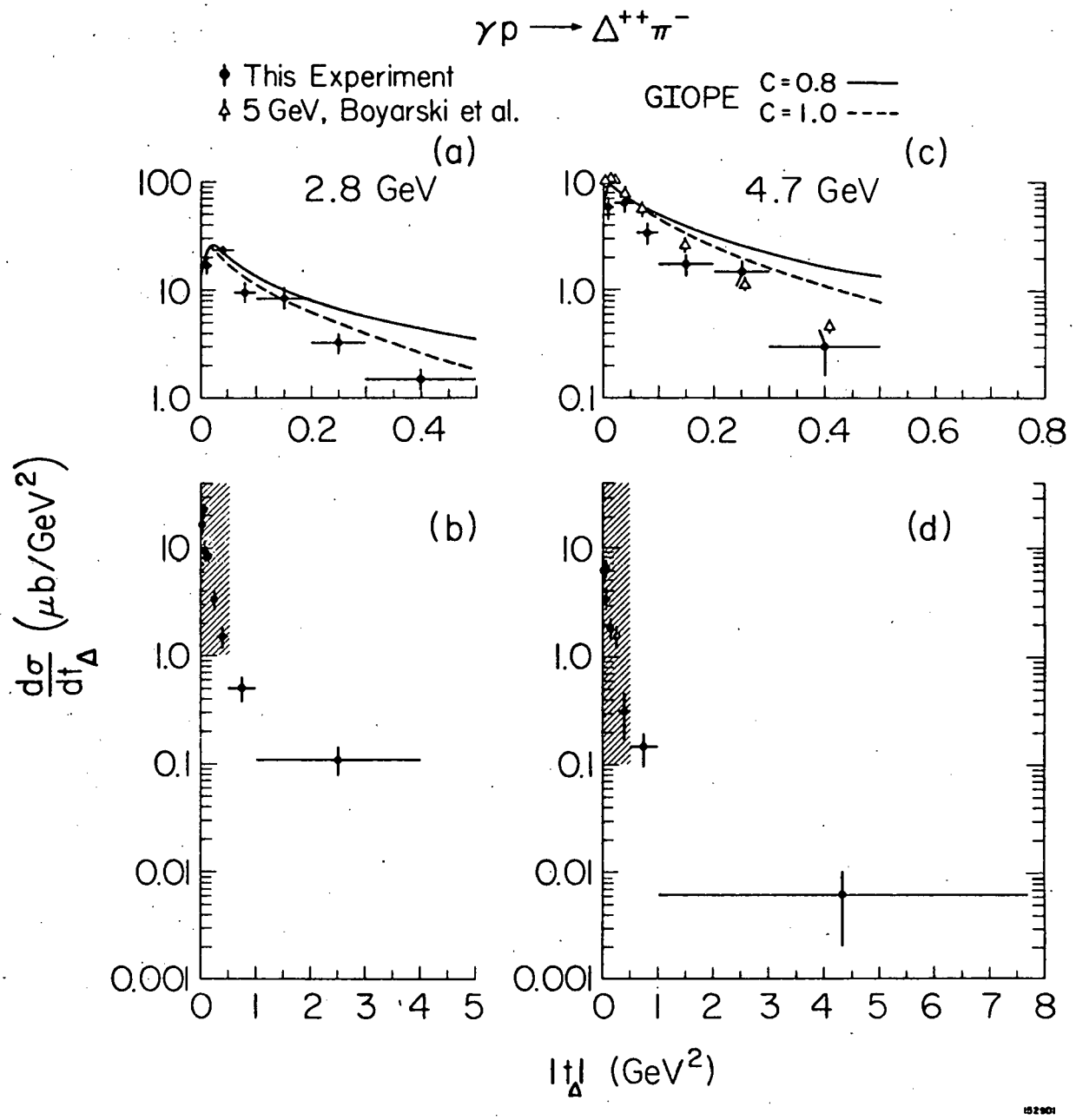

Fig. 31. Reaction $\gamma p \rightarrow \Delta^{++}\pi^-$. Differential cross sections $d\sigma/dt_\Delta$ from this experiment (♦) and from Ref. 28 for E_γ = 5 GeV (△). The shaded regions in (b), (d) are shown on an expanded scale in (a), (c). The curves are the predictions of the gauge-invariant OPE model with absorption corrections for C = 0.8 (—) and C = 1 (----).

$$W = \frac{3}{4\pi}\left\{\rho^0_{33}\sin^2\theta + \left(1/2-\rho^0_{33}\right)\left(1/3+\cos^2\theta\right)\right.$$

$$- 2/\sqrt{3}\ \mathrm{Re}\ \rho^0_{31}\cos\phi\ \sin 2\theta - 2/\sqrt{3}\ \mathrm{Re}\ \rho^0_{3-1}\cos 2\phi\ \sin^2\theta$$

$$- P_\gamma \cos 2\Phi\left[\rho^1_{33}\sin^2\theta + \rho^1_{11}\left(1/3+\cos^2\theta\right)\right.$$

$$\left. - 2/\sqrt{3}\ \mathrm{Re}\ \rho^1_{31}\cos\phi\ \sin 2\theta - 2/\sqrt{3}\ \mathrm{Re}\ \rho^1_{3-1}\cos 2\phi\ \sin^2\theta\right]$$

$$- P_\gamma \sin 2\Phi\left[2/\sqrt{3}\ \mathrm{Im}\ \rho^2_{31}\sin\phi\ \sin 2\theta\right.$$

$$\left.\left. + 2/\sqrt{3}\ \mathrm{Im}\ \rho^2_{3-1}\sin 2\phi\ \sin^2\theta\right]\right\} \qquad (16)$$

where P_γ is the degree of linear polarization; P_γ = 93% at 2.8 GeV and P_γ = 91% at 4.7 GeV. We define the polarization asymmetry $\sum$ by

$$\sum = \frac{1}{P_\gamma}\frac{W(\Phi=0) - W(\Phi=\pi/2)}{W(\Phi=0) + W(\Phi=\pi/2)} \qquad (17.1)$$

where $W(\Phi)$ is the Φ distribution integrated over θ and ϕ. Performing the integration of Eq. 16 and evaluating $W(\Phi)$ at $\Phi = 0, \pi/2$ we find

$$\sum = -2\left(\rho^1_{33} + \rho^1_{11}\right). \tag{17.2}$$

A related quantity is the parity asymmetry, P_σ, defined in terms of the cross sections for natural and unnatural parity exchange in the t-channel, σ^N and σ^U:

$$P_\sigma = \frac{\sigma^N - \sigma^U}{\sigma^N + \sigma^U}. \tag{18}$$

At high energies $P_\sigma = 2\left(\rho^1_{33} + \rho^1_{11}\right)$,[78] and the polarization asymmetry Σ which is easily measured by counter techniques becomes the negative of the parity asymmetry.

To obtain the nine measurable density matrix parameters, events were selected with $M_{p\pi^+} < 1.32$ GeV and the method of moments was used with the Eberhard-Pripstein procedure[79] to remove the ρ^o reflection: only events with $\cos\theta_H < 0.3$ (0.7) at 2.8 GeV (4.7 GeV) were used, where θ_H is the angle in the c.m.s. of the Δ between the decay proton and the Δ line of flight in the total c.m.s. Fig. 32 shows the ρ^α_{ik} and P_σ obtained this way. The values of P_σ averaged over $|t_\Delta| < 0.5$

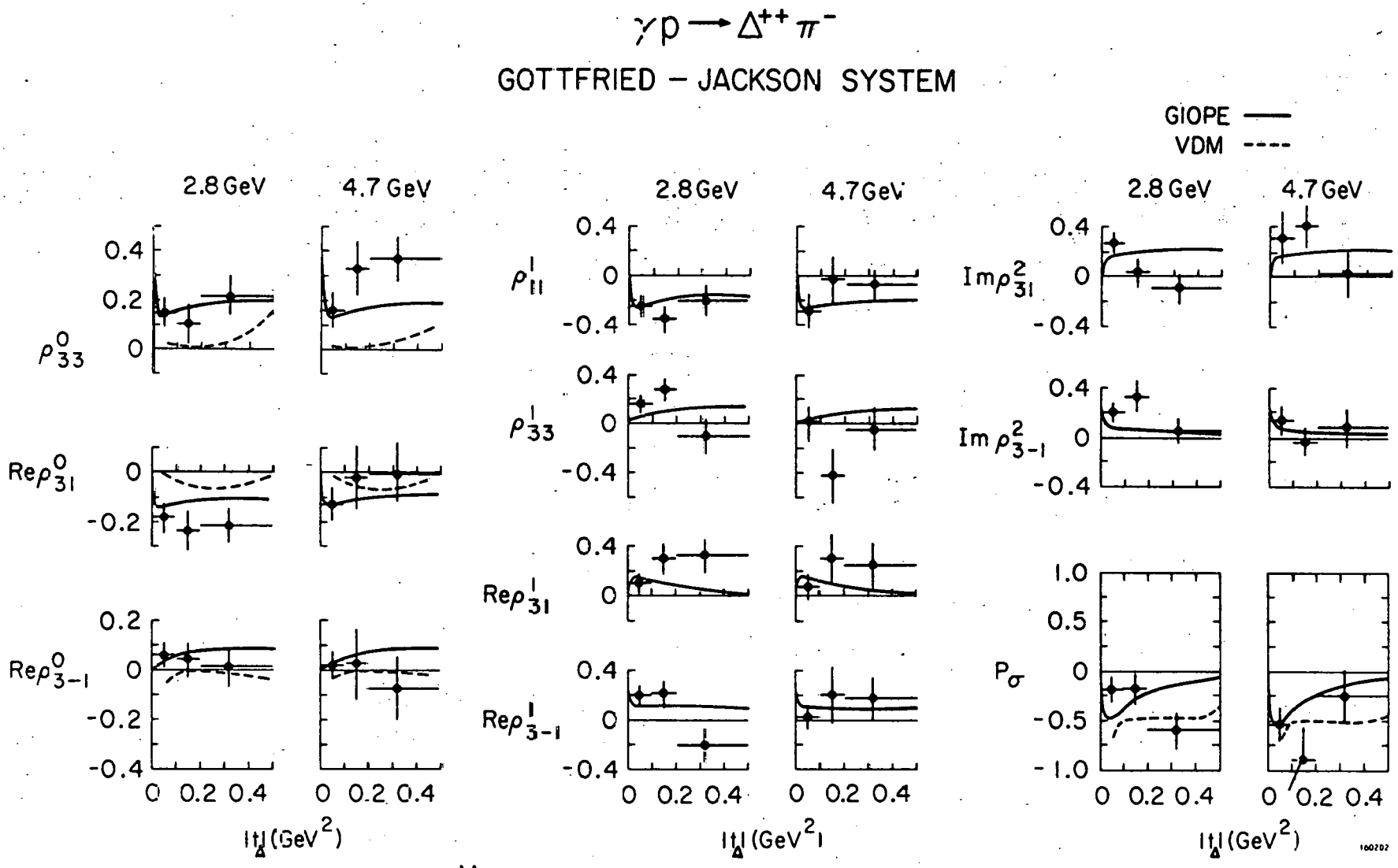

Fig. 32. Reaction $\gamma p \rightarrow \Delta^{++}\pi^{-}$. Density matrix parameters and parity asymmetry P_σ. The solid curves are the predictions of the gauge-invariant OPE model with absorption corrections for $C = 0.8$. The dashed curves show the VDM predictions (Ref. 32).

GeV^2 are given in Table XIV. It is clear that OPE alone cannot explain the data since it would require $P_\sigma = -1$. Qualitatively the same result was obtained in an experiment done at low energy.[80]

Comparison with Theory. We calculated the predictions of the minimal gauge invariant extension of the OPE model (GIOPE) with absorption corrections. Gauge invariance in this model is achieved by adding to the OPE diagram (Fig. 33-I), the s-channel nucleon exchange (Fig. 33-II), the u-channel Δ exchange (Fig. 33-IV), and the contact graph (Fig. 33-III) according to the prescription of Stichel and Scholz.[30] The decomposition of the Born amplitudes into helicity amplitudes was taken from Locher and Sandhas.[81] In contrast to these authors, following the idea of vector dominance, we applied absorption corrections in both initial and final states[82] by multiplying the helicity amplitudes for spin J by the factor[83]

$$\left\{1-C_{in}\ \exp\left(-J^2/2A_{in}q_{in}^2\right)\right\}^{1/2}\left\{1-C_{out}\ \exp\left(-J^2/2A_{out}q_{out}^2\right)\right\}^{1/2}$$

where q is the c.m.s. momentum, A is the slope parameter, C is the absorption parameter ($C = \sigma_T/4\pi A$, σ_T is the total cross section for scattering of either the initial or final state particles) and the indices "in", "out" refer to the initial and final states respectively. We assumed that $A_{in} = A_{out} = A$ and $C_{in} = C_{out} = C$; A was taken from elastic πp scattering to

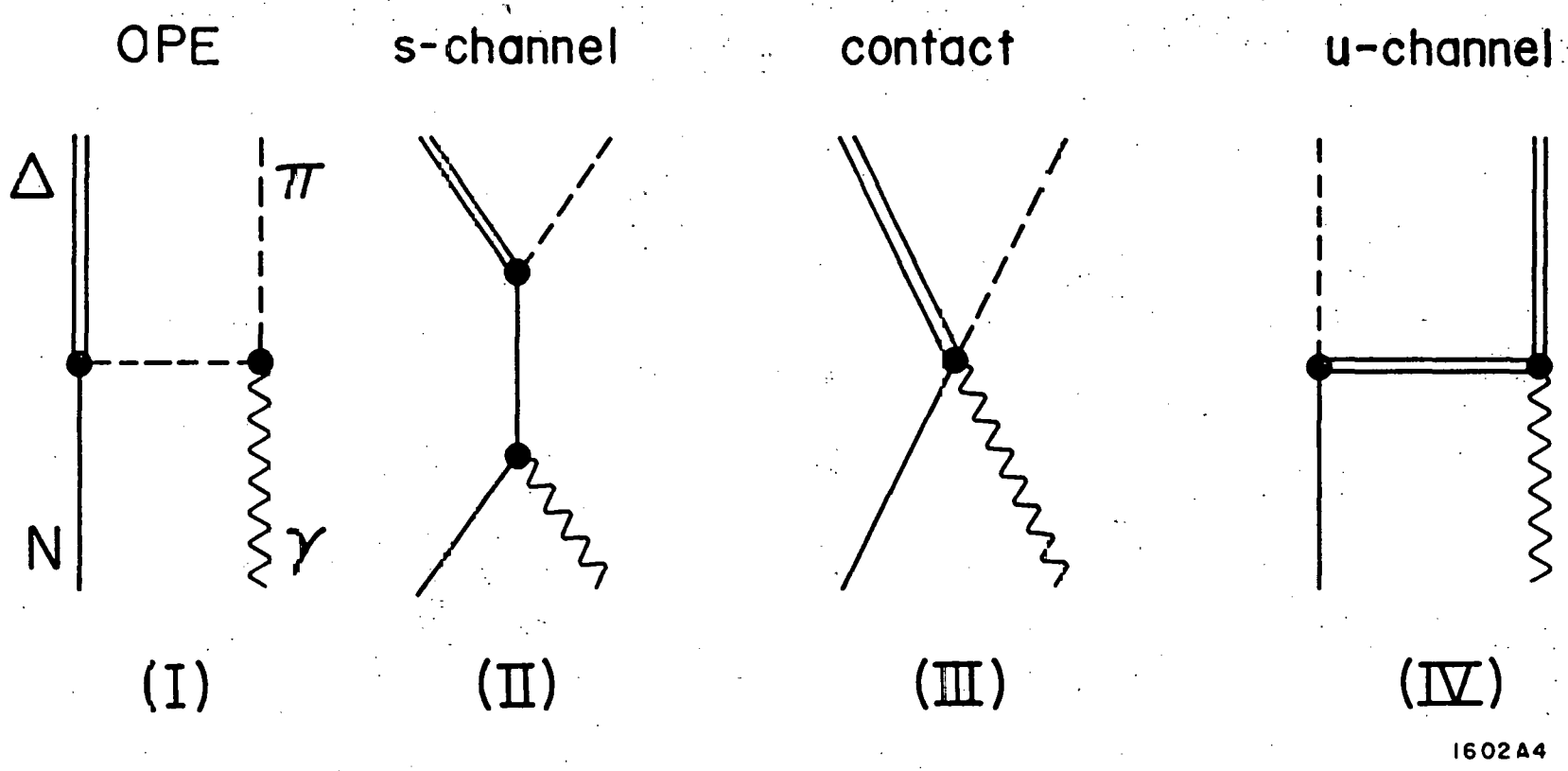

Fig. 33. The four Feynman diagrams for $\gamma p \rightarrow \Delta\pi$ taken into account in the gauge-invariant OPE model.

be 8 GeV^{-2}; for C a value of 0.8 was used. The finite width of the Δ was taken into account by integrating over the π^+p mass range using the (3,3) elastic scattering cross section.

The solid curves in Fig. 31 show the predictions of GIOPE for $d\sigma/dt_\Delta$ ($\gamma p \to \Delta^{++}\pi^-$). For comparison we also give The predictions for C = 1 (dashed curves). Except for the very low $|t|$ region, too much Δ^{++} is predicted.

In Fig. 32 we compare the predictions of GIOPE with the measured density matrix parameters and P_σ as calculated from these. It can be seen that the additional diagrams of Fig. 33 simulate some natural parity exchange contributions in the t-channel. Although there is agreement for $|t_\Delta| \lesssim 0.1$ GeV^2 in an average sense we cannot test the strong variations predicted by GIOPE for $|t_\Delta| \lesssim 0.02$ GeV^2. For $|t_\Delta| > 0.1$ GeV^2 some of the ρ^α_{ik} and P_σ are not reproduced well. The GIOPE predictions for the ρ^α_{ik} are essentially independent of the value of the absorption parameter C. The density matrix parameters predicted by the OPE graph alone, namely, $\rho^1_{11} = -1/2$, all other ρ^α_{ik} in Eq. 16 equal to zero, bear no resemblance to the data.

It is also interesting to determine the ratio $R = \sigma(\gamma p \to \Delta^{++}\pi^-)/\sigma(\gamma p \to \Delta^0\pi^+, \Delta^0 \to p\pi^-)$. If there is only t-channel $I^G = 1^-$ (e.g., π) exchange, then R = 9. Stichel and Scholz in their version of GIOPE keep only contributions equivalent to this $I^G = 1^-$ exchange in the t-channel and hence

predict R = 9. Other versions of GIOPE[81,84] drop this restriction to $I^G = 1^-$ t-channel exchange and R becomes a function of t_Δ. If this $R \neq 9$ is then interpreted in terms of t-channel effects alone it can be taken as evidence for $I^G = 1^+$ (e.g., B) or $I^G = 2^-$ (exotic) exchanges. Our data on R (see Table XIV) are consistent with either version of GIOPE. The data of Boyarski et al.[84] for Δ^{++}, Δ^0, Δ^- production off protons and deuterons are inconsistent with the assumption of I = 1 exchange alone and led to speculations on the existence of exotic exchanges.[29] We point out that these data may be understood in terms of the GIOPE model.[85]

Vector dominance (VDM) relates the reaction $\gamma p \to \Delta^{++}\pi^-$ to the reaction $\pi p \to \Delta V^0$ where V^0 is ρ^0, ω or ϕ. Gotsman[32] has fitted the latter reactions to a sum of Regge exchange amplitudes in order to perform the line reversal needed for the comparison. With $\gamma_\rho^2/4\pi = 0.5$ (γ_ρ describes the γ-ρ coupling strength), his predictions for 5 GeV are in fair agreement with our $d\sigma/dt_\Delta$ for $|t_\Delta| > 0.1$ GeV^2. While his predictions for some of the ρ^α_{ik} and for P_σ (see dashed curve in Fig. 32) are in qualitative agreement, his prediction $\rho^0_{33} \simeq 0$ is not supported by the data.

VI. CONCLUSIONS

The production of $\pi^+\pi^-$ pairs in the s-channel c.m. helicity-conserving p-wave state, determined in a model-independent way, accounts for almost all events in the ρ^o region and shows the same skewing as the $\pi^+\pi^-$ mass distributions. We have observed a variation of the ρ^o mass shape as a function of t and find this related to the variation of the exponential slope of the t distribution with $M_{\pi\pi}$. The Ross-Stodolsky factor, $[M_\rho/M_{\pi\pi}]^4$, used to explain the ρ^o mass shift is inconsistent with our observed t dependence of the ρ mass shape. Furthermore, the prediction of Ross-Stodolsky[10] and others[65-67] that the factor should work at $t = 0$, is not supported by the data near $t = 0$. We have observed an interference of the ρ^o amplitude with background. These features are well described by the interference model of Söding. Since it is necessary to use a model to determine the ρ^o differential cross section, we emphasize that an uncertainty is introduced which is much larger than our experimental errors.

From the correlation of the ρ^o decay with the polarization vector of the incident photon we find that the reaction $\gamma p \rightarrow \rho^o p$ proceeds almost completely through natural-parity exchange up to $|t| = 1.0$ GeV^2 and conserves helicity in the s-channel c.m. system up to $|t| = 0.4$ GeV^2. We remark that these features may be general characteristics of diffraction scattering.[86]

We have observed evidence for ρ^{o}-ω interference in the reaction $\gamma p \rightarrow \pi^{+}\pi^{-}p$. Our results are consistent with the prediction by Goldhaber, Fox, and Quigg[21] and by Horn;[23] they are also in agreement with the results for ρ^{o}-ω interference in diffractive photoproduction of vector mesons on Carbon.[20]

The cross sections, density matrix elements, and parity asymmetry of the reaction $\gamma p \rightarrow \Delta^{++}\pi^{-}$ have been measured as a function of t_{Δ}. The average values for $|t_{\Delta}| < 0.5$ GeV^2, $P_{\sigma} = -0.27 \pm 0.12$ and $P_{\sigma} = -0.53 \pm 0.15$ found at 2.8 and 4.7 GeV, respectively exclude a simple OPE model.

APPENDIX A: Comparison of Measurements at LRL and SLAC.

About half of the three-pronged events from the 2.8 GeV sample were measured at both SLAC and LRL. The measurements at LRL were made on Spiral Reader II. The purpose of the test was to check that the measurement and reconstruction results were consistent between laboratories.

Figure 34 displays the confidence level scatter plot for the 3-constraint fits (reaction $\gamma p \rightarrow \pi^+\pi^- p$); the abscissa of an event gives the LRL result and the ordinate the value of SLAC. The approximately uniform density of events indicates that the calculated errors from TVGP and SQUAW are primarily due to point scatter in measurement. If Coulomb scattering errors were dominant, the χ^2 probability for one measurement would be strongly correlated with a second measurement.

In contrast to the confidence levels, the incident gamma energies as determined from the 3-constraint events measured by LRL and SLAC, as shown in Fig. 35, display the expected 45° line behavior. The scatter from a straight line indicates the measurement error for $E\gamma$. There is a small energy difference ($\approx$ 15 MeV) between LRL and SLAC. This discrepancy is small, and consequently no attempt was made to reduce it. From the scatter of events on Fig. 35 we find the measurement part of the error for $E\gamma$ to be $\pm$ 21 MeV. This error is slightly

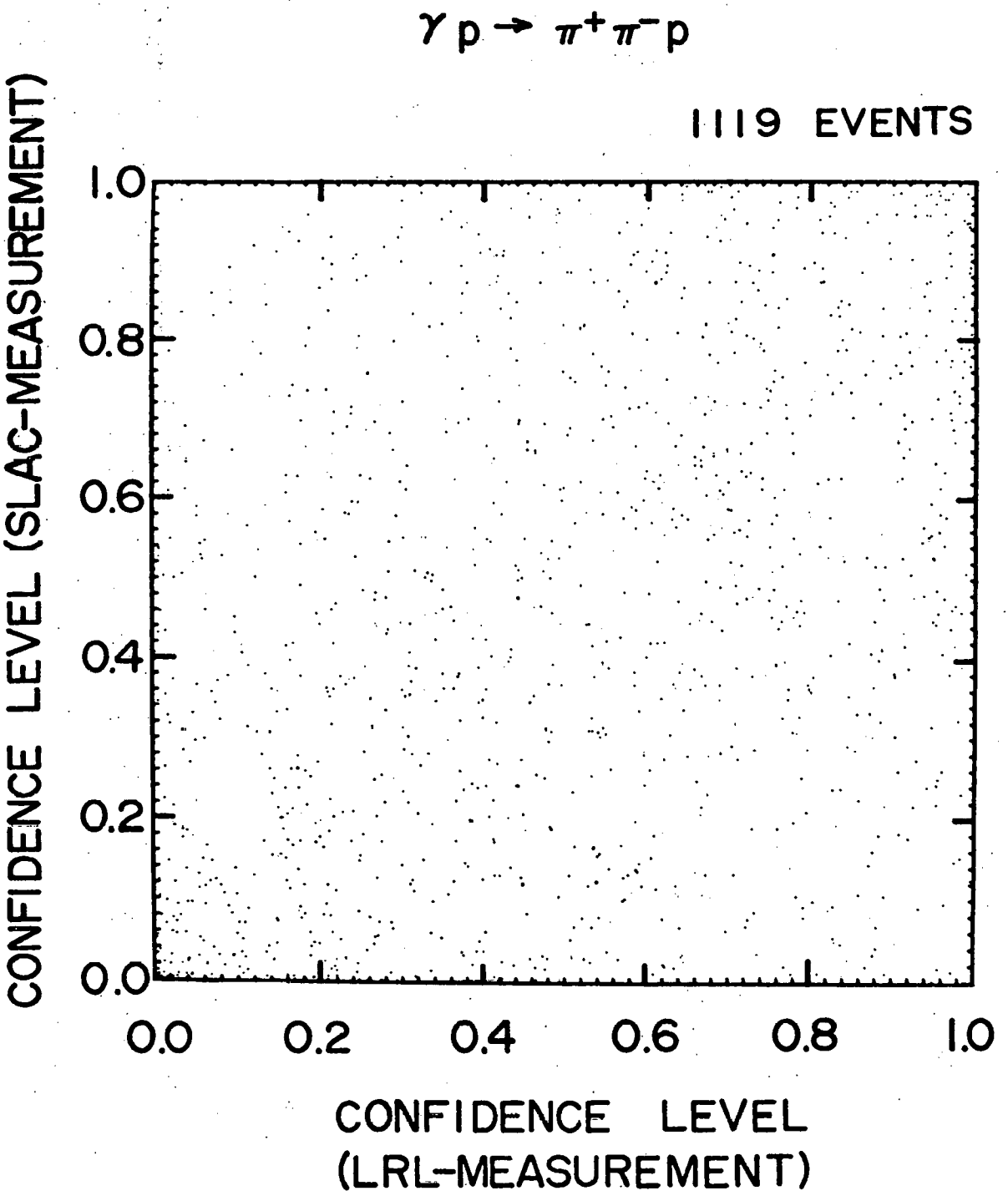

XBL 708-6437

Fig. 34. Confidence level for the 3-constraint fit to $\gamma p \rightarrow \pi^+ \pi^- p$ as determined for events measured at both LRL(abcissa) and SLAC(ordinate).

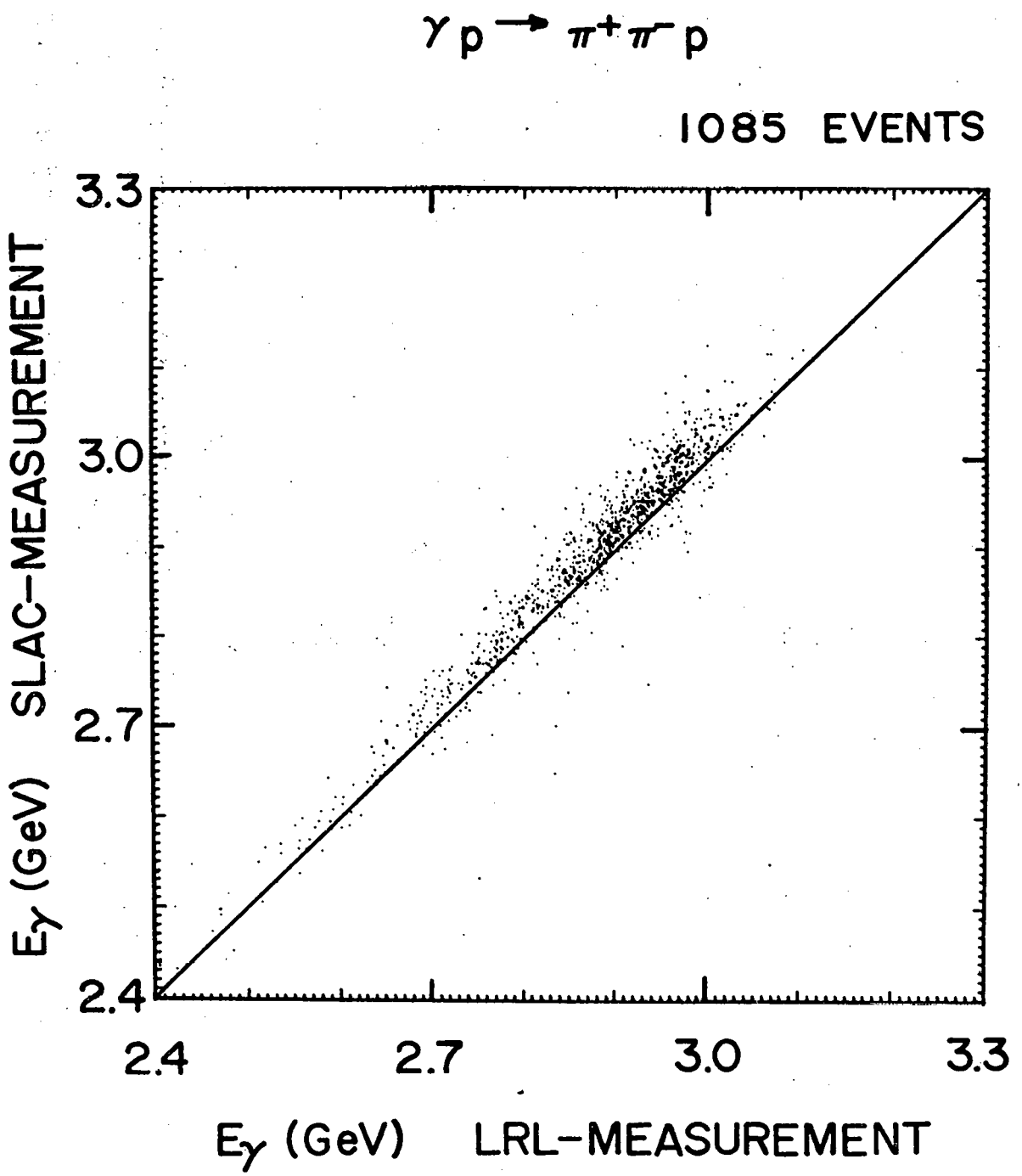

XBL 708-6438

Fig. 35. Photon energy spectra determined by LRL(abcissa) and SLAC(ordinate) from $\gamma p \rightarrow \pi^+ \pi^- p$ fits.

smaller than the calculated error from TVGP-SQUAW of ± 24 MeV (for E_γ above 2.4 GeV) again emphasizing the dominance of measurement errors over those due to Coulomb scattering.

We give the difference between the LRL and SLAC values for the dipion mass in Fig. 36 and the angle ψ in Fig. 37 (see Section IV-C for definition of ψ). Both these distribution are for events in the ρ^o mass region. Again, we see a slight difference for the dipion mass as measured by LRL and SLAC (1.5 MeV), which is small compared to the uncertainty in the fitted mass of e.g. the ρ^o given by the maximum likelihood program ($\delta M_\rho = \pm$ 3 MeV). The width of the distribution in Fig. 36 gives the measurement errors for $M_{\pi\pi}$ to be ± 4.5 MeV and is again slightly less than the calculated error from TVGP (± 5 MeV) and the determination from the K^o decays (± 5 MeV). Excellent agreement is found in the comparison of the angle ψ. The width of the distribution in Fig. 37 gives the measurement uncertainty in the angle ψ as ± 0.4°, which is much less than the systematic uncertainty in the polarization direction of the laser beam itself (± 5°) and consequently in the angle ψ.

We also compared the events for which one laboratory obtained a 3-constraint fit and the other laboratory had a 0-constraint "fit" to the reaction $\gamma p \rightarrow \pi^+\pi^- p\pi^o$. From this sample we conclude that the loss of genuine $\gamma p \rightarrow \pi^+\pi^- p$ events is less than 1% and contamination of 0-constraint events into reaction (1) is less than 1%.

We found no significant discrepancies between LRL and SLAC measurements, and conclude that the procedures for measuring and reconstruction for the two laboratories are compatible.

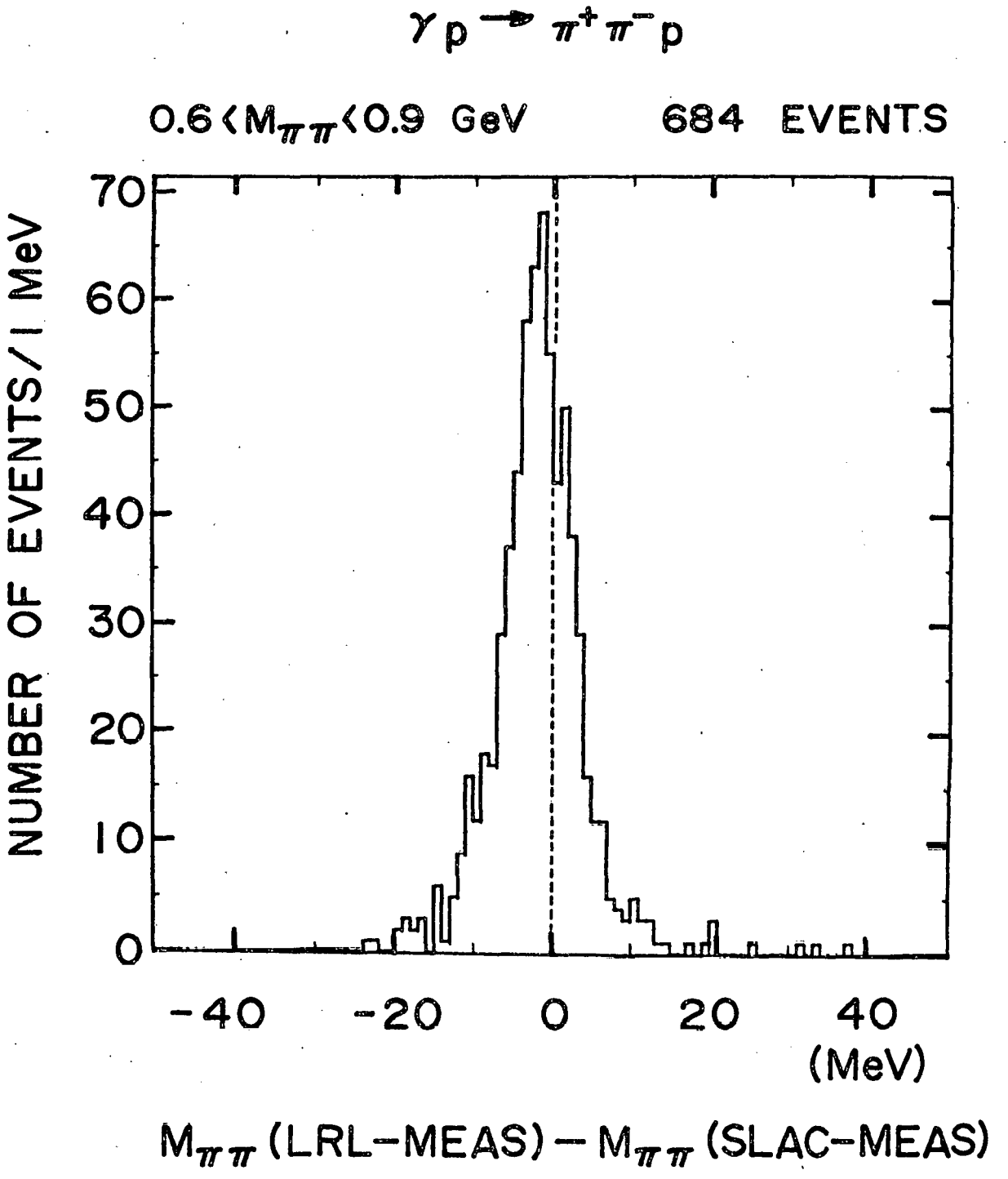

XBL 708-6439

Fig. 36. Difference between the dipion mass for events measured at LRL and SLAC in the rho mass region.

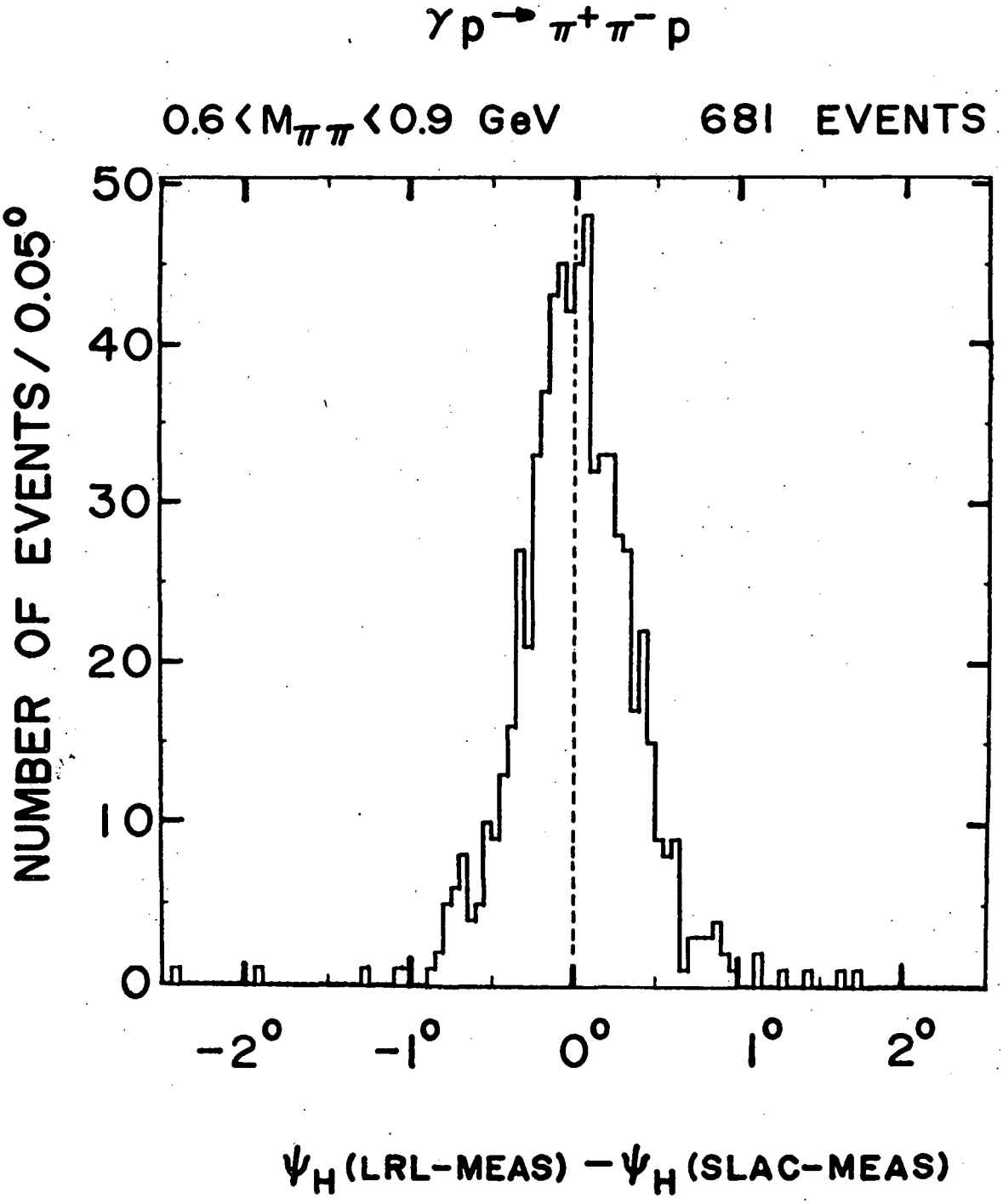

XBL 708-6440

Fig. 37. Difference between the angle ψ for events in the rho mass region measured at LRL and SLAC.

APPENDIX B: Fitting Procedure for Reaction $\gamma p \rightarrow \pi^+\pi^- p$.

Maximum likelihood fits were made using the fitting program OPTIME[87] developed at the Lawrence Radiation Laboratory by P. Eberhard and W. Koellner. The user supplies a function with m variable parameters. OPTIME, in a stepping process, adjusts the parameters such that the sum of the logarithms of the function over all data points reaches a maximum. If, as in our case the function is unnormalized, integration data points are generated by the Monte Carlo program SAGE,[88] which is a set of subroutines in OPTIME. For optimum efficiency the frequency distribution of the SAGE-generated events can be made to resemble as closely as possible the function to be integrated by coding various subroutines.

The effect of a finite number of Monte Carlo events used in the integration of the unnormalized function was checked by generating a second set of Monte Carlo events to normalize the function. The optimized parameters for the two maximum likelihood fits were required to be within 1/2 standard deviation of each other; otherwise, the number of Monte Carlo events was increased.

APPENDIX C: Description of the Söding Model

The predictions of the Söding model[11] have been calculated using a Monte Carlo program written by P. Söding. The formulas employed differ from those given in Ref. 11. We assume the rho amplitude to be helicity conserving in the s-channel c.m. system. The rescattering term proposed by Bauer[52] and Pumplin[53] discussed in Section IV is also included.

In the following we give a brief description of the Söding model used to fit the data of this experiment. We assume that the matrix element for the reaction $\gamma p \rightarrow \pi^+\pi^- p$ is the sum of ρ^o (Diag. I of Fig. 15), Drell type (Diag. II and III), and the rescattering amplitudes (Diag. IV)

$$|M|^2 = |F_\rho \, \hat{\epsilon}_\rho \cdot \hat{\pi}^+_\rho + F_\pi - (\hat{\epsilon}_\gamma \cdot \hat{\pi}^+)_{cms} + F_\pi + (\hat{\epsilon}_\gamma \cdot \hat{\pi}^-)_{cms}|^2 \, , \qquad (19)$$

where $\hat{\epsilon}_\gamma$ is the polarization vector of the incident photon in the center of mass system, $\hat{\epsilon}_\rho = \hat{\rho} \times [\hat{\epsilon}_\gamma \times \hat{\rho}]$ and $\hat{\rho}$ is the ρ^o direction of flight in the center of mass system; $\hat{\pi}^\pm$ is the direction of the $\pi^\pm$ in the appropriate system. The coefficient $\hat{\epsilon}_\rho \cdot \hat{\pi}^+_\rho$ multiplying F_ρ insures helicity conservation for the rho in the s-channel c.m. system. The ρ^o-production is assumed to be mainly absorptive and its decay is taken to be a Breit-Wigner form with a Jackson type width.[51] Thus for F_ρ we use

$$F_\rho = N_\rho \frac{-i\, e^{A_\rho t/2}}{M_\rho^2 - M_{\pi\pi}^2 - i\, M_\rho \Gamma_\rho}, \qquad (20)$$

where A_ρ is the exponential slope of the ρ^o (see Table VIII bottom) and t is the momentum transfer squared between target and recoil protons.

For the Drell amplitudes we use

$$F_{\pi^\pm} = \frac{\pm N_D\, T(\pi^\mp p)}{(m_\pi^2 - t_{\pi^\pm})\left(1 + \frac{m_\pi^2 - t_{\pi^\pm}}{g}\right)} \cdot \frac{M_\rho^2 - M_{\pi\pi}^2}{(M_\rho^2 - M_{\pi\pi}^2 - i\, M_\rho \Gamma)} \qquad (21)$$

where $t_{\pi^\pm}$ is the square of the momentum transfer between the photon and $\pi^\pm$. The term $(1 + (m_\pi^2 - t_{\pi^\pm})/g)^{-1}$ is the Ferrari-Selleri form factor[89] with $g = 65$ GeV^2. The elastic πp-scattering amplitude is

$$T(\pi^\pm p) = \sum_{\ell=0}^{3} \left[(\ell+1)\, A_\ell^+ + \ell\, A_\ell^-\right] P_\ell\, (\cos\theta) \qquad (22)$$

where θ is the πp center of mass scattering angle and $P_\ell(\cos\theta)$ are the Legendre polynomials. The elastic πp partial wave amplitudes,[90] defined by

$$A_\ell^\pm = (\eta_\ell^\pm\, e^{2i\delta_\ell^\pm} - 1)/2ik \qquad (23)$$

correspond to $J = \ell \pm \frac{1}{2}$. For $\pi^- p$ the appropriate isospin sum is used. For the energy of the πp system greater than 1.74 GeV we take $T(\pi^{\pm} p)$ to be purely imaginary with an exponential t dependence. The spin-flip term, which should not interfere with the ρ^o, was not included for the determination of the ρ^o cross sections. Within errors the same ρ^o cross sections are obtained when the extreme assumption is made that the πp elastic scattering amplitude $T(\pi p)$ is purely imaginary, $T(\pi p) = i|T(\pi p)|$.

The term multiplying the πp-scattering amplitude in Eq. 21 is to account for double counting (see Section IV).[54] This factor has been shown by Bauer[52] and Pumplin[53] to be equivalent to adding the absorptive part of the rescattering term (Diag. IV of Fig. 15) to the ρ^o and Drell amplitudes.

P. Söding[11] has pointed out that possible modifications to make the amplitude gauge-invariant will not change the essential results of the model.

ACKNOWLEDGMENTS

I wish to thank Professor H. H. Bingham for encouragement and guidance necessary for the successful completion of this work.

I take this opportunity to thank Professor William B. Fretter and the members of the Particle Physics Group for their help and support during the progress of my research at Berkeley. I will always remember the friendly and receptive manner of Professor Fretter.

I am indebted to the members of the SLAC-Berkeley-Tufts collaboration whose names are given in Reference 1. Their support and work during all phases of this experiment was essential for its successful completion. In particular, I want to acknowledge the cooperation and useful consultation of William Podolsky, Monroe Rabin, Peter Seyboth, Ian Skillicorn, Roland Windmolders, and Gunter Wolf.

The staffs of the Berkeley Physics Department, Lawrence Radiation Laboratory, and the Stanford Linear Accelerator Center deserve much credit for having made my experiences during the past few years both interesting and challenging. In particular, I want to thank Arthur Rosenfeld and Frank Solmitz for the hospitality and support of the A-Group at the Lawrence Radiation Laboratory during the past two years.

The help and cooperation of the SLAC accelerator operations crew and of R. Watt and the 82" bubble chamber group are gratefully acknowledged. A collective thanks to the scanners of

Berkeley and SLAC for their diligent work and W. Hendrix, A. Wang and D. Blohm for their coordinating efforts.

Special appreciation to Marilyn Drew and Barbara Peoples for typing of the manuscript.

Finally, I want to thank my mother and father for their encouragement over many years and my wife Kum Ja for her patience, understanding, and support during the last eight years of my higher education.

FOOTNOTES AND REFERENCES

1. SLAC- Berkeley-Tufts Collaboration:
J. Ballam, H. H. Bingham, G. B. Chadwick, W. B. Fretter, R. Gearhart, Z. G. T. Guiragossián, M. Menke, R. H. Milburn K. C. Moffeit, J. J. Murray, W. J. Podolsky, M. S. Rabin, A. H. Rosenfeld, P. Seyboth, A. Shapira, C. K. Sinclair, I. O. Skillicorn, R. Windmolders, and G. Wolf;

Preliminary results published in:

a. Phys. Rev. Letters, 23, 498, 817(E) (1969) (Cross sections)
b. Phys. Rev. Letters, 24, 955 (1970) (ρ^o production)
c. Phys. Rev. Letters, 24, 960, 1467(E) (1970) (ρ^o decay)
d. Phys. Rev. Letters, 24, 1364 (1970) ($\gamma p \rightarrow \omega p$)
e. Phys. Rev. Letters, 25, 1223 (1970) ($\gamma p \rightarrow \Delta\pi$)
f. UCRL-19753 (1970), Lawrence Radiation Laboratory, Berkeley (submitted to Nucl. Phys. B). (ρ^o-ω interference)

2. K. Schilling, P. Seyboth, and G. Wolf, Nucl. Phys. B15, 397 (1970); B 18, 332 (E).

3. Cambridge Bubble Chamber Group, Phys. Rev. 146, 994 (1966).

4. Aachen-Berlin-Bonn-Hamburg-Heidelberg-München Collaboration, Phys. Rev. 175, 1669 (1968).

5. R. Anderson et al., Phys. Rev. D 1, 27 (1970).

6. See also work quoted by A. Silverman, Proceedings of the 4th International Symposium on Electron and Photon Interactions at High Energies, Liverpool, (1969), edited by D. W. Braben, p. 71.

7. L. Criegee et al., Phys. Letters 28B, 282 (1968), and Phys. Rev. Letters 25, 1306 (1970).

8. G. Diambrini-Palazzi, G. McClellan, N. Mistry, P. Mostek, H. Ogren, J. Swartz and R. Talman, Phys. Rev. Letters, 25, 478 (1970).

9. D. McLeod, S. Richert, A. Silverman, Phys. Rev. Letters 7, 383 (1961).

10. M. Ross and L. Stodolsky, Phys. Rev. 149, 1172 (1966).

11. P. Söding, Phys. Letters 19, 702 (1965); see also A. S. Krass, Phys. Rev. 159, 1946 (1967).

12. The results for ρ^{o}-ω interference given in this report are the same with minor exceptions to that given in Ref. 1f.

13. J. Bernstein and G. Feinberg, A Needle in a Haystack, in Proceedings of XI International Conference on High Energy Physics, CERN, 1962, p. 170.

14. S. M. Flatté et al., Phys. Rev. 145, 1050 (1966), and S. M. Flatté, Phys. Rev. D 1, 1 (1970). A complicated interference is observed in the reaction $K^-p \to \pi^+\pi^-\Lambda$ at incident momenta ranging from 1.2 to 2.7 GeV/c.

15. G. Goldhaber, W. R. Butler, D. G. Coyne, B. H. Hall, J. N. MacNaughton, and G. H. Trilling, Phys. Rev. Letters 23, 1351 (1969). Destructive interference (a dip at $m_{\pi\pi} = m_\omega$) is seen in $\pi^+p \to \pi^+\pi^-\Delta^{++}$ at 3.7 GeV/c.

16. J. E. Augustin et al., Lettere Nuovo Cimento 2, 214 (1969). An interference effect is seen in $e^+e^- \to \pi^+\pi^-$ and interpreted as destructive interference. See also F. Laplanche, Paris, Thesis, LAL-1229, 1970, unpublished.

17. T. N. Rangaswamy, A. R. Clark, Bruce Cork, T. Elioff, L. T. Kerth, and W. A. Wenzel, Contribution to the Argonne Conference on $\pi\pi$ and $K\pi$ Interactions; also private communication. Constructive interference is seen in $\pi^-p \to \pi^+\pi^-n$ at 3 to 5 GeV/c.

18. W. W. M. Allison, W. A. Cooper, T. Fields, and D. E. Rhines, Phys. Rev. Letters 24, 618 (1970). A complicated interference is seen in $\bar{p}p \to 2\pi^+2\pi^-$ at 1.26 and 1.65 GeV/c.

19. M. Abramovich et al., Evidence for ρ-ω Interference in π^-p Interactions at 3.9 GeV/c, Nuclear Physics B 20, 209 (1970).

20. P. J. Biggs et al., Phys. Rev. Letters 24, 1201 (1970). They measure the magnitude and phase of ρ-ω interference in $\pi^+\pi^-$ photoproduction from carbon.

21. A. S. Goldhaber, G. C. Fox, and C. Quigg, Phys. Letters 30B, 249 (1969), hereafter called GFQ. The earlier literature may be traced from this paper.

22. M. Gourdin, L. Stodolsky, and F. M. Renard, Phys. Letters 30B, 347 (1969).

23. D. Horn, ρ^0-ω Interference, Phys. Rev. D 1, 1421 (1970).

24. R. G. Sachs and J. F. Willemsen, Two-Pion Decay Mode of the ω and ρ-ω Mixing, Phys. Rev. D 2, 133 (1970).

25. G. Goldhaber, Proceedings of the 1970 Philadelphia Conference on Meson Spectroscopy, ed. by C. Baltay and A. Rosenfeld, (Columbia University Press, New York, 1970).

26. Aachen-Berlin-Bonn-Hamburg-Heidelberg-München Collaboration, Phys. Letters 23, 707 (1966); see also Ref. 4.

27. Cambridge Bubble Chamber Group, Phys. Rev. 163, 1510 (1967).

28. A. M. Boyarski et al., Phys. Rev. Letters 22, 148 (1969).

29. H. Harari, Proceedings of the International Symposium on Electron and Photon Interactions at High Energies, Liverpool, England, September 1969, edited by D. W. Braben (Daresbury Nuclear Physics Laboratory, Daresbury, Lancashire, England, 1970); p. 107.

30. P. Stichel and M. Scholz, Nuovo Cimento 34, 1381 (1964).

31. K. Böckmann, W. Sandhas and H. Wessel, Z. Physik 202, 477 (1967).

32. E. Gotsman, Phys. Rev. 186, 1543 (1969), and private communication.

33. William Podolsky, Thesis, UCRL Report 20128, 1970, Lawrence Radiation Laboratory, Berkeley.

34. R. H. Milburn, Phys. Rev. Letters 10, 75 (1963); see also R. H. Milburn, Stanford Linear Accelerator Center Report No. SLAC-41, 1965 (unpublished).

35. F. R. Arutyunian, I. I. Goldman, and V. A. Tumanian, Z. H. Eksperim, i Teor. Fiz 45, 312 (1963). [translation: Soviet Phys. - JETP 18, 218 (1964); F. R. Arutyunian and V. A. Tumanian, Phys. Letters 4, 176 (1963)].

36. J. J. Murray and P. Klein, Stanford Linear Accelerator Center Report No. SLAC-TN-67-19, 1967 (unpublished).

37. C. K. Sinclair, J. J. Murray, P. Klein, and M. Rabin, IEEE Trans. on Nucl. Sci. 16, 1065 (1969).

38. R. A. Gearhart, P. R. Klein, J. J. Murray, W. J. Podolsky and M. S. Rabin, Nuc. Instr. and Methods 75, 220 (1969).

39. W. Heitler, The Quantum Theory of Radiation, (Oxford University Press, London, 1954, 3rd edition); p. 257.

40. F. T. Solmitz, A. D. Johnson, and T. B. Day, THREE VIEW GEOMETRY PROGRAM, Alvarez Group Programming Note -P-117 (1966); O. I. Dahl, T. B. Day, F. T. Solmitz, and N. L. Gould, SQUAW, Alvarez Group Programming Note -P-126, (1968), Lawrence Radiation Laboratory, Berkeley, unpublished.

41. E. Burns, D. Drijard, PHONY, Trilling-Goldhaber Group Technical Note 143, Lawrence Radiation Laboratory, Berkeley (1968), unpublished.

42. A. H. Rosenfeld and W. E. Humphrey, Ann. Rev. Nucl. Sci. 13, 103 (1963).

43. J. Jost, J. M. Luttinger, and M. Slotnick, Phys. Rev. 80, 189 (1950).

44. T. M. Knasel, DESY Preprint No. 70-3 (1970).

45. H. A. Bethe and W. Heitler, Proc. Roy. Soc. (London), A146, 83, (1934); H. A. Bethe, Proc. Camb. Phil. Soc. 30, 524 (1934).

46. K. J. Mork, Phys. Rev. 160, 1065 (1967); K. J. Mork and H. Olsen, Phys. Rev. 140, B1661 (1965).

47. D. Notz, Diplomarbeit, Universität, Hamburg (see Ref. 44).

48. J. Ballam et al., Phys. Rev. Letters 21, 1541 (1968); 21, 1544 (1968); Y. Eisenberg et al., ibid. 22, 669 (1969).

49. J. A. Shapiro, Phys. Rev. 179, 1345 (1969).

50. H. Satz and K. Schilling, Il Nuovo Cimento 67A, 511 (1970). These authors explain the ρ mass shift. In contradiction to experiment, the published version of their model predicts t-channel helicity conservation for ρ^0 production, however, they maintain this is not an essential feature to their model (private communication).

51. J. D. Jackson, Nuovo Cimento 34, 1644 (1964).

52. T. Bauer, Phys. Rev. Letters 25, 485 (1970).

53. J. Pumplin, Report No. SLAC-PUB-730 (1970).

54. Only the p-wave part of the Drell amplitude should be multiplied by the factor proposed by Bauer and Pumplin. Because the Drell term is $\approx$ 90% p-wave, a small error results when the entire Drell amplitude is multiplied by this factor as was done for our analysis.

55. M. Davies, I. Derado, D. Drickey, D. Fries, R. Mozley, A. Odian, F. Villa, and D. Yount, Phys. Rev. D 3, 790 (1970).

56. The exponential slope A determined from a fit to the differential cross section values obtained with the parameterization $(M_\rho/M_{\pi\pi})^{n(t)}$ should not be compared directly with A_ρ of Eq. (2) found in the fit to be ≈ 6.3 GeV^{-2} because of the t dependence of $(M_\rho/M_{\pi\pi})^{n(t)}$ (see Eq. 3).

57. L. Stodolsky, Phys. Rev. Letters 18, 135 (1967).

58. Z. G. T. Guiragossián and A. Levy, Nucl. Phys. 1311, 449 (1969).

59. J. E. Augustin, et al., Phys. Letters 28B, 503 (1969).

60. S. C. C. Ting, Proc. of the 14th Int. Conf. on High-Energy Physics, Vienna (1968) (CERN, Geneva, 1968); p. 43.

61. The y axis is the normal to the production plane, defined by the cross product $\hat{k} \times \hat{\rho}$ of the direction of the photon and the vector meson. The x axis is given by $\hat{x} = \hat{y} \times \hat{z}$. The angle Φ between the electric vector of the photon, ϵ, and the production plane in the total c.m. system is defined by: $\cos\Phi = \hat{k}\cdot(\hat{\epsilon} \times \hat{y})$, $\sin\Phi = \hat{y}\cdot\hat{\epsilon}$. The decay angles θ, ϕ are the polar and azimuthal angles of the direction of flight of the π^+ in the ρ rest system:

$$\cos\theta = \hat{\pi}\cdot\hat{z}$$
$$\cos\phi = \hat{y}\cdot(\hat{z} \times \hat{\pi})/|\hat{z} \times \hat{\pi}|$$
$$\sin\phi = -\hat{x}\cdot(\hat{z} \times \hat{\pi})/|\hat{z} \times \hat{\pi}|$$

62. R. L. Thews, Phys. Rev. 175, 1749 (1968).

63. In these fits the values of the ρ^{α}_{ik} were not constrained (see Ref. 2). Consequently P_σ and Σ may be greater than unity.

64. Symmetric rho decays are obtained with counters and magnetic field arranged to detect pions (+) at both $\theta = \frac{\pi}{2}$ and $\phi = \frac{\pi}{2}$.

65. This assumption was made in the "strong absorption model", Y. Eisenberg, et al., Phys. Letters 22, 217 (1966); 22, 223 (1966); see also G. Kramer, DESY Report No. 67/32, (1967) (unpublished).

66. G. Kramer and J. L. Uretsky, Phys. Rev. 181, 1918 (1969).

67. G. Kramer and H. R. Quinn, DESY Report No. 70/23 (1970).

68. P. D. Mannheim and U. Maor, Phys. Rev. D2, 2105 (1970).

69. P. J. Biggs et al., Phys. Rev. Letters 24, 1197 (1970). The phase shift between ρ^o and ω due to nuclear effects ϕ_N, was measured in this $\gamma C \rightarrow e^+e^-C$ experiment to be 100^{+38}_{-30} deg. However, it has been pointed out that such a large phase is disastrous for both simple VDM and diffractive production models (see J. Pumplin and L. Stodolsky, SLAC-PUB-786, unpublished). A recent measurement by H. Alvensleben, et. al., Phys. Rev. Letters 25, 1373 (1970) determined ϕ_N for γ Be $\rightarrow e^+e^-$ Be to be $41^o \pm 20^o$.

70. The ratio of natural parity exchange [$P = (-1)^J$] cross sections for ρ^o-ω photoproduction has been found in our experiment to have values between 6 and 9 depending on the model used to determine the ρ^o cross section. See SLAC-Berkeley-Tufts Collaboration, Ref. 1d, and Ref. 33.

71. By diagonalizing the ρ^o-ω mass-mixing matrix (see Refs. 21,72) the relationship between δ and the BR = $\Gamma_{\omega\to 2\pi}/\Gamma_{\omega\to all}$ is found to be

$$\frac{\Gamma_{\omega \to \pi\pi}}{\Gamma_{\omega \to all}} = \left|\frac{\delta}{m_\rho - m_\omega - i(\Gamma_\rho - \Gamma_\omega)/2}\right|^2 \frac{\Gamma_{\rho \to 2\pi}}{\Gamma_{\omega \to all}}.$$

In the maximum-likelihood fit we determined $M_\rho = 766 \pm 3$ MeV, $\Gamma_\rho = 145 \pm 6$ MeV, and have used $M_\omega = 784$ MeV, $\Gamma_\omega = 12.7$ MeV.

72. S. Coleman and S. Glashow, Phys. Rev. Letters 6, 423 (1961).

73. The degree of Δ^{++} loss because of the cut for $|t| < 0.02$ GeV^2 was further checked by fitting the Δ^{++} production as a function of $|t|$ and extrapolating the $d\sigma(\Delta^{++})/dt$ behavior into the small $|t|$ region. From this test less than 1% (< 4 events) of the Δ^{++} events were lost. Here t is the square of the momentum transfer between target and recoil protons.

74. The discrepancy is illustrated in Fig. 1 of C. Quigg and F. von Hippel, pp. 477-490 in Experimental Meson Spectroscopy, ed. by C. Baltay and A. Rosenfeld, (Columbia University Press, New York, 1970). Against $\sqrt{s}$ they plot $\sin^2 \delta_{33}$ for πN scattering both from the experimental data compiled in Ref. 75 and from Breit-Wigner parameterizations. If they choose a size parameter of 10 Fermis, there is agreement up to 1400 MeV, but at 1500 MeV, the experimental $\sin^2 \delta_{33}$ is 0.07 against 0.15 from the Breit-Wigner. At 1800 MeV the experimental δ passes through 180° and begins a second resonance while the B. W.

value is still finite. In our Eq.(15) we arbitrarily set $\sin \delta_{33} = 0$ for $M > 1800$ MeV.

75. A. Donnachie, R. G. Kirsopp, and C. Lovelace, CERN Report No. TH 838, (1967) (unpublished).

76. R. L. Anderson et al., Phys. Rev. Letters 23, 721 (1969).

77. D. S. Beder and P. Söding, Report No. UCRL-17867, Lawrence Radiation Laboratory (1967) (unpublished).

78. P. Stichel, Z. Physik 180, 170 (1964).

79. P. Eberhard and M. Pripstein, Phys. Rev. Letters 10, 351 (1963).

80. R. W. Morrison, D. J. Drickey, and R. F. Mozley, Nuovo Cimento 54, 409 (1968).

81. M. P. Locher, and W. Sandhas, Z. Physik 195, 461 (1966).

82. G. Kramer, K. Schilling and L. Stodolsky, Nucl. Phys. B5, 317 (1968).

83. K. Gottfried and J. D. Jackson, Nuovo Cimento 34, 735 (1964).

84. A. Boyarski et. al., Phys. Rev. Letters 25, 695 (1970).

85. See also J. A. Campbell, R. B. Clark, and D. Horn, Report No. CALT-68-245, California Institute of Technology (1970).

86. See also F. J. Gilman, J. Pumplin, A. Schwimmer, and L. Stodolsky, Stanford Linear Accelerator Center, Physics Letters 31B, 387 (1970).

87. P. Eberhard and W. Koellner, Principles of the OPTIME System, UCRL-20159 (1970), Lawrence Radiation Laboratory, Berkeley, unpublished.

88. J. Friedman, SAGE, Group A Programming Note-P-189, (1969), Lawrence Radiation Laboratory, Berkeley, unpublished.

89. E. Ferrari and F. Selleri, Phys. Rev. Letters 7, 387 (1961).

90. P. Bareyre, C. Brickman, A. U. Stirling, and G. Villet, Phys. Letters 18, 342 (1965). This was the set of solutions available when the program was written.

TECHNICAL INFORMATION DIVISION
LAWRENCE RADIATION LABORATORY
UNIVERSITY OF CALIFORNIA
BERKELEY, CALIFORNIA 94720